ROMA TRE UNIVERSITY
Department of Mathematics and Physics
Doctoral School in Mathematics and Physics
XXVII Cycle

Ph.D. Thesis in Physics

Uranium groundwater monitoring and seismic analysis into the Gran Sasso hydrogeological basin

by
Marta Ciarletti

Tutor
Prof. Wolfango Plastino

Coordinator
Prof. Roberto Raimondi

Marty: "Wait a minute.
Wait a minute Doc, uh,
are you telling me you built
a time machine...
...out of a DeLorean?"

Doc: "The way I see it,
if you're going to build
a time machine into a car,
why not do it with some style?"

(Back to the future, 1985)

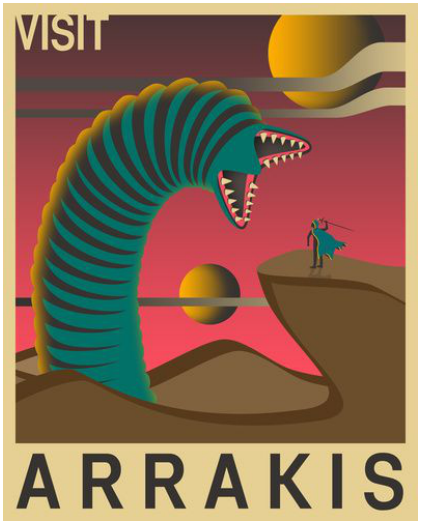

Dune, novel by Frank Herbert, 1965: stylized image.

Contents

Introduction

This thesis is based on the identification and characterization of possible anomalies in uranium (U) groundwater content and on the correlation between this observable and the seismicity of the sampling area. Such an analysis is one of the first studies in this research field available so far, mainly due to the uniqueness of the achievable observations. In fact, uranium groundwater content is monitored within the framework of the INFN's scientific program ERMES (Environmental Radioactivity Monitoring for Earth Sciences) since June, 2008. The area under investigation was affected by a seismic swarm from October, 2008 to December, 2009, with the main shock occurring at 01:33 UT on April 6^{th}, 2009 (M_l=5.9).

Gran Sasso National Laboratories (LNGS-INFN) are located inside the largest aquifer in central Italy and within the limestone formation of the upturned syncline, near the main overthrust fault. This complex hydrogeological system implies the separation of water masses belonging to two different creeks: the former, where the main laboratories are located, flows in well drained cretaceous formation, while the latter is within not drained and poorly permeable dolomitic formations. Depending on the path and on percolation features, water masses are therefore characterized by different chemical-physical properties. These physical observables have been constantly monitored since June, 2008.

Uranium content is detected by Inductively Coupled Plasma Mass Spectrometer (ICP-MS).

The main aim of this work is to study the trend of uranium concentration in groundwater, sampled weekly at LNGS-INFN for a time span of six years in four sampling sites, as well as to identify local seismic activity.

This work is divided in four chapters:

- in Chapter 1, uranium chemical-physical properties in water, sediments and soils are described in detail. In order to explain uranium transport from the upper mantle to the aquifer, geophysical and petrological models are investigated. ERMES experiment and groundwater sampling sites are also described;

- in Chapter 2, Inductively Coupled Plasma Mass Spectrometry (ICP-MS) analysis is illustrated;

- in Chapter 3, the first part of the analysis is shown. The Italian Seismological Instrumental and Parametric Data-Base is analyzed in detail. The L'Aquila earthquake is studied from different points of view: the analysis centered at LNGS-INFN is compared with the analysis centered at the epicenter of the main shock (*a posteriori* analysis). Seismicity around Gran Sasso National Laboratories is studied with the aim to distinguish periods of seismic activity from periods of mild seismicity; for this purpose, the intersection between the area of composite seismogenic sources and the surface of the aquifer is considered and four periods of relatively high seismic activity are identified, also taking into account the aftershocks of the L'Aquila earthquake;

- in Chapter 4, the optimization of a Fast Fourier Transform (FFT) algorithm is described. We developed a script and enforced it to infer information about the main features of the time series of an observable. Such a procedure aims at identifying the main characteristic frequency intervals and, after a filtering procedure, at pointing out the outliers of the residual distribution.

  This method is tested on synthetic time series, for verifying its efficacy.

  The time series of U content in sites E1, E3, E3dx and E4 are studied in detail, to find any possible correlation between uranium groundwater anomalies and seismic energy release.

Chapter 1

Uranium chemical-physical properties and geodynamic processes

1.1 Uranium

Uranium (atomic number 92) is a silvery-white metallic chemical element in the actinide series of the periodic table, with symbol U. If pure, U is malleable, ductile and weakly paramagnetic, strongly electropositive and is a poor electrical conductor (Hammond, 2000).

In nature, uranium is found as uranium-238 (99.274%), uranium-235 (0.719%), and a very small amount of uranium-234 ($\sim$ 0.007%). It is also found in traces as uranium-233 and uranium-236. The half-life of uranium-238 is about 4.47 billion years and that of uranium-235 is 704 million years (Krupka and Serne, 2002).

Uranium is present in low concentrations in every rock or soil ($\sim$0,7$\div$11 10^{-6}g/g) and basically in every water, combined with other elements ($\sim$0,1$\div$50 10^{-9}g/g). In particular, uranium is found in hundreds of minerals including uraninite (the most common uranium ore), carnotite, autunite, uranophane, torbernite, and coffinite. Significant concentrations of uranium occur in some substances such as phosphate rock deposits, and minerals such as lignite, and monazite sands in uranium-rich ores (Hammond, 2000).

Uranium in groundwater plays a lead role in description and analysis of deep aquifer. Transport of metals or radionuclides in porous means is strongly conditioned by water-rock interactions. The knowledge of equilibrium and mobility characteristics of uranium and of chemical reactions near water-rock interface is essential for studying groundwater dynamics.

Concentrated uranium deposits are spotted in uraninite, U(IV)O_2. By means of atmospheric agents on uraninite, secondary minerals containing uranium(VI) are obtained: oxyhydroxides, phosphates, silicates, sulphates and carbonated of uranium. These minerals are sources of mobility of uranium.

The time-scales of sorption and precipitation-dissolution reactions (minutes to hours) are similar to the residence times of natural water systems including groundwaters, and consequently many natural water systems are not at chemical equilibrium (Langmuir, 1997).

In aqueous solution uranium can exist in oxidation states of +III, +IV, +V, and +VI; however, under environmental conditions only the tetravalent and hexavalent states are stable and their two corresponding oxides are uranium dioxide (UO_2) and uranium trioxide (UO_3), respectively (Seaborg, 1968). Other uranium oxides such as uranium monoxide (UO), diuranium pentoxide (U_2O_5), and uranium peroxide ($UO_4 2H_2O$) also exist.

The most common forms of uranium oxide are triuranium octaoxide (U_3O_8) and uranium dioxide. Both oxide forms are solids that have low solubility in water and are relatively stable over a wide range of environmental conditions. Triuranium octaoxide is the most stable compound of uranium and is the common form in nature.

Because of their stability, uranium oxides are generally considered the preferred chemical form for storage or disposal (Krupka and Serne, 2002).

At high temperature (250°C-300°C), U reacts with hydrogen and produces uranium hydride. At higher temperature, hydrogen is reversibly removed; this property make hydrides good for the formation of uranium dust.

Uranium hydride exists in two different crystalline forms: α, stable at low temperatures, β, produced if temperature is higher than $\sim$250°C.

Uranium carbides and nitrides are both semi-metals, relatively inert, hardly soluble in acids. They react with water and they could be flammable in air producing U_3O_8.

Common uranium carbides are UC, UC_2 and U_2C_3. Both UC and UC_2 are produced adding carbon to melt uranium or processing uranium to carbon monoxide at high temperatures. U_2C_3 is stable at temperature up to 1800°C and it is produced processing a mixture of UC and UC_2 to mechanical strain.

Uranium nitrides are produced processing the metal directly to nitrogen, e.g. UN, UN_2 and U_2N_3 (Krupka and Serne, 2002).

1.1.1 Chemical features of uranium in water

The dissolution of uranium in water is favored by the transformation of rocks and minerals that contain it, as a result of climate change and geological

processes.

Uranium is particularly concentrated in the sedimentary rocks, particularly in organic schists; significant amounts are also in the metamorphic and igneous rocks, with higher concentrations in granite than in basalts.

The solubility of uranium in aqueous systems is controlled mainly by three factors: oxidation-reduction potential (ORP), pH and the amount of dissolved carbonates.

In aqueous solutions uranium in hexavalent state is considerably more soluble than uranium(IV).

Uranium salts exist in all the four oxidation states. They are soluble in water and they can be studied in aqueous solutions.

Oxidized products are U^{3+} (brown-red), U^{4+} (green), UO_2^+ (instable) e UO_2^{2+} (yellow).

U^{3+} ions release hydrogen in water, so they are highly instable. UO_2^{2+} ion is the realization of uranium(VI) and it generally forms compounds as uranyl carbonate, uranyl chloride and uranyl sulphate species. Pourbaix plot showing the domains of stability of dissolved and solid uranium species is given in Figure 1.1. The vertical axis is labeled E_H for the voltage potential with respect to the standard hydrogen electrode (SHE) as calculated by the Nernst equation (Kelly et al., 2002). The horizontal axis is labeled pH for the -log function of the H^+ ion activity. The dashed green lines show the stability limits of water in the system.

As we stated before, uranium(VI) is considerably more soluble than uranium(IV). Under reducing conditions, uranium(IV) complexes with hydroxide or fluoride are the only dissolved species. The precipitation of uranium(IV) under reducing conditions is the dominant process leading to naturally enriched zones of uranium in the subsurface (Gascoyne et al., 1992).

In oxidizing aqueous environments, uranium (VI) is present as the linear uranyl dioxo ion (UO_2^{2+}) and an array of mononuclear and polynuclear hydrolysis species. With increasing carbonate concentrations, mononuclear uranyl carbonate species become increasingly important (Giammar, 2001).

Dissolved uranium speciation as a function of pH in an open system is plotted in Figure 1.2 for a total uranium concentration of 10 μM. Although the speciation of dissolved U(VI) is likely to be dominated by hydrolysis and carbonate complexes, in environmental systems complexes with sulphate, fluoride, and organic ligands may also occur. Carboxyl groups on naturally occurring humic and fulvic acids can strongly bind uranium (Gascoyne et al., 1992).

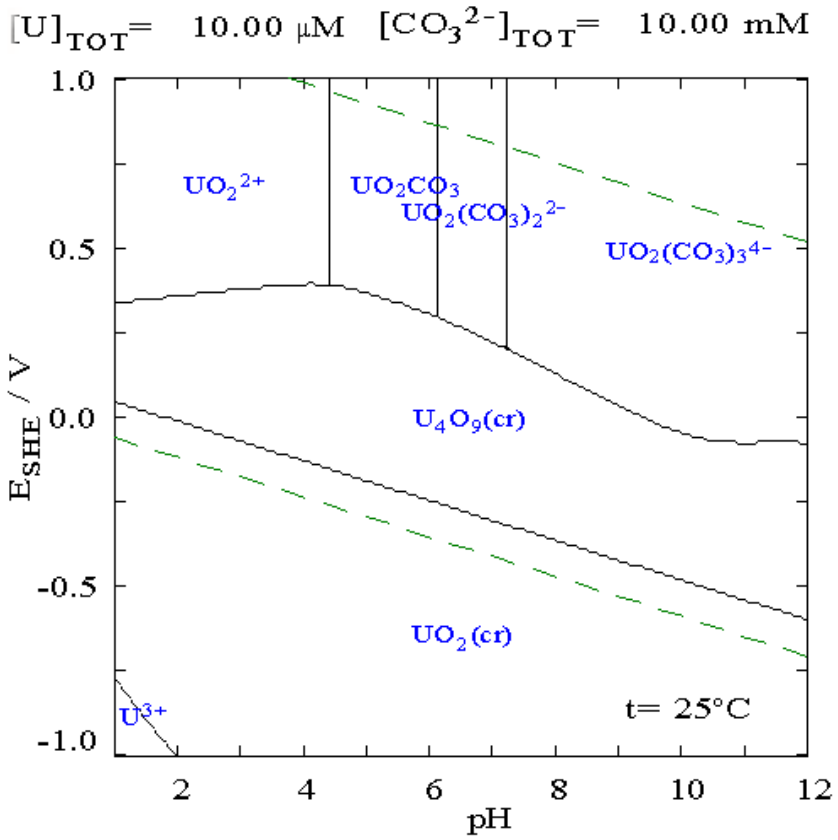

Figure 1.1: Uranium in carbonate solution (Krupka and Serne, 2002).

1.1.2 Uranium in sediments and soils

Uranium is immobile when present in a precipitated form or adsorbed to immobilized solid media and mobile when present in the dissolved phase or associated with mobile colloids.

The association of uranium with solid phases and the mobility of uranium is obviously dependent on site-specific conditions, but it's possible to describe the behavior of uranium in porous media by general trends.

When dissolved carbonate concentrations are high, uranium is highly mobile due to the formation of uranyl-carbonate species. The sorption of uranium to aquifer materials is frequently dominated by association with iron oxyhydroxide minerals (Giammar, 2001).

In uncontaminated soils, the high sorption of uranyl was conferred to the amount of contained goethite (FeO(OH)).

A study of five U.S. soils found out the relation between the solid-water

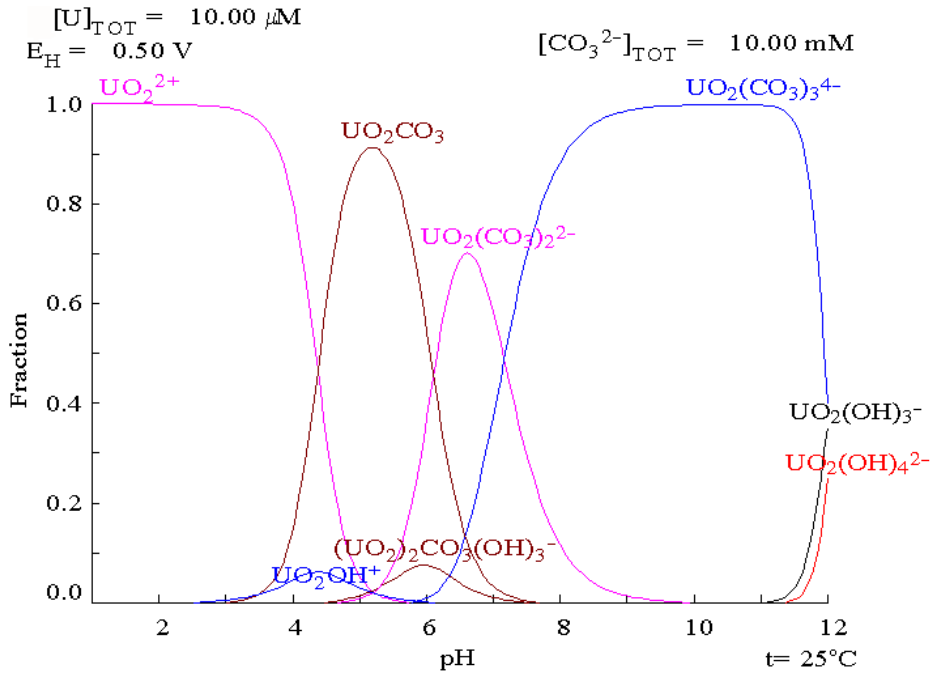

Figure 1.2: Relative concentrations of uranium chemical forms in carbonate solution (Krupka and Serne, 2002).

partitioning of radionuclides and the distribution of particles among three size classes: colloidal particles, humic acid polymers, and larger soil particles (Sheppard et al., 1980).

A study of 13 French soils found out a strong correlation between uranyl sorption and soil pH with sorption decreasing with increasing pH, an effect related to the inhibition of uranium sorption by carbonate in the higher pH soils (Echevarria et al., 2001).

The mechanism of transport of uranium in natural water has been studied for long time and for many different environmental systems; one of the most efficient is associated with colloidal phases in surface water (Porcelli et al., 1997).

A large effort has been dedicated to measuring and modeling uranium transport in groundwaters, for the purpose of hydrogeologic dating of groundwater by uranium isotopic disequilibria. The isotope 238 is a parent of 234 and is less mobile than its daughter isotope. Surplus of ^{234}U could be justified by the higher mobility, due to the high efficiency to product UO_2^{2+} (highly soluble) than ^{238}U (which prefers oxidation state IV, almost insoluble).

The most sophisticated models attempt to describe the transport of the

uranium series radionuclides by including sorption and precipitation processes in the transport equations (Harmon, 1992).

1.1.3 Uranium sorption on mineral surfaces

Sorption is a chemical-physical process, often reversible, that describes the behavior of ions and atoms when they interact with the interface surface by Van Der Waals forces or by electrostatic forces (physical sorption) or else by chemical bindings (chemical sorption).

In a two-phase system, we define the constant of the equilibrium distribution $K = C_1/C_2$, where C_1 and C_2 are the concentrations of the sorbate in the two phases, in equilibrium conditions (Giammar, 2001).

The most common model is Langmuir adsorption model. It is used to quantify the amount of *adsorbate adsorbed on an adsorbent* as a function of partial pressure or concentration at a given temperature. It considers adsorption of an ideal gas onto an idealized surface. The gas is presumed to bind at a series of distinct sites on the surface of the solid, and the adsorption process is treated as a reaction where a gas molecule reacts with an empty site to yield an adsorbed complex. In this case, each site has the same probability to be occupied.

At low concentrations, the relationship between dissolved and sorpted species is linear; for higher concentrations, surface saturates and the concentration of sorpted species tends to an upper limit (single layer covering).

More rigorous interpretation of sorption behavior can be obtained by changing the theoretical surface of the model (Giammar, 2001).

In natural systems like aquifer, chemical and physical processes influence the kinetics of sorption of species in solution near mineral surfaces.

Chemical sorption of heavy metal's ions on the soil's minerals is usually a fast process (that occurs on a ms time scale). However, this initial fast sorption is normally followed by a slower sorption (that lasts for some days). Slow chemical sorption has been explained as the coordination of a metal to the mineral surface to form an inner-sphere complex, which occurred on a time-scale of hours to tens of hours (Giammar, 2001).

Regarding iron oxyhydroxide, Uranium(VI) sorption occurs through the formation of inner-sphere surface complexes, which frequently have bidentate coordination to the mineral surface. Sorption increases from essentially none to a maximum value across a sharp sorption edge around pH values of 4-6. In presence of carbonate, sorption decreases at higher pH because of formation of uranyl-carbonate complexes (Giammar, 2001).

Sorption on goethite can be enhanced by the addition of citrate, probably through the formation of a ligand-bridging ternary surface complex (Jenne,

1998). In these studies, the sorption of uranium on goethite is considered as a reversible phenomenon; however, uranium sorption is not entirely reversible in the presence of a crystallizing goethite (Ohnuki et al., 1997).

Maximum sorption of uranium on goethite (FeO(OH)) in open systems occurs between pH values of 5-6 with the decrease at higher pH values.

Surface complexation modeling of the uranium-hematite (Fe_2O_3) system has been performed in numerous studies. Although sorption on hematite does decrease with increasing carbonate concentration, spectroscopic and electrophoretic mobility data indicate that uranyl-carbonate surface complexes are formed with bidentate coordination to the hematite surface.

Ferrihydrite, an iron oxyhydroxide that can transform to form goethite and hematite, also has a high sorption affinity for uranium (Giammar, 2001).

1.2 Earth Mantle and CO_2 lithosphere-asthenosphere degassing beneath the Western Mediterranean region

Earth Mantle occupies about 84% of Earth's volume. It's composed essentially of ultraphemic rocks, stable at high temperatures, rich of Fe and Mg. The upper limit of Earth Mantle is between 10 km and 35 km of depth and it's called Mohorovicic discontinuity (Moho). This is revealed by the change of the seismic waves velocity. The lower limit is at about 2890 km deep and it is called Gutenberg discontinuity (Anderson, 1989).

The uppermost part of the Mantle is rheologically rigid. Together with the Earth Crust, it composes the lithosphere (80-200 km deep). The inner part has plastic characteristics and it composes the asthenosphere. This plastic behavior is an integral part of the motion of plates. Lithospheric plates float on the asthenosphere, interacting with themselves and with the asthenosphere.

Mantle is different from the Crust and the Core, because of its seismic, rheological and mechanical features. These features are directly connected with chemical composition (mineralogy) and physical properties.

Mantle's rocks up to 400 km deep are mainly composed by olivine, pyroxenes, spinel-structure minerals, and garnet (Anderson, 1989). The mineral olivine (also called peridot and chrysolite) is a magnesium iron silicate with the formula $(Mg^{+2}, Fe^{+2})_2SiO_4^{4-}$. Pyroxenes are single chains of groups SiO_4^{4-}, combined by sharing oxygen; spinel is a mineral composed by Mg and Al ($MgAl_2O_4$); garnets are a group of silicate minerals, identified by the formula $X_3Y_2(SiO_4)_3$, where X is a divalent cation (Ca^{2+}, Mg^{2+}, Fe^{2+}) and

Y is a trivalent cation (Al^{3+}, Fe^{3+}, Cr^{3+}) in an octahedral or tetrahedral structure.

The typical rocks are thought to be peridotite, dunite (olivine enriched by peridotite), and eclogite.

Below 400 km depth, olivine is no longer stable and it is replaced by polymorphic materials, with similar composition (wadsleyite e ringwoodite). Under 650 km deep, all Mantel composites become unstable. The most abundant materials are similar to perovskite.

Mineralogical changes between 400 and 650 km produce characteristic signals on seismic records (similar to the Moho) and they are revealed by seismic waves. These changes in mineralogy can influence convection processes because of different densities; besides, they can absorb or release latent heat, as well as to reduce or to elevate the depth of polymorphic phase transitions in regions at different temperatures.

The trend of mineralogical changes versus depth has been studied by means of laboratory experiments, with the aim of reproducing high pressure of the upper Mantle (Anderson, 1989; Jackson, 2000).

The temperature in the Mantle varies from 500°C up to 900°C close to the top end, while it is over 4000°C near by the bottom end (close to the Core boundary). These temperatures are much higher than the melting point of Mantle rocks; nevertheless, the Mantle is mainly solid: in fact, the melting temperature varies with pressure, so melting processes are inhibited by the large weight of the lithostatic pressure.

The upper Mantle is not isotopically and chemically homogeneous.

Because of the geochemical fractionation, there are variations in isotopic composition. This is due to the formation of magma after subduction processes: the melting of a polycrystalline material in particular P-T conditions. The melting is controlled by the partial melting parameter F. Elements are categorized in solid state and liquid state, by the coefficient $D_i = C_{s,i}/C_{l,i}$, where $C_{s,i}$ and $C_{l,i}$ are the concentration in solid and liquid of the element i, respectively (Allègre and Sutcliffe, 2008).

Some elements are called "incompatible elements". In this case, D value is very low. For these elements is

$$C_{l,i} \simeq \frac{C_{s,i}(0)}{F} \tag{1.1}$$

where $C_{s,i}(0)$ is the initial concentration of the element in the solid, F is the partial melting parameter. The lower is F, the most concentrated is the liquid. This implies that ratio between the concentration of two elements i and j is always constant in case of partial melting:

$$\frac{C_{l,i}}{C_{l,j}} = \frac{C_{s,i}}{C_{s,j}} \tag{1.2}$$

This is true only for heavy elements (Th, U, Nd, Rb, Pb) with a low distribution coefficient D, only in particular conditions (Allègre and Sutcliffe, 2008).

The geophysical and petrological models show how efficient is the carbon cycle in upper mantle, beneath the western Mediterranean regions and Italy.

Decarbonation or melting of carbonate-rich lithologies from a subducted lithosphere may affect the efficiency of carbon release in the lithosphere-asthenosphere system.

Melting of carbonated lithologies, induced by the progressive rise of mantle temperatures behind the eastward retreating Adriatic-Ionian subducting plate, generates low fractions of carbonate-rich melts (Frezzotti et al., 2009). These melts contain from a hundred up to a thousand times the concentration in noble gases, heat-producing elements (e.g. U, Th, K and other incompatible elements) than the primitive mantle.

The generation and evolution of deep-mantle derived CO_2 has been delineated integrating surface wave tomography with experimentally determined melting relationships for carbonated peridotite and crustal lithologies, relevant to recent mantle processes in the Western Mediterranean region.

Melting of sediments and/or continental crust of the subducted Adriatic lithosphere at pressures greater than 4 GPa (120 km) and temperatures of 1200°C generate carbonate-rich melts. Such melts are very mobile, due to their low viscosity and density, so they migrate upward through the mantle and form a carbonated partially molten layer recorded by tomographic images between 70 and 160 km of depth (Plastino et al. (2011) and references therein).

When carbonate-rich melts start to be out of their P-T stability field (e.g. at depths less than 60-70 km), they produce a massive outgassing of CO_2 in the lithosphere. Buoyancy forces allow the upwelling of the fluid through deep lithospheric faults (also favored by the fluid overpressure), especially where the continental crust is thin (Frezzotti et al., 2009). Figure 1.3 reports a summary of recent CO_2 emission measurements in Italy, based on literature data. Active volcanoes represent a prominent natural source of CO_2. Degassing of "cold" CO_2 in areas where volcanism activity is absent or no longer active, occurs via diffuse soil emission associated with fault and fractures often of deep origin.

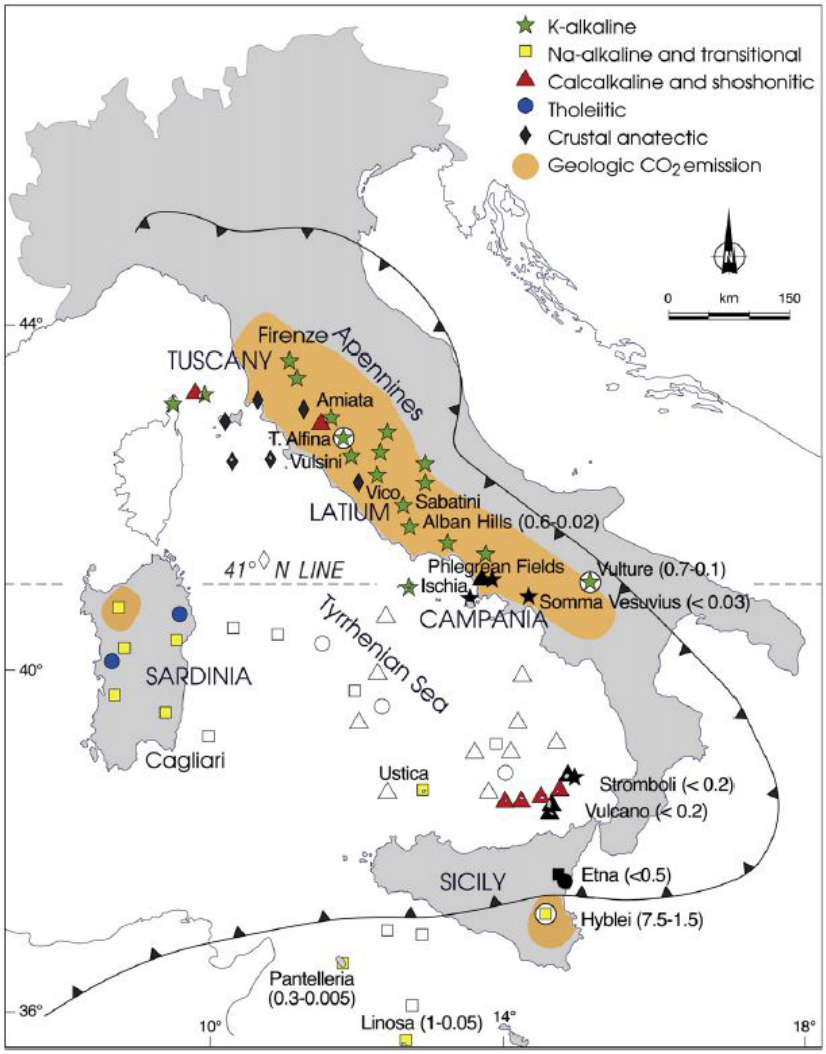

Figure 1.3: Distribution of main geological CO_2 emission in Italy (gray area), as derived from the on-line catalog of Italian gas emissions, INGV-DPCV5 project (http://googas.ov.ingv.it), and of petrochemical affinities and ages of the main Plio-Quaternary magmatic centers in Italy, modified from Peccerillo (2005). Volcanic centers marked by white circle bear peridotites. Active volcanoes are marked in black. Open symbols refer to outcrops below the sea level. Ages in parenthesis (Frezzotti et al., 2009).

1.3 ERMES Experiment at LNGS-INFN

Gran Sasso National Laboratory (LNGS-INFN) is one of the four INFN national laboratories. It is the largest underground laboratory in the world and

it is located under the Gran Sasso massif, more precisely below the Mount Aquila, between the towns of L'Aquila and Teramo, about 120 km far from Rome. The Laboratory hosts experiments that require a low background environment in the fields of astroparticle physics and nuclear astrophysics and other disciplines that can profit of its characteristics and infrastructures.

The underground facilities are located on a side of the ten kilometers long freeway tunnel crossing the Gran Sasso Mountain. They consist of three large experimental halls (A, B and C), each about 100 m long, 20 m wide and 18 m high and service tunnels, for a total volume of about 180000 cubic meters. The temperature inside is about 6-7 ° C.

The headquarters and the support facilities, among which offices, different services, library and canteen, are located in the external building. The Gran

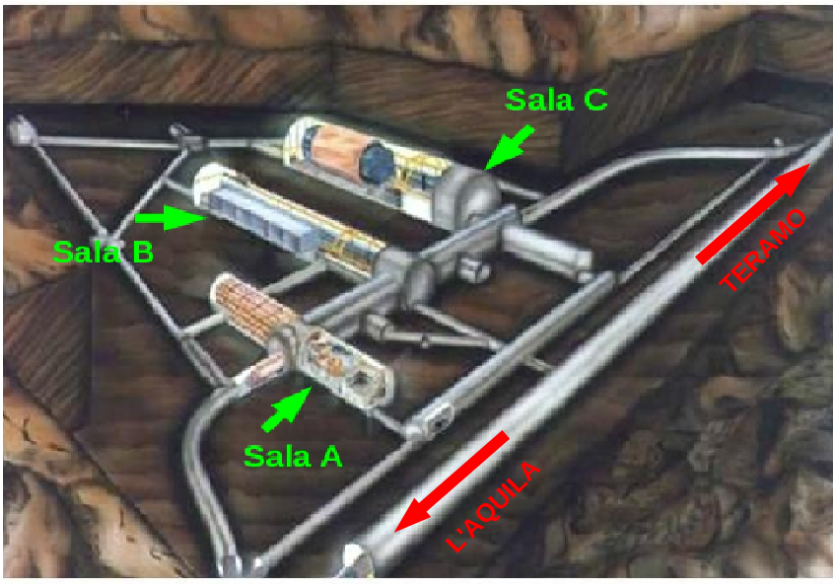

Figure 1.4: Gran Sasso National Laboratory: underground facilities

Sasso National Laboratory is located inside the largest aquifer of the Central Italy. The hydrological and hydrogeological properties have been monitored and studied during construction of the highway tunnel and LNGS-INFN. These studies have emphasized a complex structure of aquifer due to geological and lithological settings. The presence of semi-permeable and / or impermeable structures produce different hydrological and geochemical patterns in the various compartments of the aquifer.

Within the framework of the LNGS-INFN scientific program ERMES (Environmental Radioactivity Monitoring for Earth Sciences) radon (^{222}Rn),

radiocarbon (^{14}C) and tritium (^{3}H) are monitored in the groundwater inside the LNGS-INFN, and different chemical, physical and fluid dynamical characteristics of groundwater are detected.

The radioactivity of the materials used for the experiments has been studied in detail during the last few years. Unfortunately, not many information about hydrological properties of the rocks due to the water-rock interactions are available in literature.

Preliminary measurements of radon, radiocarbon and tritium in groundwater have shown different chemical-physical properties, associated to different percolation effects concerning snow melting or abundance of rain.

The uranium groundwater monitoring started on June, 2008 with the aim of better defining the ^{222}Rn groundwater transport processes through the cataclastic rocks as well as to check its contribution to the neutron background at the LNGS-INFN. In fact, neutrons from cosmic radiation are properly shielded by dolomite and flint rocks (1400 meters of overlying rocks are equivalent of 3100 meters of equivalent water (mwe)), while the contribution of the spontaneous fission of rocks and water inside the underground facilities is under investigation.

The uranium content detected in four different sampling sites (see section 1.3.1) have shown different features (Ciarletti, 2011). Two distinct groups of water could be identified: the former (E3 and E3dx) has shown higher content of uranium and a strong variation, the latter (E1 and E4) showed lower content of uranium and a milder variation (Plastino et al., 2011). The uranium groundwater content followed a seasonal trend, with the exception of some anomalous values observed until March, 2009.

One month later, on April 6th, 2009, at 01:33 UT, a violent earthquake ($M_W = 6.3$) occurred near L'Aquila (epicenter identified at about 18 km from LNGS-INFN). Seismic activity continued during the following days with two main aftershocks of magnitude $M_W = 5.2$ and $M_W = 5.4$, occurred north and south-east respect to the main shock, respectively.

The uranium content detected until March 31st, 2010, allowed Plastino et al. (2011) to distinguish two different time spans. Period A (23/06/2008-31/03/2009): spike trend, correlation between uranium and sodium, magnesium, potassium and calcium contents; Period B (10/04/2009-31/05/2010): disappearance of the spike trend, no correlation between uranium and sodium, magnesium, potassium and calcium contents (see Figure 1.5).

1.3.1 Groundwater sampling sites

A series of tectonic events going from the end of the upper Miocene until the Pleistocene produced a complex structure, crossed by three main faults.

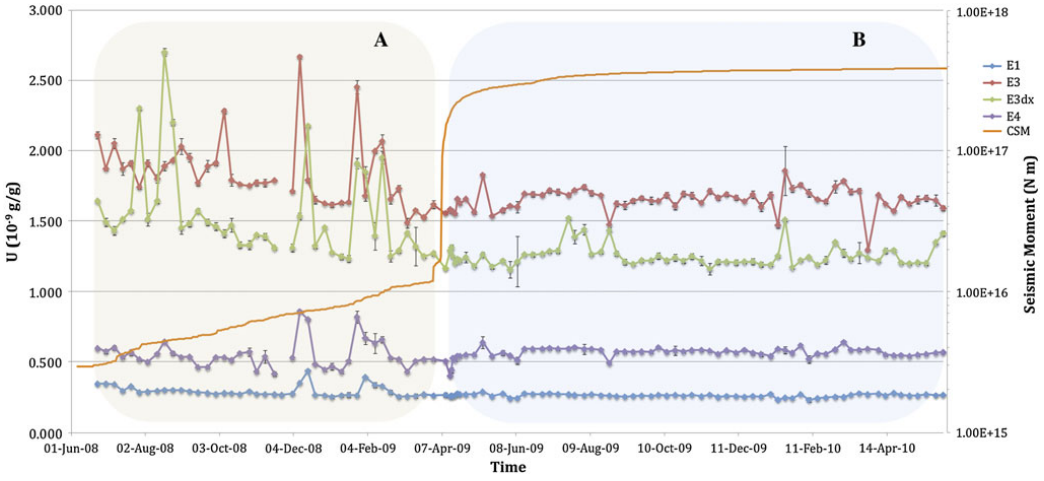

Figure 1.5: Trend of uranium concentration (relative accuracy $\pm 5\%$), regarding Period A and B, detected in sites E1, E3, E3dx and E4, related to cumulative seismic moment ($ln(M_0) = 1.85M_l + 27.2$) calculated by data provided by INGV-Istituto Nazionale di Geofisica e Vulcanologia. A spike trend is evident in Period A, but not in Period B (Plastino et al., 2011).

Geological and hydrogeological structures are shown in Figure 1.6.

As previously stated, LNGS-INFN is located inside the largest aquifer of central Italy within the limestone formation of the upturned syncline, near the main overthrust fault (Plastino et al., 2010b). This fault actually divides water masses belonging to two distinct flowpaths: the former (sites E1 and E4) flows in well drained cretaceous formation (where the main laboratories are excavated), while the latter (sites E3 and E3dx) is within not drained and poorly permeable dolomitic formations (Plastino, 2006).

Groundwater samples have been collected weekly in sites E1, E3, E3dx and E4, located inside the LNGS-INFN underground laboratories as it is shown in Figure 1.7.

Collected groundwater are stored in 1L cleaned polyethylene bottles, after 5 minutes of water flushing at maximum flow. The analysis is performed by ICP-MS technique and it is explained in detail in Chapter 2.

Concerning site E3, two different regions are investigated: E3 is parallel to the main overthrust fault, northward; E3dx is orthogonal to the fault, toward E4. Site E3dx is very significant, thanks to its position (it is the nearest site to cataclastic rocks (Plastino et al., 2013)). It is also characteristic for a better description of water-rock interactions through the main overthrust fault.

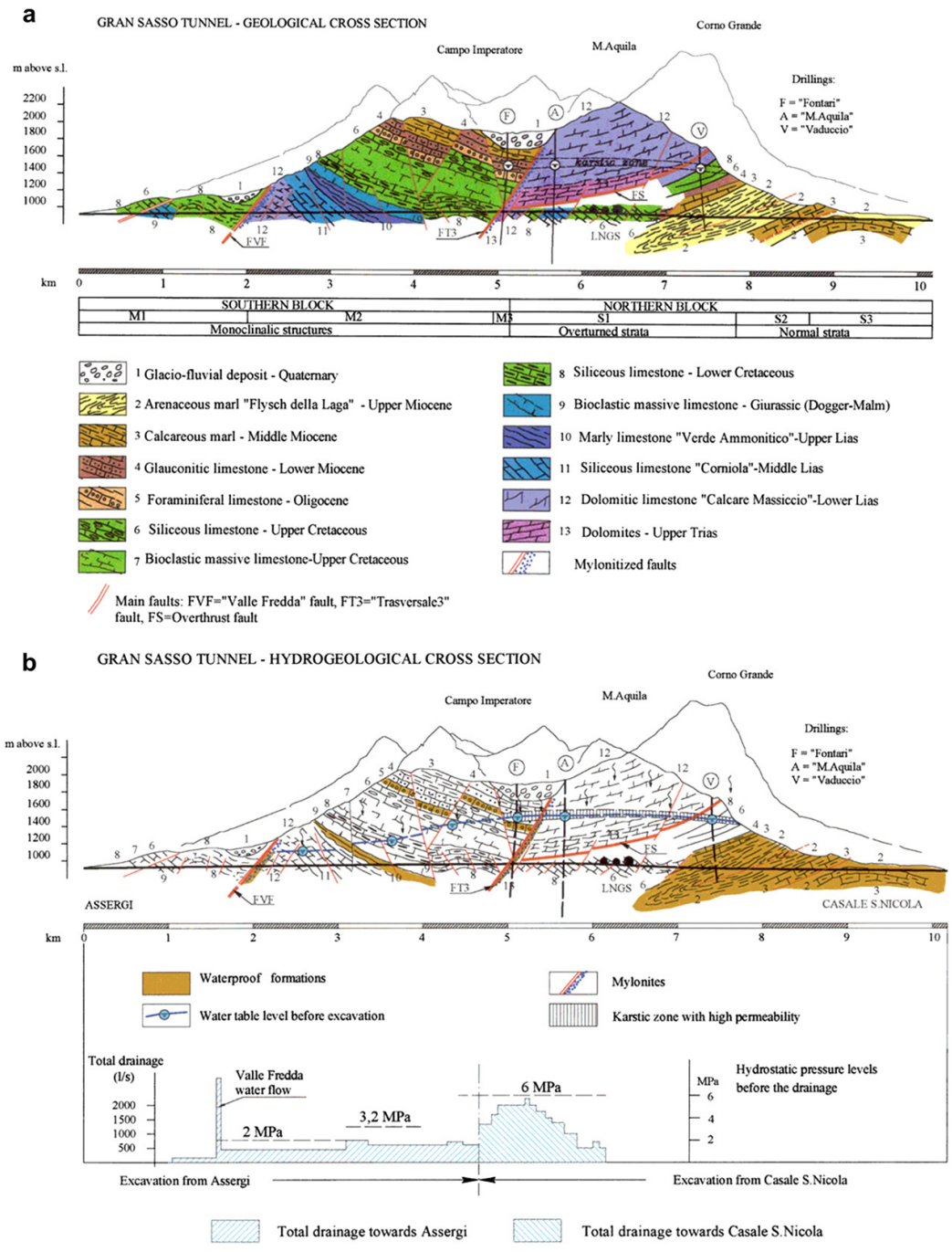

Figure 1.6: The Gran Sasso massif: schematic view of geological (a) and hydrogeological (b) cross sections. LNGS-INFN is also shown (Plastino et al., 2010b).

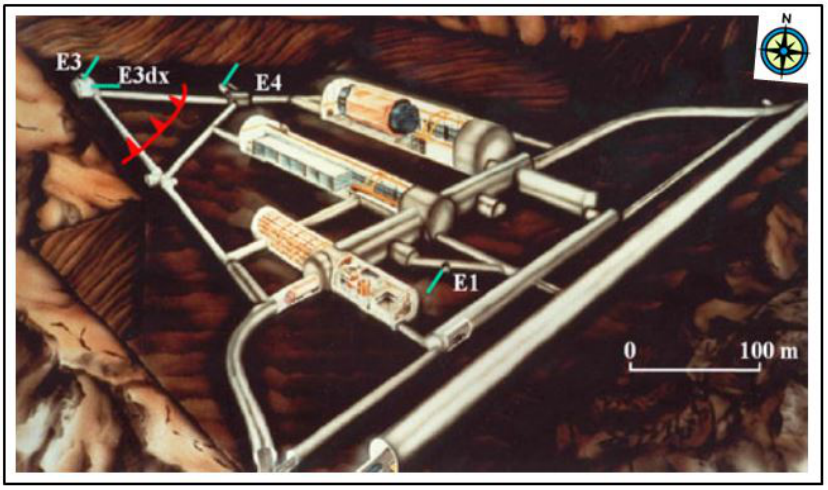

Figure 1.7: Schematic view of the LNGS-INFN. The overthrust fault (red line) and monitoring sites E1, E3 and E4 are also shown. At site E3 there are two sampling points: E3 which is parallel to the overthrust fault in the North direction; and E3dx which is orthogonal to the fault in the E4 direction into the cataclastic rocks.

Chapter 2

Inductively Coupled Plasma Mass Spectrometry (ICP-MS) and uranium content detection

Mass Spectrometry (MS) is an analytical technique that produces spectra of the masses of the atoms or molecules constituting a sample of material. The spectra are used to determine the elemental or isotopic signature of a sample.

Inductively Coupled Plasma Mass Spectrometry (ICP-MS) consists in ionizing the sample with inductively coupled plasma and then in using a mass spectrometer to separate and to quantify those ions. It is one of the most employed techniques in chemical analysis. It is based on analysis and detection of mass/charge ratio of ions formed from atoms or molecules, which are accelerated by subjecting to a electric or magnetic field.

ICP-MS uses a plasma torch as ion source and a mass spectrometer for the analysis and the survey. The main feature of this technique consists in the identification and analysis of almost every element in the periodic table, even for very low concentration of ions (from 10^{-6}g/g up to 10^{-9}g/g in general, up to 10^{-15}g/g for high resolution instruments).

A further advantageous aspect is the possibility of a satisfying analysis of non-metal elements.

In general, ions and molecules are identified with high accuracy and precision (Taylor, 2001).

This technique was born in the 60's. At the beginning it was called Atomic Emission Spectrometry, but Taylor (2001) demonstrated how useful is the combination of a plasma source and a MS.

By means of an analytical nebulizer, the liquid sample is converted in aerosol and it is carried to the plasma source by a gas carrier, usually argon. The sample is atomized, than ionized. The quantity of ions inside the plasma

is proportional to the quantity of analyte in the sample (Taylor, 2001).

If the temperature of the plasma is high (10000 K) and the sample remains within the plasma for few milliseconds, then a satisfying ionization process is guaranteed (Nidasio, 1994/1995).

Ions are then extracted from plasma and separated by a mass analyzer. A mass analyzer is a mass filter with the aim of isolating one specific ion (identified by a specific mass/charge ratio) from the main ions beam. The common analyzers are: quadrupole mass analyzer, double focusing systems (with single or multiple collectors), time-of-flight systems (with axial or perpendicular accelerator).

After the separation, ions beams are sequentially (single collector) or concurrently (multiple collector) directed to a detector for quantifying (by means of the ions current) each analyte of the initial sample.

Resolution Power

The *Resolution Power (RP)* is one of the most characterizing parameters of a Mass Spectrometer. This feature quantifies the capability of separating adjacent mass regions within the mass spectrum (Taylor, 2001).

The RP can be defined as:

$$RP = \frac{m}{\Delta m} \tag{2.1}$$

where m and $m+\Delta m$ are the values of the mass/charge ratio of two adjacent peaks of the mass spectrum.

The resolution of a Mass Spectrometer depends on two main factors: the analyzer and the experimental conditions. It can be classified in three main categories: low resolution (RP ranges from 100 up to 1000); medium resolution (RP ranges from 1000 up to 5000); high resolution ($RP \geq$5000) (Watson and Sparkman, 2008).

The numerical value RP can be determined from both the form and the amplitude of two adjacent peaks. In the first case, two equal height adjacent peaks (relative to the masses m and $m + \Delta m$) are considered as resolved in the mass spectrum if the mean height of the secondary peaks between the two main peaks is lower than 10% of the height of the main peaks. In the second case, m represents the mass/charge ratio of the main peak, Δm its amplitude (measured at a specific height) (Becker, 2008).

Sensitivity

A signal requires a minimum number of particles in order to be revealed. The *sensitivity (S)* is the ratio of net signal to concentration and it represents the

minimal value detectable by the instrument:

$$S = \frac{\Delta V_{mis}}{\Delta V_{re}} \tag{2.2}$$

where ΔV_{mis} is the variation of measured value and ΔV_{re} is the variation of the real value.

Detection Limit

The value of the *Detection Limit (DL)* for a particular element can be determined by means of a standard solution containing that element:

$$DL = \frac{3\sigma_B}{(cps)_E - (cps)_B} \cdot X \tag{2.3}$$

where $(cps)_B$ and $(cps)_E$ are the counts/s measured in the blank solution and in the standard solution, respectively; σ_B is the standard deviation of $(cps)_B$; X is the concentration of the element in the standard solution (Di Vacri, 2008/2009).

Interferences

Everything that can affect the measurement of the ions current of the analyte under consideration, is called *Interference*.

Interferences can be divided in two categories: Spectral effects and non-Spectral effects. The former are, for example:

- Isobaric Interferences: isotopes of different elements, both atoms and molecules, can have the same mass value.
  -Ions from atoms generally interfere with other ions already in the sample, or in the gas carrier. For example, argon has the main isotope at m/z=40 (99.6%), so it can interfere with $^{40}K^+$ and $^{40}Ca^+$.
  -Polyatomic ions (oxides, hydrides, hydroxides) can be produced in the plasma by sample matrix, gas carrier components and solvents used in the preparation of the sample.

- Double charge ions: some elements have a low ionization potential: they can produce double charge ions, detected as single charge ions with half mass.

Non-Spectral Effects are those chemical or physical effects which cause a decrease or an increase of the ionic current. For example:

- Matrix effects: the decrease or increase of ionic current is caused by the high concentration of the matrix elements (low ionization efficiency).
- Effects of the solid dissolved in the sample: they can modify the ionic current of the analyte (Cavalli, 2004).

2.1 ICP-MS at Gran Sasso National Laboratory

Gran Sasso National Laboratory provides different types of ICP-MS.

For our purpose we use the 7500a from Agilent Technologies, equipped with a quadrupole analyzer. A description of the main components is provided below.

2.1.1 Spray chamber

The sample consists in an aqueous acidified solution. It is introduced by means of a peristaltic pump. A nebulizer converts the liquid sample on aerosol: the tiny drops are hanged up in the gas carrier. The nebulization of the sample permits to maximize the ionization process inside the plasma torch (Taylor, 2001).

A schematic representation of a *spray chamber* is provided in Figure 2.1. The nebulizer produces tiny drops of the sample. The spray chamber is provided by a cooling system, that permits to discard big drops (condensing on the side), and to admit small drops to the torch. This system ensures uniform size for the drops. Argon is used as gas carrier for different reasons: it is inert, not much expensive, available at high purity levels. Furthermore, its first ionization energy ($15,75$ eV) is high, being a noble gas, and it is situated between the first and the second ionization energy of many chemical elements. Therefore, it permits the first ionization and reduces the second. For this reason, it is considered a good ionizing gas.

2.1.2 Plasma ion torch

The *Plasma ion torch* (Figure 2.2) is composed of three coaxial tubes, through which argon flows. The gas in the external tube operates as a cooling gas; argon inside the intermediate tube is called "supporting gas" and it drives the plasma to the upper part of the internal tube, to avoid overheating (Becker, 2008).

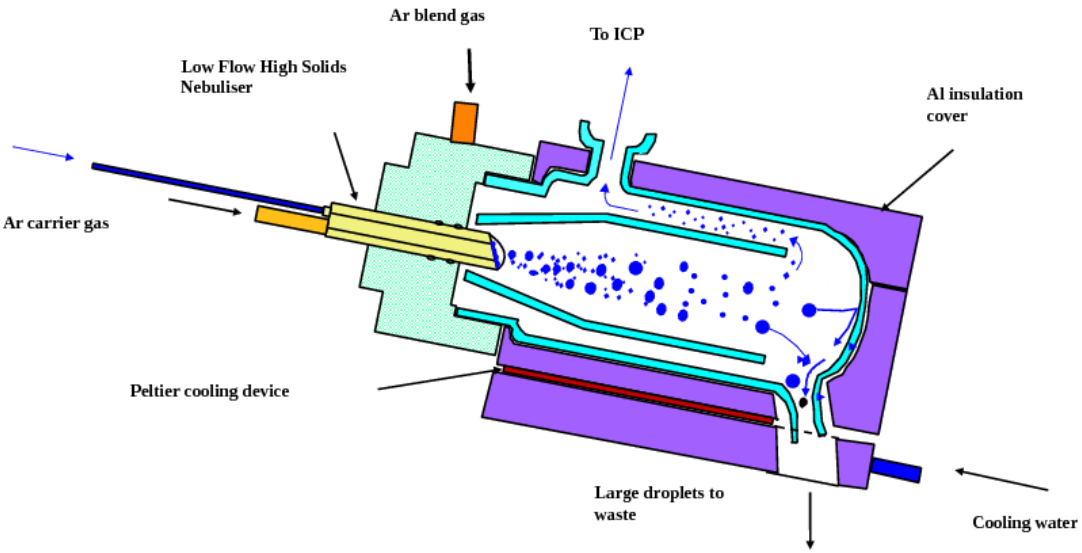

Figure 2.1: Schematic of a spray chamber.

The sample is carried by the internal tube by means of the gas carrier. Differently from both the "cooling gas" and the "supporting gas", the gas carrier needs to flow homogeneously, to guarantee the stability of the plasma (Di Vacri, 2008/2009). By means of a radio-frequency generator, electric power flows through induction coils encircling tubes, which produces an oscillating electromagnetic field.

After sparking the plasma, argon electrons are disassociated, then they are accelerated by the oscillating magnetic field and they collide with atoms and molecules for argon ionization.

The temperature of the plasma and the ionization efficiency depend on the choice of the experimental parameters. Generally, the temperature of the plasma reaches 5000-8000K, while the temperature of the excited atoms is lower. Temperature of electrons is about 8000-10000K (Becker, 2008).

Therefore, summarizing:

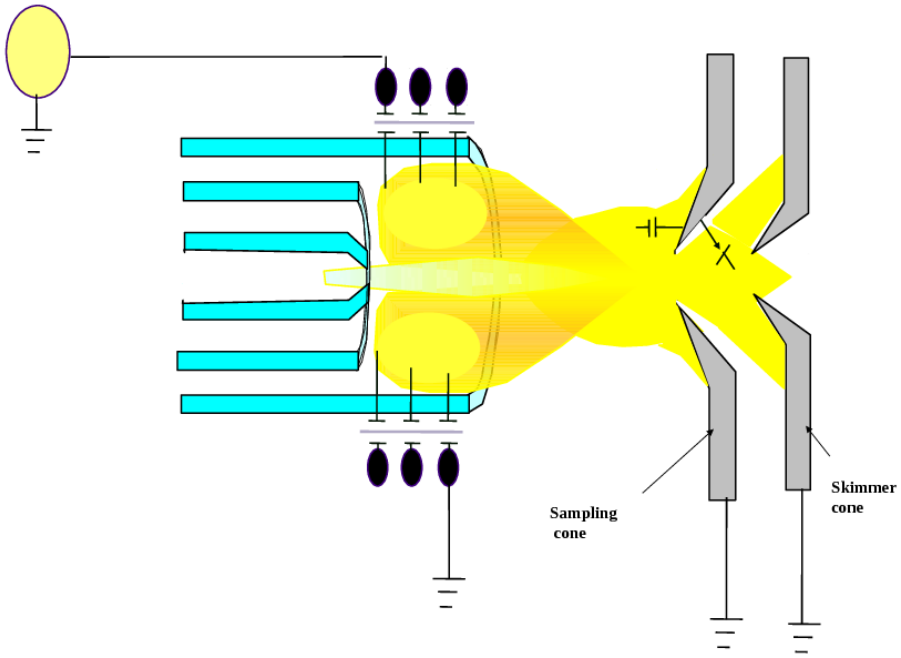

Figure 2.2: Schematic of a plasma torch.

- accelerated electrons ionize argon

$$Ar + e^- \rightarrow Ar^+ + 2e^- \tag{2.4}$$

- argon ions recombine with electrons, producing excited argon atoms and photons

$$Ar^+ + e^- \rightarrow Ar^* + h\nu \tag{2.5}$$

This process can cause a raising of instrumental background. Also the contribution of bremsstrahlung needs to be taken into account (high energy electrons, if accelerated, can produce electromagnetic radiation).

The main ionization processes of an analyte are:
-electronic ionization $M + e^- \rightarrow M^+ + 2e^-$
-ionization with charge transfer $M + Ar^+ \rightarrow M^+ + Ar$
-Penning ionization $M + Ar^{m*} \rightarrow M^+ + Ar + e^-$.
Excited metastable species, as Ar^{m*} or M^*, exist in the argon plasma because of:
-excited electrons of the atoms $M + e^- \rightarrow M^* + e^-$
-excited electron of argon $Ar + e^- \rightarrow Ar^* + e^-$
-recombination electron-ion $M^+ + e^- \rightarrow M^* + h\nu$.

Ionization efficiency of an ICP source depends on the ionization energy of the analyte. The higher the first ionization energy, the lower the ionization efficiency (Becker, 2008).

2.1.3 Interface region and ion optics

The main aim of the *interface region* is to extract ions produced in the plasma source at atmospheric pressure and high temperature and to drive them through the vacuum region of the mass analyzer.

There are two metal coaxial cones (Figure 2.3). The one nearest to the interface is called "extraction cone" or "sampler cone". It has a 1 mm diameter hole and ions produced by the source pass through it.

Then the beam is directed to the quadrupole, passing through the hole of the second cone (with a diameter <0,5 mm), called "skimmer cone", located just behind the first one.

In order to pass from the atmospheric pressure region to the analyzer region, two vacuum pumps are required. Vacuum between the extraction cone and the skimmer cone is ensured by a rotary pump. the region behind the skimmer cone is the second vacuum region. Pressure is changed to the optimal value for the analyzer by means of a turbomolecular pump.

Next to the skimmer cone, there are a photon-stop and ion lens. The photon-stop is a beam deflector, which inhibits photons and neutral particles produced in the plasma to reach the detector (for a lower background).

The ion lens collimate and focus the beam to the analyzer.

2.1.4 Analyzer: quadrupole

A quadrupole mass analyzer is represented in Figure 2.4.

It is based on four parallel cylindrical metal bars (electrodes), placed parallel to the ion beam direction. They are separated two by two by the distance $2r_0$.

The beam passes exactly through the center of the four bars.

Applying concurrently both a direct current (DC) potential E and a radio-frequency (RF) potential to the two couples of bars, then a mass filter is created. In fact, the applied potential is

$$U_0 = +(E - Vcos(\omega t))$$

for a couple of bars and

$$-U_0 = -(E - Vcos(\omega t))$$

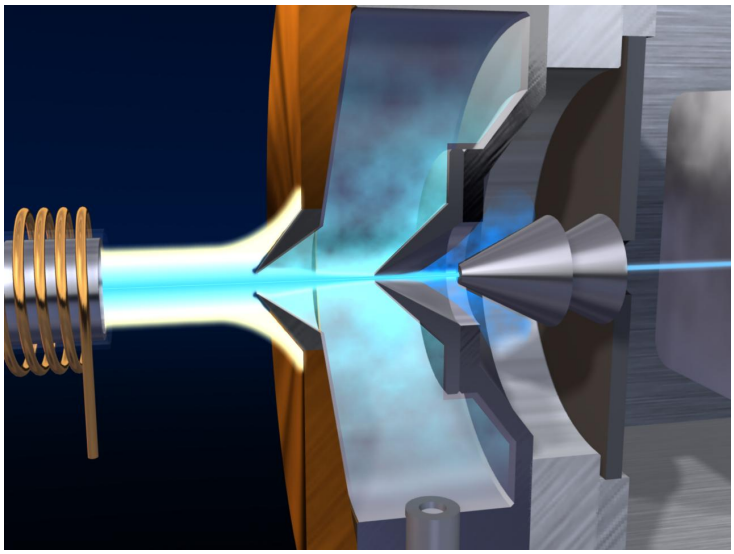

Figure 2.3: Schematic view of the interface region.

for the other couple. V is the amplitude of the RF potential, ω is the angular frequency; opposite electrodes of the quadrupole have the same sign potential.

The electric potential maintains ions in a linear central trajectory. The radio-frequency potential induces an oscillating motion: the ions beam is therefore deflected in a spiral motion, with a radius depending on the applied potential.

If we call z the direction of the motion, the electric potential $U(x, y)$ inside the bars is:

$$U(x, y) = \frac{x^2 - y^2}{r_0^2} U_0 \tag{2.6}$$

where x and y are the coordinates in the (x, y) plane with respect to the central axis, r_0 is the distance between the electrode and the central axis.

The force along x direction is:

$$F_x = -ze\frac{2x}{r_0^2} U_0 \tag{2.7}$$

linearly dependent on the distance from the central axis.

F_x is not dependent on y: the motion along x and y must be considered separately.

Ions motion inside the quadrupole can be described by Mathieu equation.

Along the x direction, the equation of motion is:

$$m\frac{d^2x}{dt^2} = -ze\frac{2x}{r_0^2}\left(E - Vcos(\omega t)\right) \tag{2.8}$$

from which we obtain:

$$\frac{d^2x}{d\xi^2} + \left(a_x - 2q_xcos(2\xi)\right)x = 0 \tag{2.9}$$

where $\xi = \omega t/2$ and a_x, q_x are Mathieu parameters:

$$a_x = \frac{8zeE}{m\omega^2 r_0^2} \qquad q_x = \frac{4zeV}{m\omega^2 r_0^2} \tag{2.10}$$

Concerning ions motion along y direction, the potential has opposite sign: we obtain the same Mathieu relation, changing the sign to Mathieu parameters, $a_y = -a_x$ and $q_y = -q_x$.

Along the x axis, the motion is not affected by the electric field, so the velocity along this axis does not change.

The solutions of the Mathieu equation are divided in "stable" and "unstable" solutions. For each value of the applied electric potential, all the ions hit the quadrupole bars ("unstable" solution, x or y become $> r_0$) except the ones with a specific value of the ratio m/z. Those ions travel steadily along the central axis of the quadrupole, reaching the detector ("stable" solution) (Watson and Sparkman, 2008).

Therefore, the quadrupole selects ions with a particular m/z ratio by the application of an electric potential to the bars: it works as a mass filter.

2.1.5 Detector

The detector is an electron multiplier composed of a series of dynodes. Each dynode is characterized by a potential greater than the previous one. When an electron hits the dynode, one or more electrons are accelerated by the potential difference and then emitted: the signal is significantly amplified and the resulting current is proportional to the number of electrons which initially hit the dynode.

2.2 Sensibility and interferences problems

One of the most problematic issues in mass spectrometry is the chemical preparation of the sample. This process requires care and attention to avoid contamination.

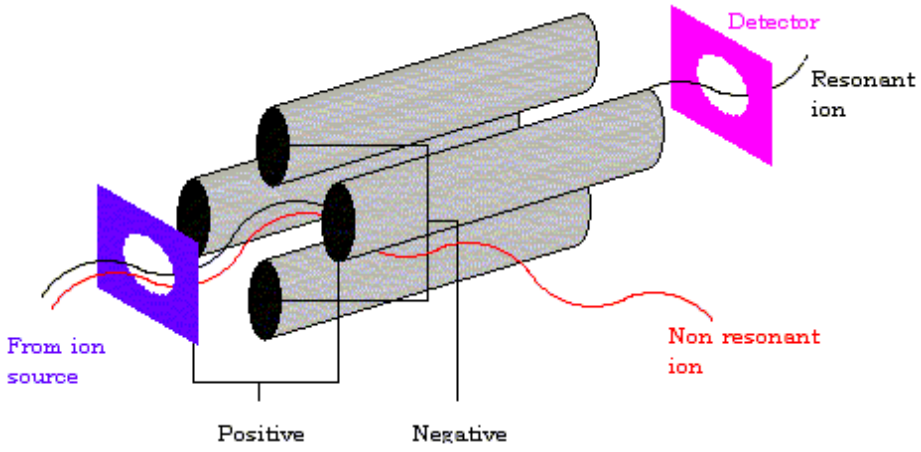

Figure 2.4: Schematic view of a quadrupole mass analyzer.

The reachable sensibility of a mass spectrometer is excellent, this is why it is so important to avoid the contamination of the sample. During the preparation of the sample, the usage of ultra pure reagents is necessary, e.g. special containers as polytetrafluoroethylene (teflon), synthetic quartz, platinum. The usage of contamination control areas is preferred, in order to further reduce the background.

Each sample is introduced into the mass spectrometer in acid liquid form. For this reason, it is necessary to take into account the dilution factor in the estimation of the analyte in the sample. Normally, the dilution factor is 1%. Sometimes a higher factor is necessary, in order to avoid unpleasant deposits on the instrument. A higher dilution factor means sensibility loss. It is possible to avoid those annoying inconveniences using chemical separation methods on the sample or by preconcentration of the analyte.

Isobaric interferences problems represent one more difficulty in mass spectrometry.

The resolution power on a quadrupole mass analyzer ($RP \sim 100$) is not always good to resolve those interferences: sometimes a higher RP is required, this is why a high resolution mass spectrometer is necessary.

A classical example of interference for quadrupole mass spectrometer concerns potassium (K). The interference is caused by the polyatomic species $^{38}Ar^{1}H$.

2.3 Measurement of uranium content

The sample preparation in ICP-MS is a delicate procedure and a careful attention is required.

Groundwater is initially contained into 1L polytetrafluoroethylene bottles. As we stated before, U concentration in the collected samples has been determined by ICP-MS 7500a Agilent Technologies. The instrument is located in a clean room.

Groundwater sampling started on June, 2008. Water is partially poured into 10 ml flasks, after a filtering procedure by 0.45 μm nylon membrane filters with polypropylene housing. A quantity of 250 μl of nitric acid is added to each flask. Only ultra-pure grade acids supplied by Carlo Erba Reagenti (Italy) is used.

Concentrations of U are evaluated by means of a four levels calibration curves: detecting the content of the analytes in standard solutions (of known concentration levels, between 0.2 and 2 ng g^{-1}), the linear functions between instrumental counts and concentration of the analyte is estimated. A 1,000 mg L^{-1} standard solution of U supplied by AccuTrace Reference Standard, USA, was used to prepare all the calibrating solutions.

Analysis is controlled by using also an internal standard solution (100 ng g^{-1} Bi solution): a chemical component which behaves similarly to the analyte to detect is added in known quantities to the samples. The signal of the analyte is then normalized to the signal of the internal standard, in order to attenuate instrumental fluctuations during the analysis.

One minute 2% HNO_3 rinses are carried out between samples, in order to avoid cross contamination due to memory effect in the sample introduction line.

In order to reach high sensitivity, stable signal, and low background, a careful sample preparation is performed and the tuning of the instrument is optimized.

Chapter 3

Analysis of seismicity

The active normal faults of the central Apennines are commonly divided in two parallel sets, a western set and an eastern one. Some of the strongest historical earthquakes have been attributed to the rupture of the western set of normal faults in this area. On the contrary, the eastern set has not been activated in historical times (Falcucci et al., 2011).

Uranium groundwater anomalies, observed before the L'Aquila earthquake (April 6th, 2009) and before the seismic swarm occurred at the end of 2010, were probably associated with geodynamic processes occurring before the earthquake, which may have triggered diffusion processes through the overthrust fault (Plastino et al., 2009).

In this chapter, a quantitative description of temporal variability of seismicity is proposed, which may be eventually correlated with temporal variability of uranium. For this purpose, the normalized energy release and the number of seismic events are analyzed in detail, using monthly sliding time windows. These quantities are compared with uranium anomalies, in order to highlight any possible correlation.

3.1 Environmental setting

3.1.1 Seismogenic Sources

The central part of the Apennines is characterized by extensional tectonics since the Pliocene epoch, with most of the active faults being normal in type and NW-SE trending. At a regional scale, fault systems and individual faults are organized into larger fault sets that run almost parallel to the Apennines chain axis (Akinci et al., 2009). This complex system is described in the Database of Individual Seismogenic Sources (DISS), a repository of geologic,

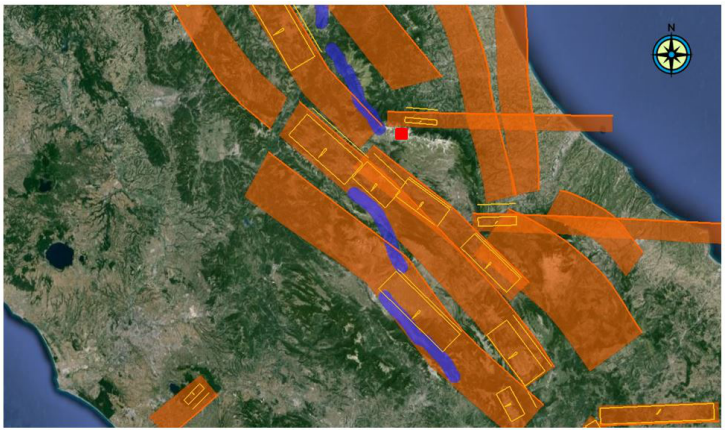

Figure 3.1: Map of central Italy (from Google Earth-CNES/Spot Image-Data SIO, NOAA, U.S. Navy, NGA, GEBCO (2013)). Individual (yellow lines), Composite (orange strips) and Debated Sources (purple bold lines) in the central Italy, based on geological and geophysical data and characterized by geometric and kinematic parameters, identified by Basili et al. (2008). The red dot represents LNGS-INFN.

tectonic, and active fault data for the Italian territory. The Database highlights the results of several decades of research work, with special emphasis on data and conceptual achievements within the past 25 years.

Seismogenic sources of all types are characterized based on the available literature or unpublished original work. This information is organized in summaries of published papers and commentaries on critical issues.

The Individual and the Composite Seismogenic Sources are described by a full set of geometric, kinematic and seismological parameters. A typical Composite Seismogenic Source spans an unspecified number of Individual Sources. The compilers of the DISS database guarantee the existence of all listed Seismogenic Sources, both Individual and Composite, and strive to describe them with the best possible accuracy. Nevertheless, they are well aware that the literature contains hypotheses and descriptions concerning a significantly larger number of potential Seismogenic Sources than those currently listed in the database (Basili et al., 2008). The Individual Seismogenic Sources, together with the composite Seismogenic Sources and the Debated Sources are represented in Figure 3.1.

A seismic swarm affected the area under investigation from October, 2008 to April, 2009, before the main shock of April 6th, 2009, M_W=6.3, M_l=5.9 (Plastino et al., 2011). The main shock was followed by a period of relatively intense seismic activity, associated with aftershocks occurrence. A further moderate size swarm occurred in the second half of 2010, NW of the main

shock epicentral area at a distance of about 30 km. The main event of this swarm was an earthquake with M_l =3.5 on August 31st, 2010, accompanied by five earthquakes with magnitude $M_l \geq$3.0, and by about 100 additional events with $M_l \geq$2.0, which occurred within a small area of 5 km radius, from July to December, 2010. Hence, the swarm is characterized by a quite large number of events, although having fairly small magnitudes (Plastino et al., 2013).

3.1.2 Hydrogeological setting and groundwater flow system

The hydrogeological system formed by the Gran Sasso and the Velino-Sirente mountains occupies a surface of 2164 km^2. This complex system can absorb 714 mm of annual effective infiltration and can give back 49 m^2/s as mean discharge (Bella et al., 1999). The Gran Sasso massif is in the northern part of the system (Boni et al., 1986) and it holds a very large and deep aquifer. The aquifer consists of a series of minor aquifers separated by the main structural discontinuities with values of permeability up to 10^{-4} m/s (A.N.A.S.-CO.GE.FAR., 1980).

The Gran Sasso National Laboratories are located beside the Gran Sasso tunnel. The rocks in the measurement site are mainly composed by detrital limestones and, in particular, have crossed by the overthrust fault which separates the limestones from the dolomite rocks (Plastino and Bella, 2001). Hydrogeological investigations showed that the main springs can be classified in different groups.

After the construction of the tunnels, the aquifer reached a new hydrodynamic equilibrium (Barbieri et al., 2005). From a hydrogeological point of view, the Gran Sasso Underground Laboratory is "immersed" in the saturated zone in the core of the aquifer (Amoruso et al., 2013). By means of the hydrogeological scheme in Boni et al. (1986) a polygon with 25 vertices can be outlined for representing the aquifer, to be used for the following analysis (Figure 3.2). The arrows in the small panel of Figure 3.2 represent the direction of the flowpaths.

3.2 Analysis of seismicity

Aware of the complexity of the region under consideration, our analysis consists in the investigation of the variations in space and time of the seismic pattern around LNGS-INFN.

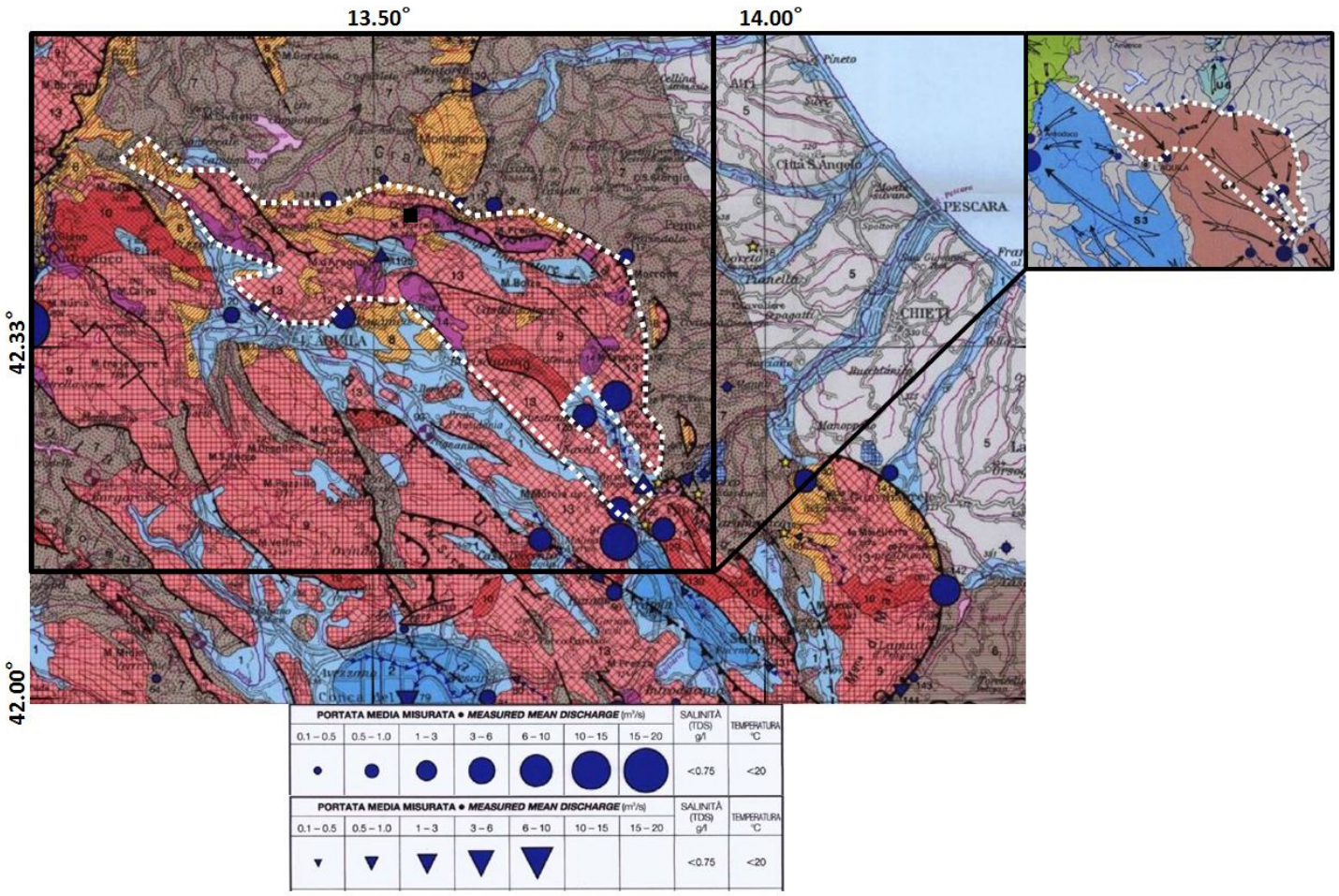

Figure 3.2: Hydrogeological scheme of central Italy, modified from Boni et al. (1986). The white dotted line represents the Gran Sasso aquifer, symbolized by a 25 vertices polygon. The black dot represents LNGS-INFN. Groundwater flow lines are shown by arrow symbols in the small picture. Hydrogeological complex: "light blue" (1) is used for shallow alluvial aquifer, "dark blue" (2) for thick multistata alluvial aquifer. A pattern of "red squares" shows the carbonate infiltration areas (9, 10, 11, 12, 13), where effective infiltration prevails over both surface runoff and evapotranspiration. The mesh is closer where infiltration is higher. "Yellow" areas refer to volcanic complex (4) and marly-calcarentic complex (8), where the effective infiltration preferably occurs in the most fractured hard rocks. "Violet" refers to dolomitic complex (14). Effective infiltration seems to be comparable to that of volcanic complex (4). No data is available regarding surface runoff and evapotranspiration. "Light gray" (5) is used for areas where both surface runoff and evapotranspiration prevail over infiltration. Percolation and aquifer capacity are consequently negligible. "Dark gray" (7) shows the occurrence of limited effective infiltration and diffuse percolation. Hydrological symbols: "blue filled circles" identify springs, considered as a localized natural discharge of ground water emerging in a restricted area. Mean discharge is proportional to the diameter. "Blue filled triangles" identify linear springs, considered as a natural discharge of ground water emerging into a portion of a stream, which varies in length from a few hundred meters to some kilometers. Mean discharge is proportional to the size.

A reliable analysis of the time features of seismicity requires to consider only the complete part of the seismic catalog, thus eliminating the smallest events, which are not systematically recorded.

Furthermore, to guarantee the homogeneity of the catalog, only seismic events occurred after April 16th, 2005 have been considered. On account of the magnitude heterogeneity in the earthquake catalogs available for the Italian territory (namely CSI, BSI and Iside), which has been evidenced by Romashkova and Peresan (2013) and confirmed by Gasperini et al. (2013), we limited our analysis to the BSI bulletins, compiled since April, 2005 and available on line via the Istituto Nazionale di Geofisica e Vulcanologia (INGV) website (iside.rm.ingv.it).

Earthquakes occurred from April 16th, 2005 to September 30th, 2014 have been selected from the Italian Seismological Instrumental and Parametric Data-Base. The completeness of the catalog can be visually determined from the frequency-magnitude distribution, that is considering the linear distribution of the logarithm of the number of earthquakes within each magnitude grouping interval ΔM (Dimri, 2005).

The test has been performed on events occurred in the circular region centered at LNGS-INFN with a radius of 100 km. Figure 3.3 shows the number of events versus magnitude for the whole period of seismic activity. In this case, the catalog can be considered as complete for events with magnitude $M \geq \ M_{min} = 1.5$.

To be sure of the choice of the threshold, we tested the completeness of the catalog considering two different time intervals: before the L'Aquila earthquake and after the L'Aquila earthquake. Figure 3.4 guarantees the stability of the choice of the threshold.

The spatial distribution of the events, from April 2005 to December 2012, considering a circular region centered at LNGS-INFN with radius of 70 km, is shown in Figure 3.5. Intensity of seismic activity, expressed as number of earthquakes, is represented by a colored scale from blue to red, as in Plastino et al. (2013). In this case, the scale ranges from zero (blue color) up to 150 (red color).

At the coordinates 42.270°, 13.495°, the red cluster clearly represents most of the seismic activity occurred near L'Aquila from February to December, 2009.

The energy release E_i for each earthquake i with magnitude M_i has been calculated, and then normalized to the energy E_{min} of the minimum magnitude M_{min} taken into account for the analysis:

$$E_i^* = \frac{E_i}{E_{min}} = \frac{10^{c+dM_i}}{10^{c+dM_{min}}} = 10^{d[M_i - M_{min}]} \tag{3.1}$$

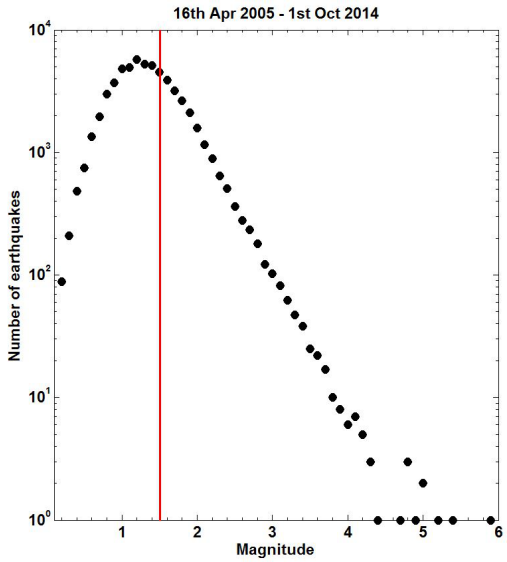

Figure 3.3: Frequency-magnitude distribution of the seismic events. The red line represents the completeness threshold $M_{min} = 1.5$.

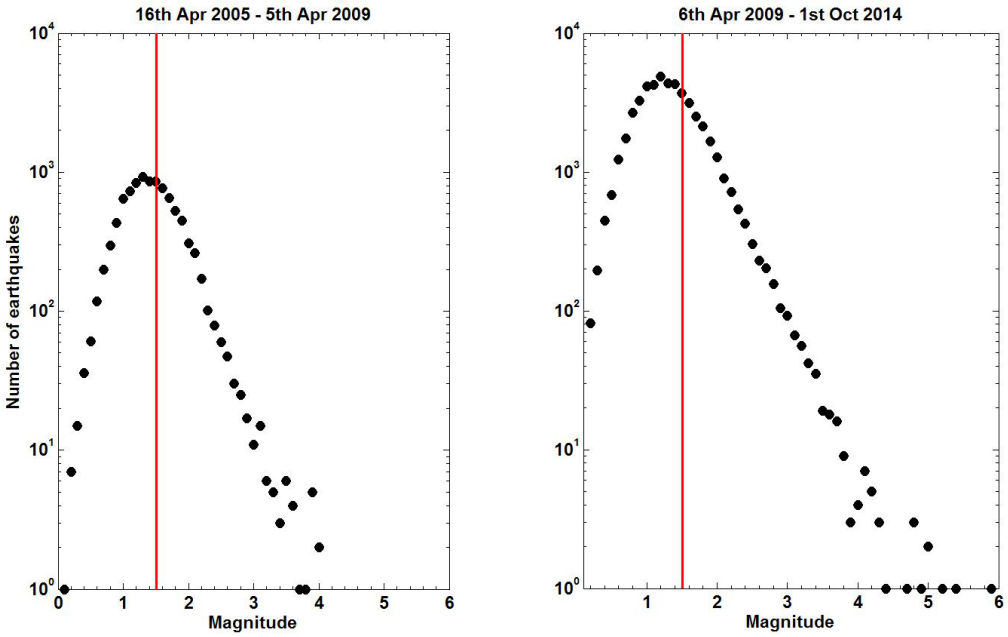

Figure 3.4: Frequency-magnitude distribution of the seismic events, represented before and after the L'Aquila earthquake. In both cases, the catalog can be considered as complete for $M \geq M_{min} = 1.5$.

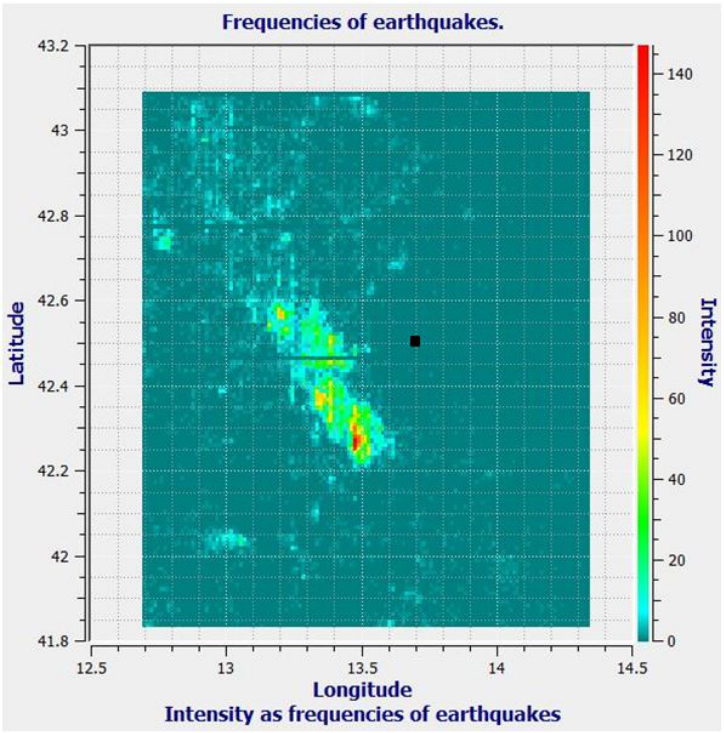

Figure 3.5: Spatial distribution of the events with $M \geq M_{min} = 1.5$, from April 2005 to September 2014, considering a circular region centered at LNGS-INFN with radius of 70 km. Intensity of seismic activity, expressed as number of earthquakes, is represented by a colored scale from blue (no events) to red (150 events). The black dot represents LNGS-INFN.

The considered relationship between the energy and the magnitude of each seismic event has the classical form proposed by Gutenberg and Richter (1956). The use of the normalized energy E_i^* allows us to better highlight the features of seismic activity and to make it less dependent on empirical parameters c and d of the energy-magnitude relation, since only the coefficient d is required. In this study, to be conservative in outlining the trend of the energy release rate, we use the value $d = 1.5$, given by Gutenberg and Richter (1956).

The quantity $E = \sum_i E_i^*$, together with the number of events $N = \sum_i N_i$, has been calculated for monthly sliding time windows, as in De Natale et al. (2004).

Different regions have been properly considered for a better characterization of the seismic source in space and time. Specifically, in this study we considered a set of circular areas centered on LNGS-INFN, which is the observation site for uranium anomalies.

3.2.1 Seismic analysis on circular regions

As previously stated, the main goals of the study of seismicity around LNGS-INFN are the quantitative characterization of seismic energy release in space and time, as well as the investigation of any possible correlation between seismicity and groundwater anomalies.

For that purpose, temporal variation of the number of events and normalized energy release within sliding time windows of one month duration have been calculated ($N_M(t)$ and $E_M(t)$, respectively), considering circular regions centered at LNGS-INFN (42.457°, 13.545°), with values for the radius ranging from 10 up to 70 km, i.e. $R = 10, 20, 30, 40, 50, 70$ km. It is important to underline that our aim is to study seismicity around our groundwater sampling site, in order to identify any possible correlation between uranium groundwater anomalies and local seismicity, independently from our knowledge of the L'Aquila earthquake. To outline the differences between the physical seismic process and the way we observe it from our groundwater sampling site, the same analysis has been applied to circular regions centered at the epicentral coordinates of the L'Aquila main shock (42.340°, 13.380°). This last analysis can only be tested *a posteriori*. The period under investigation is April, 2005-October, 2014. The area under investigation is shown in Figure 3.6.

The non-cumulative area charts allow clearly visualizing the number of events and the seismic energy release, as represented by $N_M(t)$ and $E_M(t)$ in Figures 3.7(a), 3.7(b), 3.8(a) and 3.8(b) in each distance range, for LNGS-INFN and L'Aquila analysis, respectively.

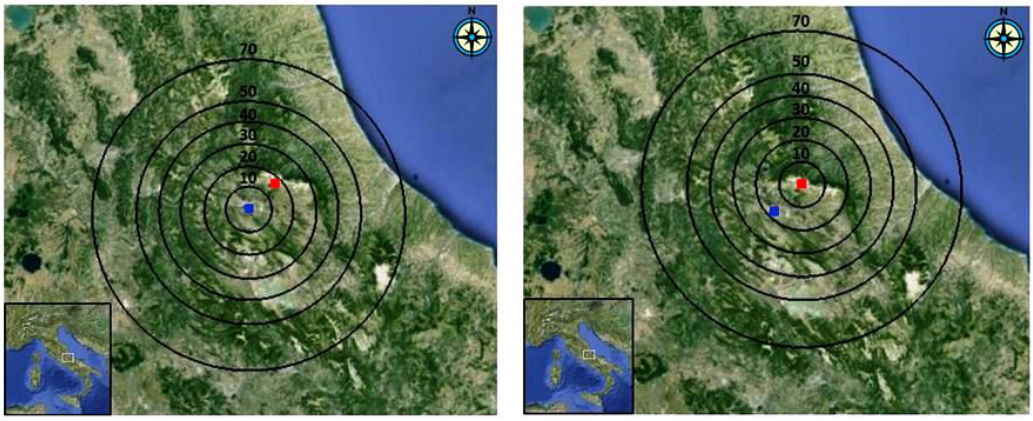

Figure 3.6: Map of central Italy (from Google Earth-CNES/Spot Image-Data SIO, NOAA, U.S. Navy, NGA, GEBCO (2013)). Circular regions centered at L'Aquila main shock (42.340°, 13.380°) and at LNGS-INFN (42.457°, 13.545°), $R = 10, 20, 30, 40, 50, 70$ km. The red dot and the blue dot represent LNGS-INFN and L'Aquila, respectively.

Focusing on the analysis of the entire period, it is possible to observe that most of the seismic activity took place within a distance from 10 to 30 km from LNGS-INFN. Within a radius of 10 km, seismic energy release has been negligible both before and after the L'Aquila earthquake, except for the first few months immediately following the main event. Up to two months before the L'Aquila earthquake, seismic activity was almost absent within 20 km radius from LNGS-INFN and it was very limited also within 30 km. The activity was comparatively higher at distances larger than 40 km. Seismic activity around LNGS-INFN raised significantly a few months before the main event, i.e. starting on November, 2008 within R=30 km, and starting on January, 2009 within R=20 km. Accordingly, seismicity seemed to progressively concentrate around the epicentral area of the impending earthquake, i.e. closer to the LNGS-INFN.

After the earthquake, the region was characterized by a generalized increase of seismic activity, particularly at distances between 10 and 30 km from the LNGS-INFN. Furthermore, seismicity at distances larger than 50 km seemed not significantly affected by the L'Aquila earthquake: no evident increase has been observed in the number of events for regions with R=50 km and R=70 km prior and after the event.

As a rule, for distance ranges up to 40 km, seismicity kept still higher after the L'Aquila earthquake than before the event.

The analysis centered at the epicentral coordinates of the L'Aquila main shock shows that the region was characterized by an increase of seismic activ-

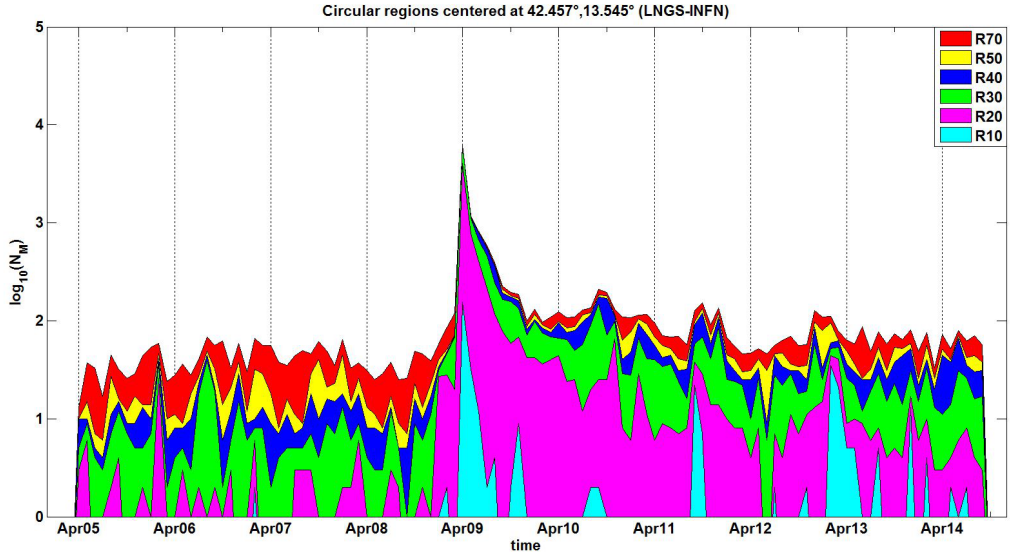

(a) $N_M(t)$

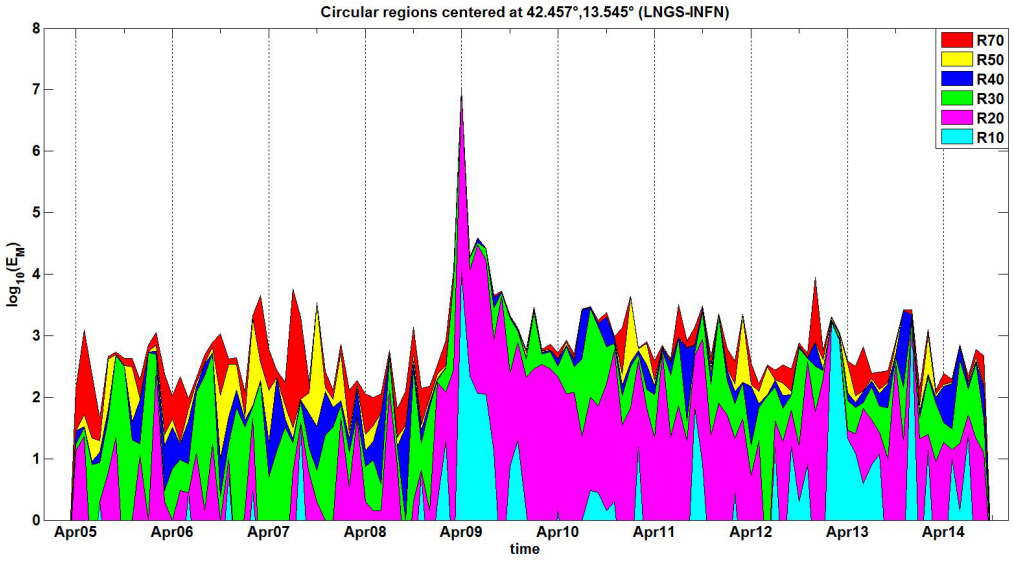

(b) $E_M(t)$

Figure 3.7: Number of events per month $N_M(t)$ and normalized energy release per month $E_M(t)$ are shown for the whole period by non-cumulative area charts, in each distance range, for circular regions centered at LNGS-INFN.

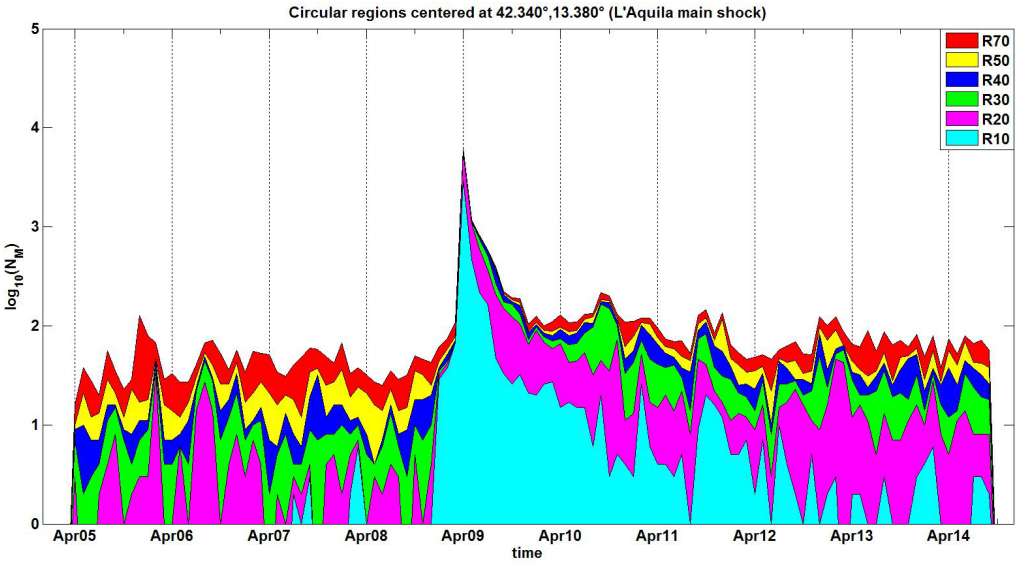

(a) $N_M(t)$

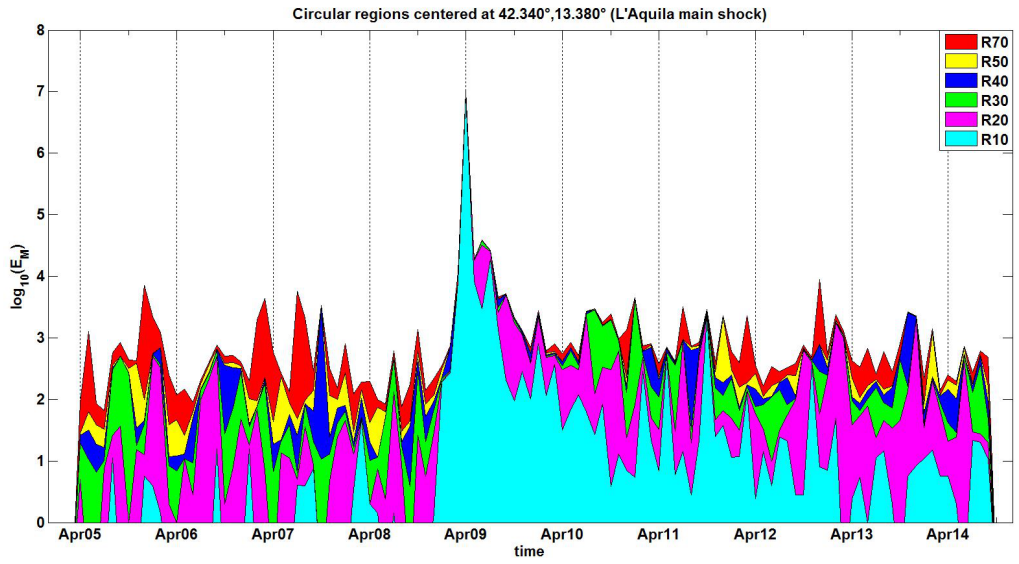

(b) $E_M(t)$

Figure 3.8: Number of events per month $N_M(t)$ and normalized energy release per month $E_M(t)$ are shown for the whole period by non-cumulative area charts, in each distance range, for circular regions centered at the epicentral coordinates of the L'Aquila main shock.

ity at distances between 10 and 40 km after the L'Aquila earthquake. Moving the center of the circular regions from LNGS-INFN to L'Aquila, we observe the activation of the R10 circle: most of the aftershock activity has occurred close to the epicentral area of the main event, but outside of the circular region centered at LNGS-INFN with R=10 km.

The number of aftershock events in unit time interval after the main shock of a significant earthquake ($N(t)$) is described by Omori's law (1894). According to it, the rate of aftershocks decays as the inverse power law in elapsed time after the main shock.

$$N(t) \sim t^{-p} \tag{3.2}$$

where p is the rate of decay of aftershocks.

Omori's law has been modified by Utsu (1961): the rate of decay of an aftershock sequence is described by equating $N(t)$ with the quantity t plus k_1 to the negative power of p, all multiplied by k_2, with k_1 and k_2 constant.

$$N(t) = k_2 \cdot (t + k_1)^{-p} \tag{3.3}$$

The p-value ranges from 0.5 up to 2.5, but normally comes closer to 1 (Dimri, 2005).

We studied the aftershocks of the L'Aquila earthquake, considering seismic events occurred inside the circular region with radius of 30 km (R30), centered at the epicentral coordinates of the L'Aquila main shock, and different time spans after the main shock. We calculated monthly $N(t)$ and we evaluated the goodness of fit with Omori's law for 9, 12 and 15 months, then we compared our results with the same analysis on the complete final part of the catalog under consideration (from the L'Aquila main shock to September 30th, 2014).

Our analysis is represented in Figure 3.9. The estimated parameters are listed in Table 3.1.

For the goodness of fit parameters (GOF), R^2 and adjusted R^2 ($\hat{R}^2$) have been used. They are defined as follows:

- R^2: it can assume values between 0 and 1, with a value closer to 1 indicating that a greater proportion of variance is accounted for by the model. For example, an R^2 value of 0.8234 means that the fit explains 82.34% of the total variation in the data about the average.

$$R^2 = 1 - \frac{\sum_{i=1}^{n}(y_i - \hat{y}_i)^2}{\sum_{i=1}^{n}(y_i - \bar{y})^2} = 1 - \frac{SSE}{SST} \tag{3.4}$$

  where $y_i - \hat{y}_i$ are the predicted values, y_i are the observed values and $\bar{y}$ is the mean of the observed data. We called SSE the numerator of the

previous formula (Explained Sum of Squares) and SST the denominator (Total Sum of Squares).

Increasing the number of fitted coefficients in the model, R^2 will increase although the fit may not improve in a practical sense. To avoid this situation, it is necessary to use the degrees of freedom adjusted R^2 statistic ($\hat{R}^2$).

- $\hat{R}^2$: it is generally the best indicator of the fit quality, because it takes into account the residual degrees of freedom, defined as the number of independent pieces of information, i.e. the number of response values n minus the number of fitted coefficients p minus 1:

$$\nu = n - p - 1$$

.

$$\hat{R}^2 = 1 - \frac{SSE \cdot (n-1)}{SST\Delta\nu} \tag{3.5}$$

$\hat{R}^2$ can assume any value less than or equal to 1, with a value closer to 1 indicating a better fit (MATLAB, 2009).

Table 3.1: Parameters k_1 and k_2 estimated by goodness of fit (with 95% C.L. intervals) with Omori's law for 9, 12, 15 months and for all the months after the L'Aquila earthquake considered in our R30 seismic catalog.

	9 months	12 months	15 months	all months
k_1	0.225	0.223	0.222	0.222
	(0.191, 0.259)	(0.194, 0.252)	(0.196, 0.247)	(0.210, 0.235)
k_2 (10^3)	1.389	1.373	1.367	1.369
	(1.184, 1.593)	(1.198, 1.548)	(1.214, 1.520)	(1.294, 1.445)
GOF:				
R^2	0.998	0.998	0.998	0.998
$\hat{R}^2$	0.998	0.998	0.998	0.998

The residuals, i.e. the difference between the observed value and the theoretical value for each month, are plotted together with the monthly number of events, evaluated after the L'Aquila earthquake (see Figure 3.10). Positive residuals correspond to an increased number of events (as we can see in the case of June-December, 2010, February, 2011, August-November, 2011, November-April, 2013).

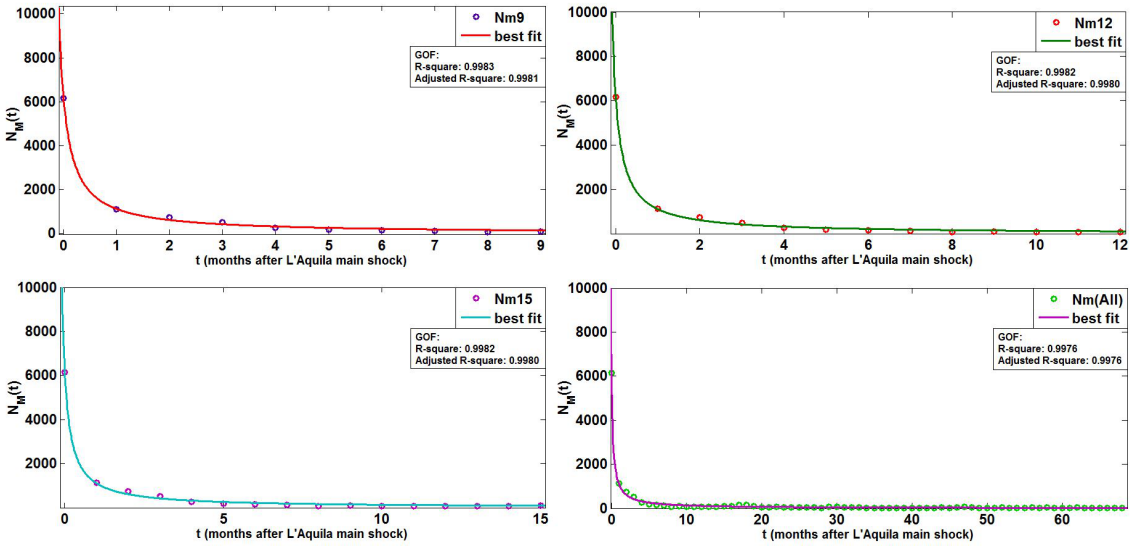

Figure 3.9: Number of monthly aftershocks after L'Aquila earthquake for R30 versus time (9, 12, 15 and 69 months). The estimated parameters are listed in Table 3.1. The four graphs and the corresponding fit curves show that there is no big discrepancy in aftershocks analysis considering different periods of time. Data from the catalog are well explained by Omori's law, even if we consider very long periods of time (69 months).

Although circular extraction centered at LNGS-INFN and L'Aquila can be considered a good meter to outline the basic features of seismicity in the central Italy, a more rigorous analysis is required. For this reason, we decided to analyze the contribution to seismicity of each different circular sector of the R30 circle centered at LNGS-INFN (Section 3.2.2). The R30 circle is the circular region that best approximates the aquifer surface, as it is shown in Figure 3.11. Then, the region occupied by the aquifer and the Seismogenic Sources is taken into account to discriminate seismic activity from seismic "background" (Section 3.2.3).

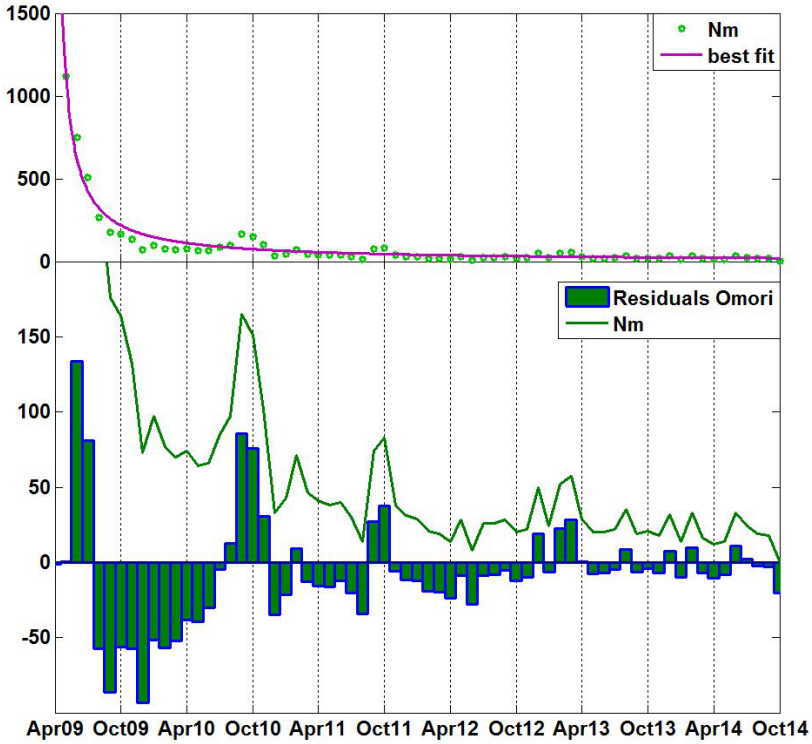

Figure 3.10: Number of monthly aftershocks after the L'Aquila earthquake for R30 versus time, plotted together with the residuals of the analysis. Markedly positive residuals correspond to an increased number of events.

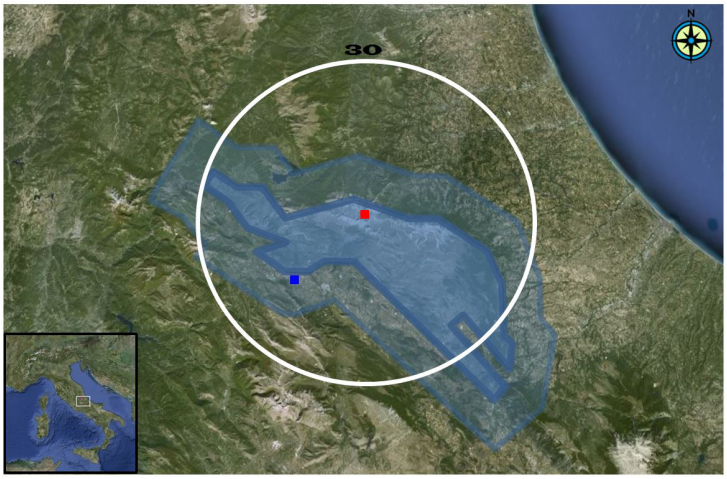

Figure 3.11: Map of central Italy (from Google Earth-CNES/Spot Image-Data SIO, NOAA, U.S. Navy, NGA, GEBCO (2013)). The circular region centered at LNGS-INFN with radius of 30 km (white contour) and the aquifer (light blue area) are shown. The red dot and the blue dot represent LNGS-INFN and L'Aquila, respectively.

3.2.2 Seismic analysis on circular sectors

The second part of the analysis is focused on the spatial variation in time of the seismic signal.

For this purpose, the circular region centered at LNGS-INFN with radius of 30 km has been chosen. This region has been divided in four sectors, named N-W (North-West), S-W (South-West), N-E (North-East), S-E (South-East) because of their position relative to LNGS-INFN, as shown in Figure 3.12.

As the previous analysis, the number of events $N(t)$ and the energy release $E(t)$ within sliding time windows of one month duration have been calculated. In this case, it is possible to observe in Figures 3.13(a) and 3.13(b) that the seismic activity mostly concentrates on the western sectors (i.e. N-W and S-W). Activity in S-E sector is negligible before the main L'Aquila earthquake. It seems mostly related with aftershocks, and it keeps negligible during the remaining time; remarkably, the activity in N-E sector is very limited during most of the time, even immediately after the L'Aquila earthquake, when aftershocks are clearly visible in the other sectors. The only evident feature in seismicity of N-E sector is the period of increased seismicity in December, 2011-January, 2012. The seismic swarm occurred in June, 2010-December, 2010 can be mainly located in the N-W sector.

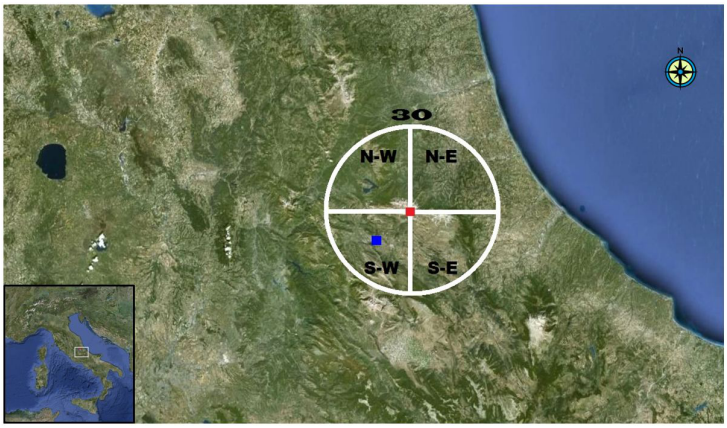

Figure 3.12: Map of central Italy (from Google Earth-CNES/Spot Image-Data SIO, NOAA, U.S. Navy, NGA, GEBCO (2013)). Circular region centered at LNGS-INFN with radius of 30 km, divided in four sectors, named N-W (North-West), S-W (South-West), N-E (North-East), S-E (South-East) because of their position relative to LNGS-INFN. The red dot and the blue dot represent LNGS-INFN and L'Aquila, respectively.

3.2.3 Characterization of seismic activity

For a better definition of the time periods of activity, i.e. to discriminate the seismic background from increased seismicity, the choice of a threshold is required (De Natale et al., 2004). For this purpose, we chose the region identified by the intersection between the boundary of 10 km from the edge of the aquifer and the Composite Seismogenic Sources (i.e. the intersection area between the red polygon and the orange strips in Figure 3.14. For more details, see Sections 3.1.1, 3.1.2); we considered the threshold L_E=E^*_M=356 for the normalized monthly energy release, corresponding to 30% of the considered period of time, as in De Natale et al. (2004). This threshold allows to identify a threshold for the monthly number of events: L_N=N^*_M=35. The periods of activity are then defined as the time spans within which both the normalized energy release E_M and the number of events N_M exceed the threshold of 30%, as shown in Figure 3.15.

Therefore, it is possible to distinguish four periods of increased seismic activity: period A, from February, 2009 to December, 2009, which consists of the preparation phase, the main phase and the several aftershocks of the L'Aquila earthquake; from July to December, 2010, another period is identified (period B), minor than the previous one for both the normalized energy release and the number of events; Periods C and D have been identified from August to November, 2011 and from January to April, 2013. Periods B, C and D are very similar to the time spans identified in Section 3.2.1, during

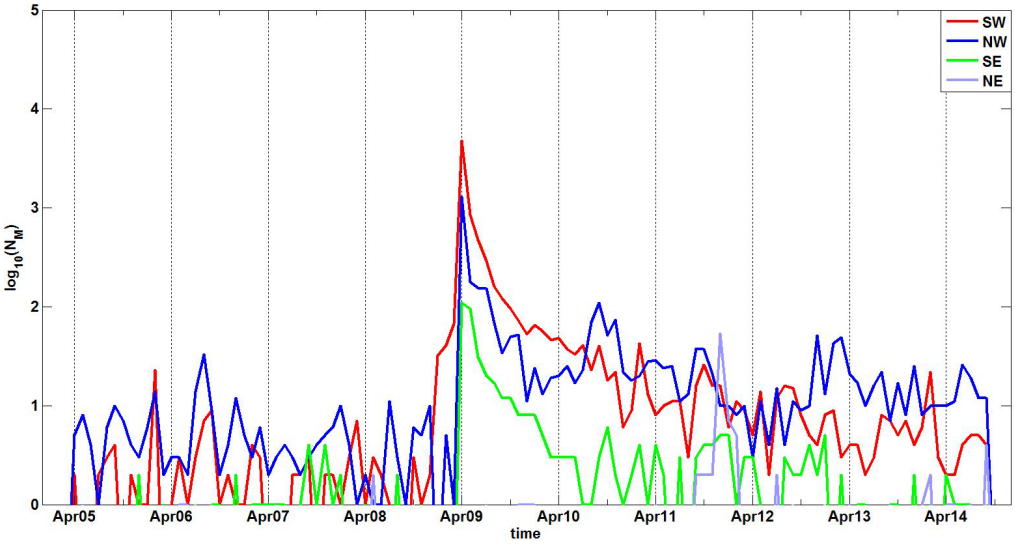

(a) $N_M(t)$

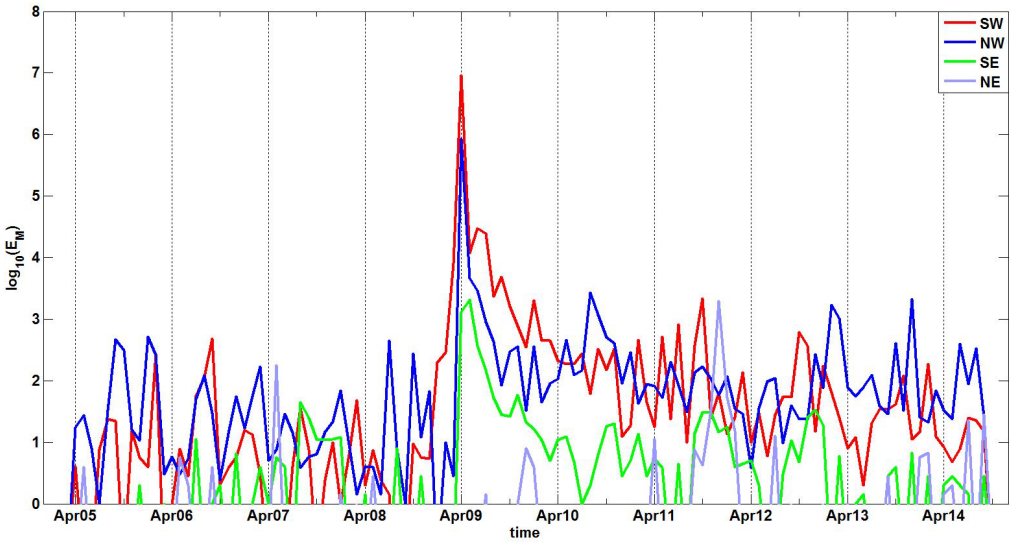

(b) $E_M(t)$

Figure 3.13: Number of events per month $N_M(t)$ and normalized energy release per month $E_M(t)$ calculated for four different sectors of the circular region centered at LNGS-INFN with radius R=30 km. It is possible to notice that seismic activity mostly concentrates on the western sectors, S-W and N-W. Activity in S-E sector is negligible before the main L'Aquila earthquake and it seems mostly related with aftershocks. Activity in N-E sector is very limited during most of the time, even immediately after the L'Aquila earthquake. The only evident feature in seismicity of N-E sector is the period of increased seismicity in December, 2011-January, 2012.

Figure 3.14: Map of central Italy (from Google Earth-CNES/Spot Image-Data SIO, NOAA, U.S. Navy, NGA, GEBCO (2013)). Composite Seismogenic Sources (orange strips), boundary of the aquifer (25 vertices black polygon) and boundary of 10 km from the edge of the aquifer (10 vertices red polygon). The red dot represents LNGS-INFN. The area under consideration is the intersection between the red polygon and the orange strips.

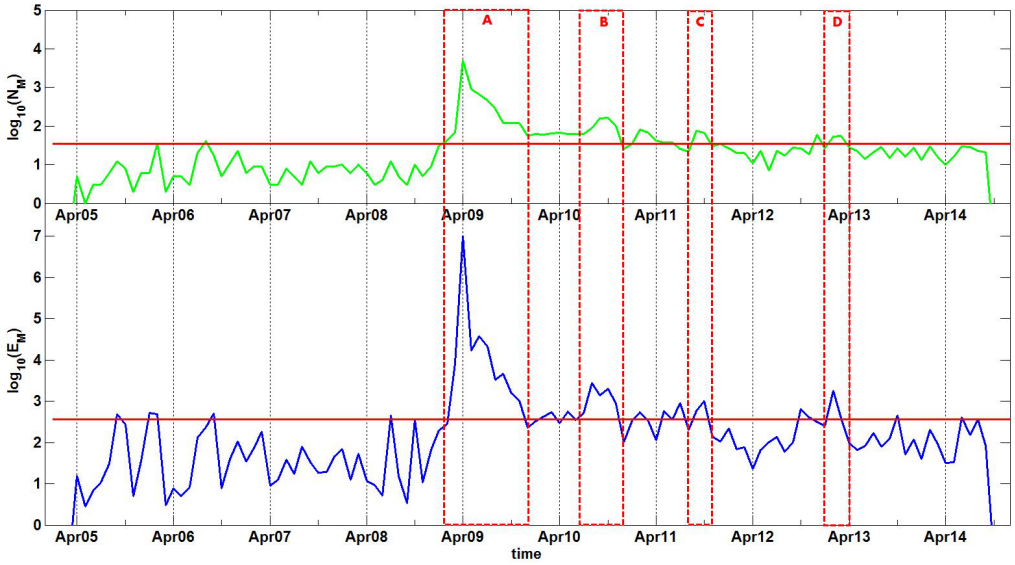

Figure 3.15: Time periods of activity defined by the thresholds $L_E = E_M^* = 356$ and $L_N = N_M^* = 35$, corresponding to 30% of the considered period of time. The periods of activity are defined as the time intervals within which both the normalized energy release E_M and the number of events N_M exceed the threshold of 30%. The red dashed boxes represent Period A (February-December, 2009), Period B (July-December, 2010), Period C (August-November, 2011) and D (January-April, 2013).

the analysis of the L'Aquila aftershocks (see Figure 3.10).

In Figures 3.17(a), 3.17(b), 3.17(c) and 3.17(d) it is possible to identify the geographic coordinates and the depth of the seismic swarms in periods A, B, C and D, to show the scale of magnitudes and number of events, for a better comparison between a large seismic event and lighter seismic swarms. Swarm A affected the area under investigation from February to December, 2009. It consisted of almost 2800 records with M_l ranging from 2.0 up to 5.9 (magnitude of the main shock, occurred at 01:33 UT on April 6th, 2009). The magnitude scale in Figures 3.17(b), 3.17(c) and 3.17(d) reaches values of 3.5-3.6.

Observing swarms B, C and D respect to both LNGS-INFN and to the aquifer (Figures 3.17(f), 3.17(g) and 3.17(h)) and comparing them with Figure 3.14, some additional remarks can be done: swarm B is clustered in the northwestern area of LNGS-INFN (in a normal fault area), while swarms B and C are gathered north with respect to LNGS-INFN (in a thrust fault region, very close to the Laboratories). As it was already deducible from Figure 3.2.3, the order of magnitude of the number of events of B, C and D is very different from A.

Figure 3.16: Swarms A, B, C and D are represented in the three spatial coordinates (Longitude, Latitude and Depth), to better visualize the 3D position of each single event, as well as to show the different entities of the swarms. The size of the markers shows the magnitude of the events of each seismic swarm (M_l ranges from 2.0 up to 5.9 for swarm A and from 2.0 up to 3.6 for swarms B, C and D.)

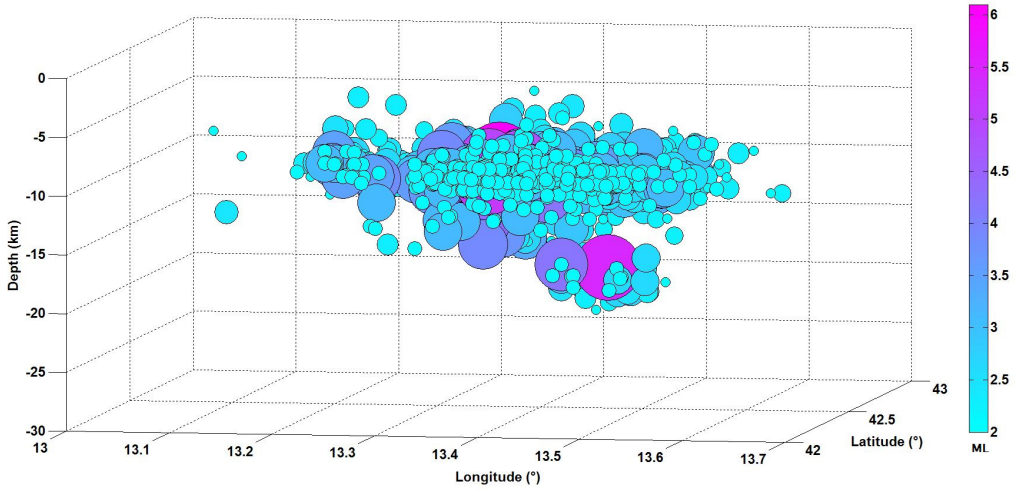

(a) Swarm A (L'Aquila earthquake, February-December, 2009)

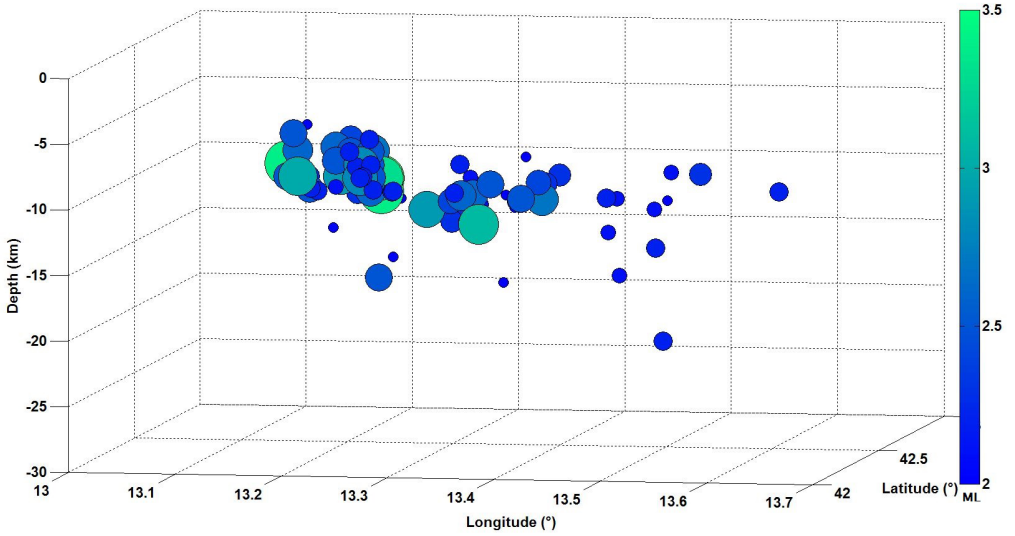

(b) Swarm B (July-December, 2010)

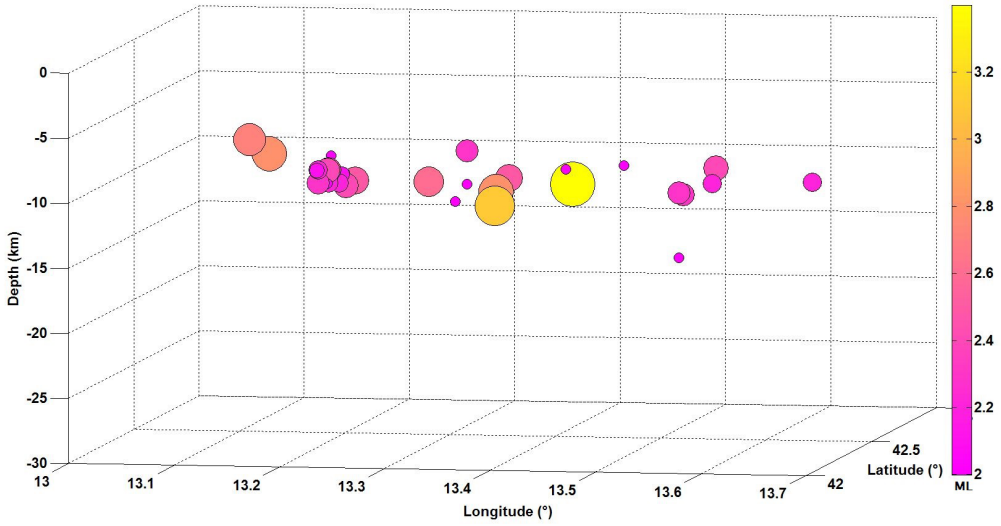

(c) Swarm C (August-November, 2011)

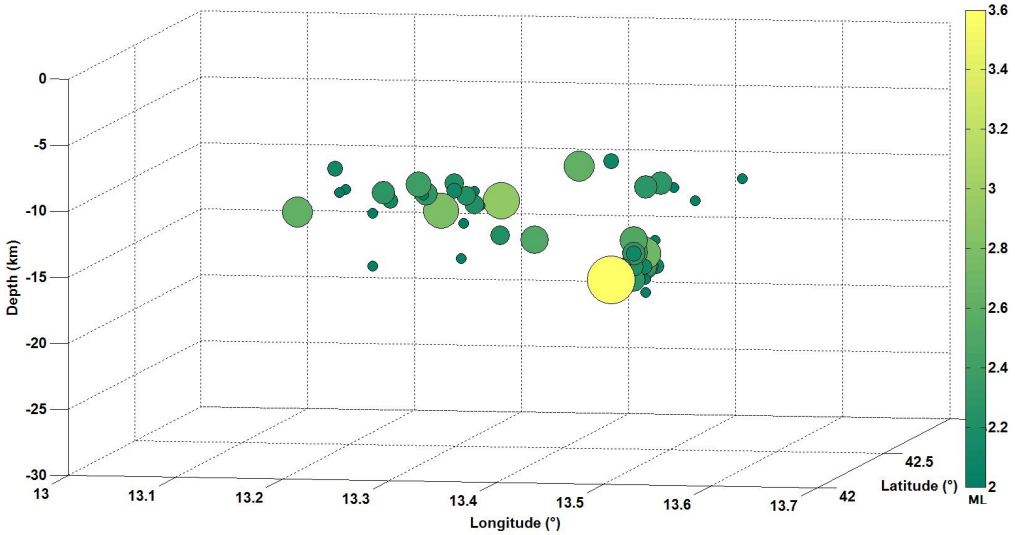

(d) Swarm D (January-April, 2013)

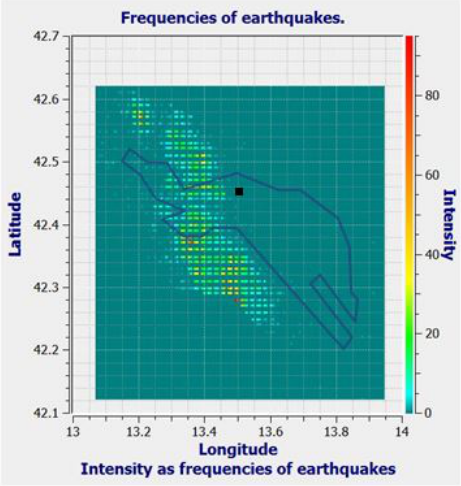

(e) Swarm A (L'Aquila earthquake, February-December, 2009)

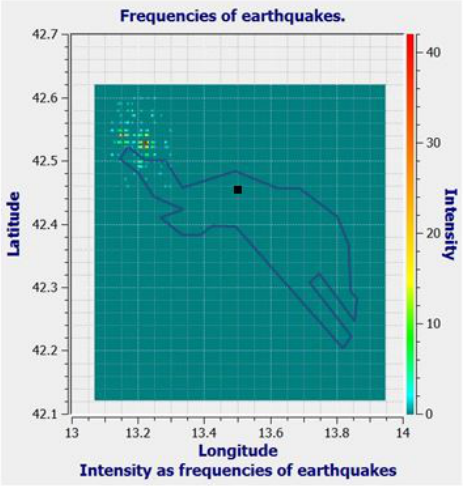

(f) Cluster B

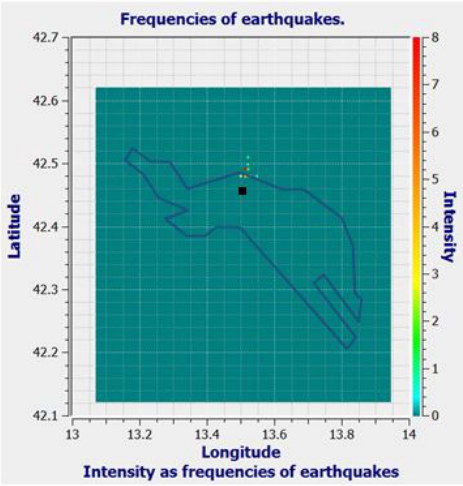

(g) Cluster C

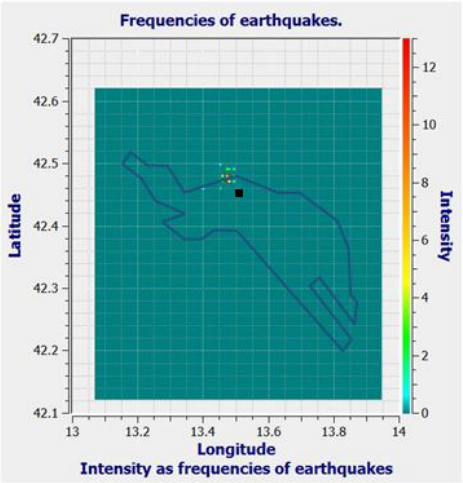

(h) Cluster D

Figure 3.17: Spatial distribution of the events with $M \geq M_{min} = 1.5$. Intensity of seismic activity, expressed as number of earthquakes, is represented by a colored scale from blue to red. The black dot represents LNGS-INFN. The aquifer is also shown.

Chapter 4

Uranium time series analysis

With stochastic process we indicate an actual, e.g. physical, process in the real world, that has some random (stochastic) elements involved in its structure. The observed value at time t, x_t, is as an observation of an underlying random variable, X_t. The observed time series is called a (finite) realization of the stochastic process and the population of all possible realizations is called the *ensemble*.

The analysis of time series is different from other statistical problems in which the observed time series is usually the one and only realization that will ever be observed. In other words, x_t is usually the only observation we will ever get on X_t. Despite this, it is important to estimate the properties of the underlying stochastic process. Estimation theory for stochastic processes is partially concerned with seeing whether and when a single realization is enough to estimate the properties of the underlying model.

The observation of a continuous physical process by discrete measurements, a time series, is then a collection of observations of well-defined data items obtained through repeated measurements over time.

Processes are stationary if their properties do not change through time, e.g. it is homogeneous in time. More formally, a stochastic process is said to be second-order stationary if its first and second moments are finite and do not change in time. The first moment is the mean $E[X_t]$, while the general second moment is the covariance between X_t and X_{t+k} for different values of t and k. This type of covariance is called autocovariance. The variance is the particular case when the lag k is zero. Thus, a process is second-order stationary if, for all t, $E[X_t]$ is a finite constant, say μ, if $Var[X_t]$ is a finite constant, say σ^2, and, more generally, if the autocovariance function depends only on the lag k:

$$Cov[X_t, X_{t+k}] = E[(X_t - \mu)(X_{t+k} - \mu)] = \gamma_k \tag{4.1}$$

The autocovariance function is sometimes standardized to autocorrelation function:

$$\rho_k = \frac{\gamma_k}{\gamma_0} \tag{4.2}$$

The autocorrelation function is an even function of lag, since $\rho_k = \rho_{-k}$, and has the usual property of correlation that $|\rho_k| \leq 1$.

A stochastic process is said to be Gaussian (or normal) if the joint distribution of any set of X_t's is multivariate normal. Such a process is completely characterized by its first and second moments. One way for describing a stationary stochastic process is by means of its spectral density function, or spectrum, which is the discrete Fourier transform of γ_k:

$$f(\omega) = \frac{1}{\pi}(\gamma_0 + 2\sum_{k=1}^{\infty}\gamma_k cos(\omega k)) \tag{4.3}$$

for $0 \leq \omega \leq \pi$.

The function describes how the overall variance of the process is distributed over different frequencies from zero to the Nyquist frequency. The latter frequency is the highest frequency which we can get information about from data recorded at unit intervals of time. It corresponds to a sine wave which completes one cycle in two time intervals.

The two functions γ_k and $f(\omega)$ are equivalent and complementary. An analysis primarily based on estimates of the autocorrelation (or autocovariance) function is called an analysis in the time domain, while an analysis primarily based on the spectrum is called a spectral analysis (an analysis in the frequency domain). Sometimes it is not possible to disregard from one of this two functions.

A real time series is both discrete and finite. For this reason, the autocorrelation function can only be estimated, as well as the spectral density function.

One of the most useful tool in time series analysis is the correlogram. Let us denote the observed time series by $x_1, x_2, ..., x_N$. The sample autocovariance coefficient at the lag k is:

$$c_k = \frac{1}{N}\sum_{t=1}^{N-k}(x_t - \bar{x})(x_{t+k} - \bar{x}) \tag{4.4}$$

for $k = 0, 1, 2, ..., N$, and the sample autocorrelation coefficient at the lag k is

$$r_k = \frac{c_k}{c_0} \tag{4.5}$$

The graph r_k against k is called sample autocorrelation function or correlogram. It is usually plotted for the original series and at the end of the analysis of the residual data, as necessary to make the series look stationary and approximately normally distributed. For data from a stationary process, it can be shown that the correlogram generally provides an estimate of the theoretical autocorrelation function defined in 4.2.

Interpreting a correlogram is one of the hardest tasks in time-series analysis, especially when N is small, so that the sample autocorrelations have relatively large variance. For a stationary series, the pattern of the correlogram may suggest a stationary model with an autocovariance function of similar shape.

It is possible to outline some general cases:

- Random Series
  If a time series is completely random, for large N it's $r_k \sim 0$ for each k. This implies the complete randomness and the total independence of the samples. For a random series, r_k has a quasi-normal shape with zero mean. All values of r_k are therefore inside the band $\pm z_{1-\alpha/2}/\sqrt{N}$.

- Short-term Correlation
  In this case, the samples are not completely independent for any lag k. For example, there can be a big r_1 value, while $r_k \to 0$ for big k. This happens when an observation above (under) the mean is followed by many observations above (under) the mean.

- Non-Stationary Series
  If a time series is characterized by a trend, then r_k could show the same trend behavior when k increases. If the time series is characterized by a periodicity, then the correlogram could show the same periodicity. The interpretation of the correlogram is very helpful, because it permits to identify the non-stationarity of the series under consideration. However, if the series is affected by a trend or a periodicity, it needs to be processed. The procedure is described below.

A time series can be generally decomposed into three components. The trend is the long term direction of the series, without calendar related or irregular effects. The seasonal is the systematic, calendar related effect. This component consists of effects that are reasonably stable with respecting to timing, direction and magnitude. Examples of seasonal are natural conditions (snow melting, rain precipitations). Seasonality in a time series can be identified by regularly spaced peaks in the spectrum, which have approximately the same direction and magnitude every year, relative to the trend.

The irregular component (also known as residual component) is what remains after the seasonal and the trend components of a time series have been estimated, characterized and removed. This short term fluctuations are neither systematic, nor predictable. If the series is highly irregular, these fluctuations could dominate movements and could mask the trend and the seasonality.

The identification of the outliers of a time series is not an easy matter. Assumptions about outliers from the initial series could be a hazard. In fact, outliers are anomalous observations respect to the mechanism of generation of the series, not only "high values". For this reason, they can be hidden inside the time series. For example, the overlapping of different periodic components could amplify the resulting signal, showing an ostensible anomaly, which is actually part of a mechanism of generation of the series. Removing the periodicities of the series, one can deal with the residual component of the series, linked to the *real* basic process.

The aim of our work is therefore the implementation of an algorithm able to conduce our starting series to a residual series (white noise (WN) series), outlining, characterizing and removing the periodic components, which are not connected to the physical mechanism we are studying (with the assumption that this mechanism is NOT periodic).

The method implies the use of frequency-domain analysis. These methods are better than the time-domain methods in the removal of periodic components (Fuenzalida and Rosenbluth, 1989).

Spectral analysis is used for the identification of the characteristic periodicity (which appears in the form of peaks in the frequency spectrum), while stop-band filters are used for removing it.

After the filtering procedure, the residuals are analyzed in order to outline any possible anomalous value.

4.1 Spectral valuation of time series

The discrete Fourier transform of a real sequence of data $x(n)$, $0 \leq n \leq N-1$ is defined as in Brigham (1974):

$$X(k) = \sum_{n=0}^{N-1} x(n) e^{-j2\pi kn/N} \tag{4.6}$$

with $k \in \mathbb{Z}$ and $k/N = f$.

Power spectrum estimation is called periodogram (Welch, 1967):

$$P_N(f) = \frac{1}{N} |X(f)|^2 \tag{4.7}$$

Unfortunately, this is not an adequate estimation of the periodogram, since the variance of $P_N(f)$ does not tend to zero when N tends to infinity (Reina, 2006).

In Bartlett (1948) and Bartlett (1950), the author proposed to extend the evaluation on many independent valuations. Data sequence is therefore divided in K independent segments, each composed of M elements ($N = KM$).

From the sequences

$$x^{(i)}(n) = x(n + iM - M) \tag{4.8}$$

with $0 \leq n \leq M - 1$ and $1 \leq i \leq K$, it is possible to calculate the K periodograms.

$$P_M^{(i)}(f) = \frac{1}{M} \left| \sum_{n=0}^{M-1} x^{(i)}(n) e^{-j2\pi \frac{Kn}{M}} \right|^2 \tag{4.9}$$

with $1 \leq i \leq K$.

Spectral estimation is defined as

$$B(f) = \frac{1}{K} \sum_{i=1}^{K} P_M^i(f) \tag{4.10}$$

Unfortunately, also Bartlett estimation is not adequate, this time to the detriment of the spectral resolution.

As we stated before, it is essential to take into consideration that a time series is a finite realization (N) of a real process in spectral analysis, that is a limited ensemble of collected data. It corresponds to multiply, in the time domain t, the input signal (theoretically, $-\infty < t < +\infty$) by a rectangular window of the dimension of Δt occupied by the samples under consideration. Multiplication in time domain means convolution product in frequency domain; furthermore, the spectrum of a rectangular window is a *sinc* function. What follows is that the spectral estimation of the single frequencies is not accurate, because each component of the spectrum contains losses (leakage effect) descending from many consecutive components.

This inconvenience could be solved by using a lighter cut off of the Fourier series, changing the shape of the window. This choice constitutes a compromise between resolution in frequency and uncertainty on the amplitude of the signal. Bartlett window represents a better choice. The inconvenience, in this case, is that the small variance is paid by a worse resolution of the spectrum.

In Welch (1967) the author, with the aim of improving the spectral resolution without renouncing windowing, modified Bartlett method. In Welch method, data are divided in $K = N/M$ sequences, each of length M samples (as in Bartlett method), but a particular window $w(n)$ is applied before the evaluation of the periodogram, directly on the M sequences of data.

The analysis is therefore, step by step:

1. Definition of K modified periodograms

$$P_M^{(i)}(\omega) = \frac{1}{MU} \left| \left[\sum_{n=0}^{M-1} x^i(n) w(n) e^{-j\omega n} \right] \right|^2 \tag{4.11}$$

with $i = 1, 2, ..., K$
and

$$U = \frac{1}{M} \sum_{n=0}^{M-1} w^2(n)$$

2. Spectrum estimation

$$\Phi(\omega) = B^w(\omega) = \frac{1}{K} \sum_{i=1}^{K} P_M^{(i)}(\omega) \tag{4.12}$$

U is necessary for being $B^w(\omega)$ asymptotically correct.

It is also possible to choose a percentage of windows overlapping (P) in order to avoid the loss of some samples.

The reasons for this modifications to the Bartlett method are simple to explain. The overlapping of the periodograms to be averaged decreases the variance of the estimated spectrum. The appropriate window applied before the evaluation of the periodogram allows a better control on the bias/resolution properties of the estimated spectrum and it also permits to give less weight to the data samples at the ends of each subsample (decreasing the correlation between the sequences, even if they are overlapped) (Stoica and Moses, 2005).

4.2 Synthetic time series simulations

A method for the analysis of time series is designed and optimized in order to distinguish the characteristic frequencies of the time series as well as to find possible outliers (Plastino et al. (2010a) and references therein).

It is important to underline that the main aim of this algorithm is to discover anomalous values in an environmental time series (content of uranium in groundwater, in our case), while it is not important to find the 'real value' of the basic physical process observable.

The first step of our analysis is based on the application of the designed method to two different synthetic series: the first one is the composition of a Deterministic signal, a Stochastic signal and a linear trend; the second one has, compared to the fist one, the addition of five outliers.

In this way it is possible to optimize the parameters of the method as well as to check if the method works well in the individuation of the characteristic frequencies and of possible outliers of a time series.

Various tests on synthetic time series have brought almost to the same results. Two significant cases are shown below.

4.2.1 Synthetic time series without outliers (NOS)

We define our synthetic series as the sum of different contributions:

- Deterministic signal D: sum of sine and cosine

$$\begin{aligned} D = A_1 \sin(2\pi t \nu_1) + A_2 \sin(2\pi t \nu_2) + A_3 \cos(2\pi t \nu_3) + \\ + A_4 \sin(2\pi t \nu_4) + A_5 \cos(2\pi t \nu_5) \end{aligned} \tag{4.13}$$

  with (in days^{-1}): ν_1=0.001, ν_2=0.01, ν_3=0.02, ν_4=0.04, ν_5=0.06 and (in a.u.): A_1=3, A_2=4, A_3=5, A_4=4.5, A_5=2.5.

- Stochastic signal S: white Gaussian noise

- Linear trend T

$$T = 0.0008t + 0.7$$

All data processing is performed off-line using a commercial software package (MATLAB 7.9, The MathWorks Inc., Natick, MA, 2009).

Our synthetic time series DST is now ready for analysis and it is shown in Figure 4.1. The first step is to detrend the starting series, by means of the *detrend()* function already available in MATLAB (Figure 4.2).

Power spectrum is evaluated by means of Welch method (*spectrum.welch()*), using Hann window. Hann window *hann()* returns an L-point symmetric Hann window in the column vector w. L must be a positive integer. The coefficients of a Hann window are computed from the equation 4.14.

$$w_k = 0.5 \left(1 - cos\left(2\pi \frac{k}{M}\right)\right) \tag{4.14}$$

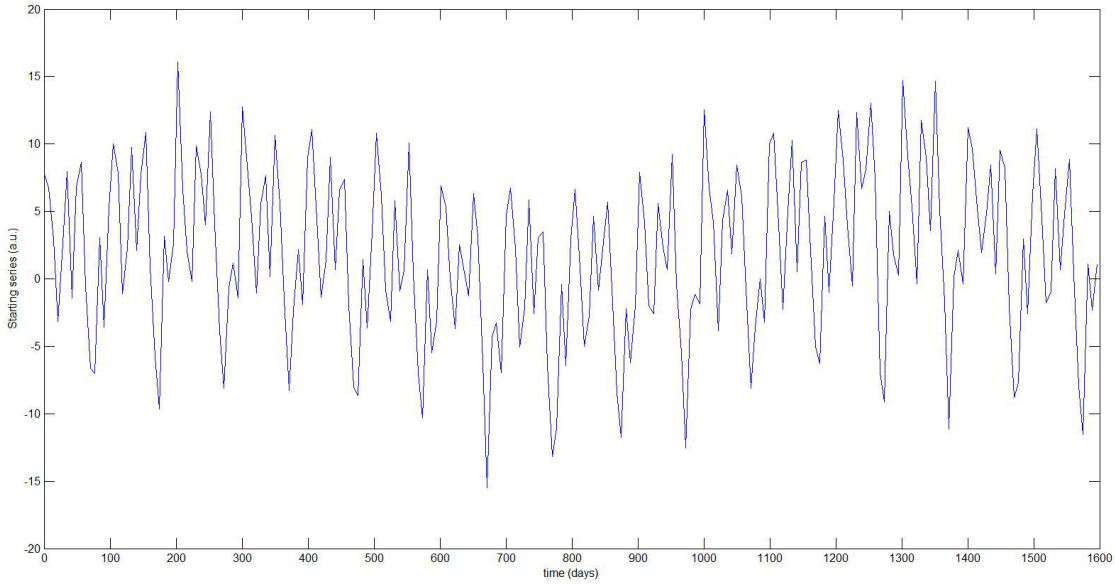

Figure 4.1: Synthetic series (NOS), composed by a Deterministic, Stochastic and Linear trend signal.

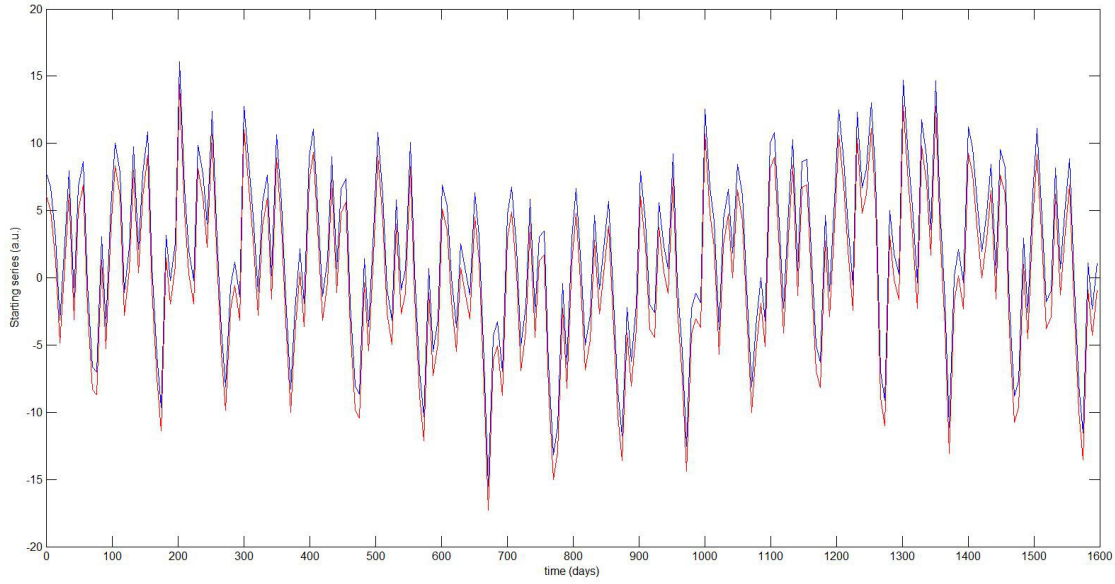

Figure 4.2: *detrend* function applied to the starting series (red) respect to the starting NOS (blue).

with $0 \leq k \leq M$ and $L = M + 1$.

Our analysis is optimized by the choice of M=150 and P=90% for windowing and overlapping, respectively.

An important observation is due to the choice of M. Large values of M imply great number of peaks in the estimated power spectrum, most representing spurious peaks. However, too small M could hide significant peaks (Plastino et al., 2010a).

Chatfield (2013) references Jenkins and Watts (1968) for the general relationship between the truncation point M and the variance of the spectral estimation: the spectrum valuation asymptotically follows a χ^2_ν distribution with

$$\nu = \frac{2N}{\sum_{k=-M}^{M} w_k^2}$$

degrees of freedom. It follows that a 100(1-α)% confidence interval is given by

$$\left[\frac{\nu\Phi(\omega)}{\chi^2_{\nu,\alpha/2}}, \frac{\nu\Phi(\omega)}{\chi^2_{\nu,1-\alpha/2}} \right] \tag{4.15}$$

The spectrum valuation (Figure 4.3) is plotted with spectrum upper and lower limits considering confidence intervals at 95%, together also with the null spectrum (estimated by the mean of the spectra of 1000 simulations of white noise time series).

We considered the peaks of the spectrum as significant only if the corresponding maximum of the lower limit function was greater than the value of the null spectrum at the same frequency. In that case, the two minima of the spectrum within which the peak is located, pinpoint a frequency band to be considered as significant. The spectrum within that band is fitted with a Gaussian curve:

$$y = a \exp\left[(x - b)/c\right]^2$$

Frequency intervals are estimated considering $\Delta\nu$ that corresponds to the 10%, 20%, 30%, 40%, 50%, 60%, 70% and 80% of the parameter a, depending on the user's choice. 10% and 80% correspond to the largest and the smallest $\Delta\nu$, respectively. We chose the 10% and we obtained the corresponding $\Delta\nu$ intervals (Table 4.1). By means of the function *idealfilter*, a ideal notch filter is applied to the data: $\Delta\nu$ intervals are removed from the starting series.

The residual series is subjected to a Kolmogorov-Smirnov test (KStest), which returns a test decision for the null hypothesis that the data in the input vector comes from a normal or a t-location-scale distribution, against the alternative that it does not come from such a distribution. The result h is 1 if the test rejects the null hypothesis at the 5% significance level, or 0

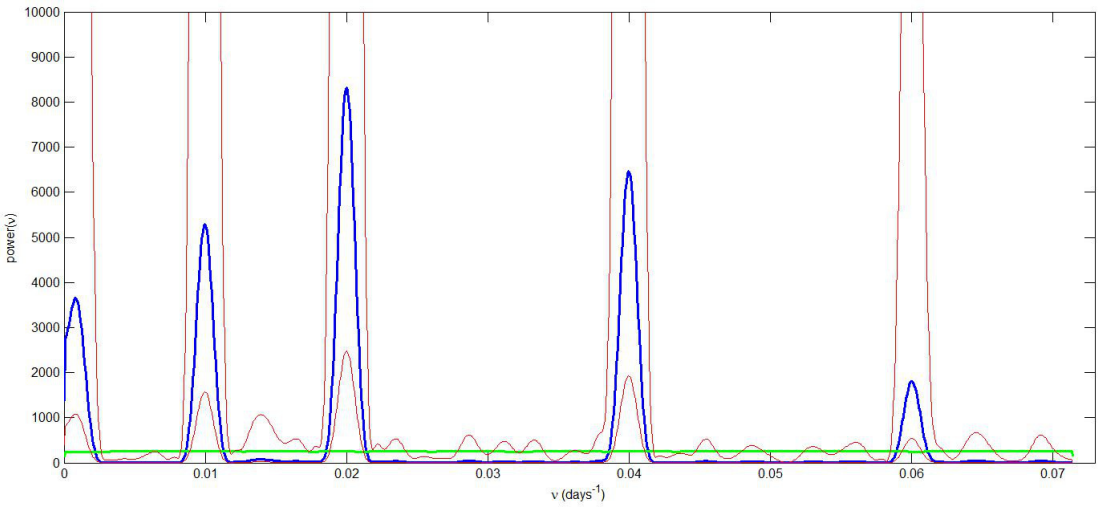

Figure 4.3: Power spectrum of NOS, evaluated by Welch method, using Hann window with M=150 and P=90%, together with spectrum upper and lower limits considering confidence intervals at 95% (red) and the null spectrum (green).

Table 4.1: $\Delta\nu$ $(days^{-1})$ intervals corresponding to 10% a (NOS)

$\nu_{min}(days^{-1})$	$\nu_{max}(days^{-1})$
0	0.0021
0.0088	0.0111
0.0188	0.0212
0.0388	0.0412
0.0590	0.0611

otherwise. The test statistic is

$$D = max\left(|F(x) - G(x)|\right) \tag{4.16}$$

where $F(x)$ and $G(x)$ are the empirical and the theoretical cumulative distribution functions, respectively. The D value is compared with the cutoff value D^*.

- Normal Distribution

$$y_N = \frac{1}{\sigma\sqrt{2\pi}} \exp\left[-\frac{(x-\mu)^2}{2\sigma^2}\right]$$

with mean μ and standard deviation σ

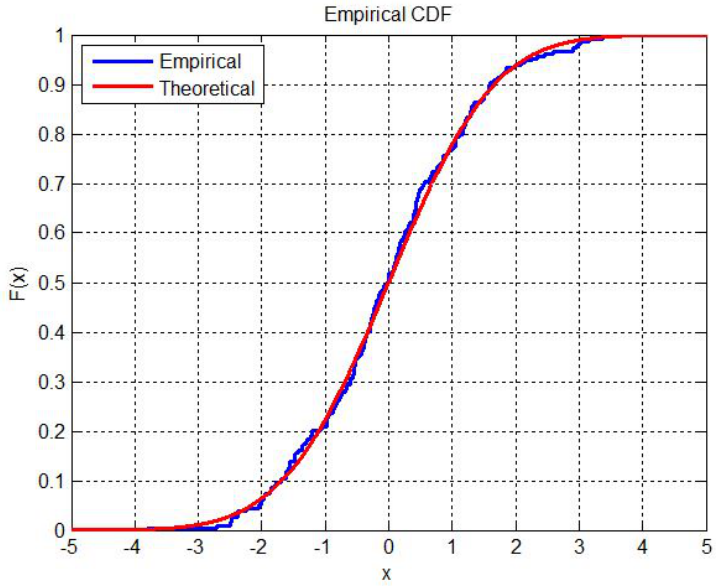

Figure 4.4: Cumulative distribution function of empirical (NOS) and theoretical (Gaussian) distributions.

- t-location-scale Distribution

$$y_t = \frac{\Gamma(\frac{\nu+1}{2})}{\sigma\sqrt{\pi\nu}\Gamma(\frac{\nu}{2})}\left[\frac{\nu + \left(\frac{x-\mu}{\sigma}\right)^2}{\nu}\right]^{-\left(\frac{\nu+1}{2}\right)}$$

  with location parameter μ, scale parameter σ and shape parameter $\nu>0$. If the input vector x has a t-location-scale distribution with parameters μ, σ and ν, then $\frac{x-\mu}{\sigma}$ has a Student's t distribution with ν degrees of freedom.

The empirical and theoretical cumulative distribution function (CDF) and the probability density function (PDF) are shown in Figure 4.4 and 4.5. In this case, the test did not reject the null hypothesis.

The residual series, normalized with zero mean and σ=1, is represented by a bar graph (Figure 4.6). Outliers are defined as values of the residual series with a modulus greater than three times the estimated standard deviation. It is important to notice the no appearance of (spurious) outliers in the residual series.

The filtered $\Delta\nu$ intervals are saved together with the percentage of the removed spectrum respect to the total spectrum (Table 4.2). It is possible to

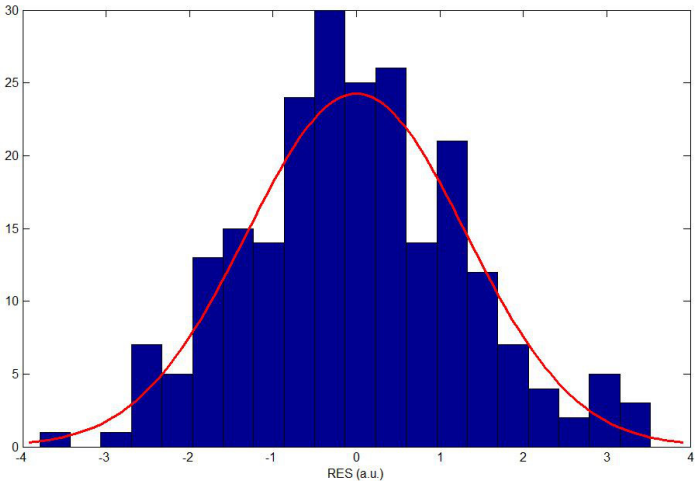

Figure 4.5: Probability density function of empirical (NOS) and theoretical (Gaussian) distributions.

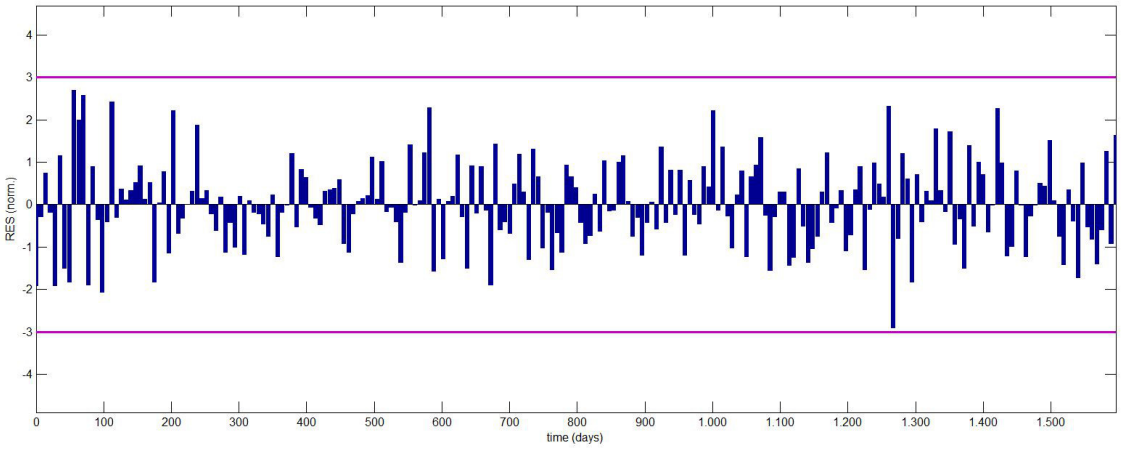

Figure 4.6: Residuals of the synthetic time series (NOS).

Table 4.2: $\Delta\nu$ ($days^{-1}$) intervals corresponding to 10% a (NOS) and the percentage of the removed spectrum

$\nu_{min}(days^{-1})$	$\nu_{max}(days^{-1})$	%
0	0.0021	14
0.0088	0.0111	20
0.0188	0.0212	31
0.0388	0.0412	24
0.0590	0.0611	7

notice that $\Delta\nu$ intervals correspond exactly to the Deterministic Signal we put inside the initial synthetic series.

An Autocorrelation test (or Ljung-Box Q-Test, LBtest) is now applied on the residual series. This test assesses the null hypothesis that a series of residuals exhibits no autocorrelation for a fixed number of lags L, against the alternative that some autocorrelation coefficient $r(k)$, k=1,...,L, is non-zero.

The test statistic is:

$$Q = N(N+2)\sum_{k=1}^{L}\frac{r(k)^2}{N-k} \tag{4.17}$$

where N is the sample size, L is the number of autocorrelation lags, $r(k)$ is the sample autocorrelation at lag k.

Under the null hypothesis, the asymptotic distribution of Q is chi-square with L degrees of freedom. For significance level α, the critical region for rejection of the hypothesis of randomness is:

$$Q > \chi^2_{1-\alpha,L} \tag{4.18}$$

where $\chi^2_{1-\alpha,L}$ is the α-quantile of the chi-square distribution with L degrees of freedom (Q^*).

The correlogram ($r(k)$ versus the lag k) is another way of verifying that all the characteristic frequencies have been removed from the starting series, e.g. the series is now a white-Gaussian-noise series. In the same graph one can draw upper and lower bounds for autocorrelation with significance level α. If the autocorrelation is higher (lower) than this upper (lower) bound, then the null hypothesis that there is no autocorrelation at a given lag is rejected at a significance level of α. This test is an approximate one and assumes that the time-series is Gaussian.

For the confidence band we used the formula: $\pm\frac{z_{1-\alpha/2}}{\sqrt{N}}$, where N is the sample size and z is the quantile function of the normal distribution.

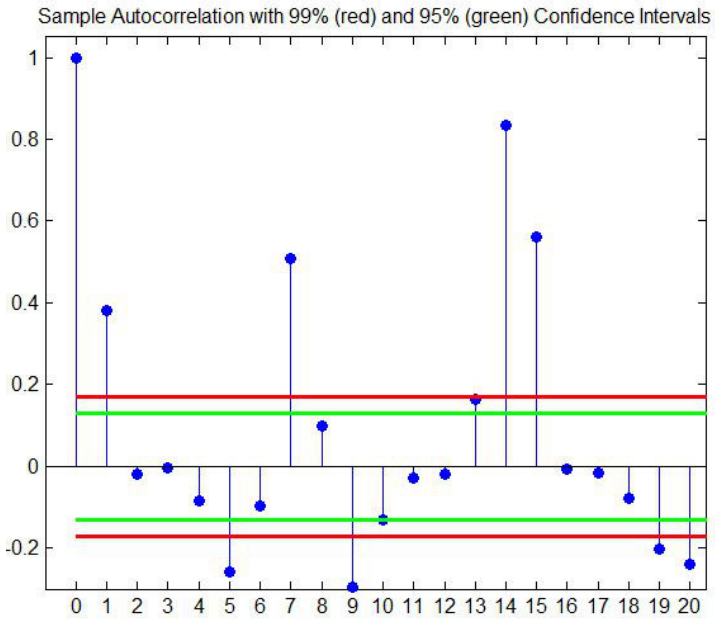

Figure 4.7: Correlogram of the starting series (NOS).

Autocorrelation function applied to our starting series shows a strong autocorrelation (Figure 4.7).

The correlogram of the residual series is shown in Figure 4.8. It is possible to compare the initial and the final correlograms by the plot in Figure 4.9. The difference between the autocorrelation coefficient and the value of the 95% confidence interval for each lag k allows to make considerations about the success of the procedure, by the comparison of the values before and after the analysis.

The procedure of our analysis of time series can be outlined in a block diagram, shown in Figure 4.10.

4.2.2 Synthetic time series with outliers (OS)

The same procedure has been applied to the same synthetic series with the addition of five outliers.

The outliers are placed before the analysis in random positions inside the synthetic time series, in order to avoid the presence of a "false" frequency peaks in the frequency spectrum. For convenience, the components of the synthetic time series are written again below.

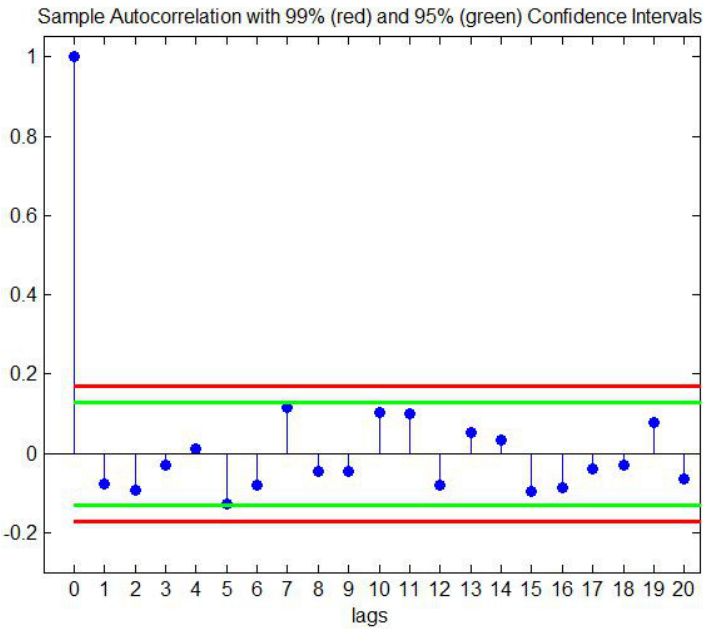

Figure 4.8: Correlogram of the residual series (NOS).

- Deterministic signal D: sum of sine and cosine

$$D = A_1 \sin(2\pi t\nu_1) + A_2 \sin(2\pi t\nu_2) + A_3 \cos(2\pi t\nu_3) + \\ + A_4 \sin(2\pi t\nu_4) + A_5 \cos(2\pi t\nu_5) \tag{4.19}$$

  with (in days^{-1}): ν_1=0.001, ν_2=0.01, ν_3=0.02, ν_4=0.04, ν_5=0.06 and (in a.u.): A_1=3, A_2=4, A_3=5, A_4=4.5, A_5=2.5.

- Stochastic signal S: white Gaussian noise

- Linear trend T

$$T = 0.0008t + 0.7$$

In addition, five outliers have been added to the series, at these random positions: t=84, 231, 364, 791 and 1260 days, three positive and two negative, as shown in Figure 4.11. As in the case with no outliers, the *detrend()* function is applied to the synthetic series (Figure 4.12). For the estimation of the spectrum, we used the same Welch method (using Hann window), keeping using the same values of the parameters M and P (150 and 90%, respectively).

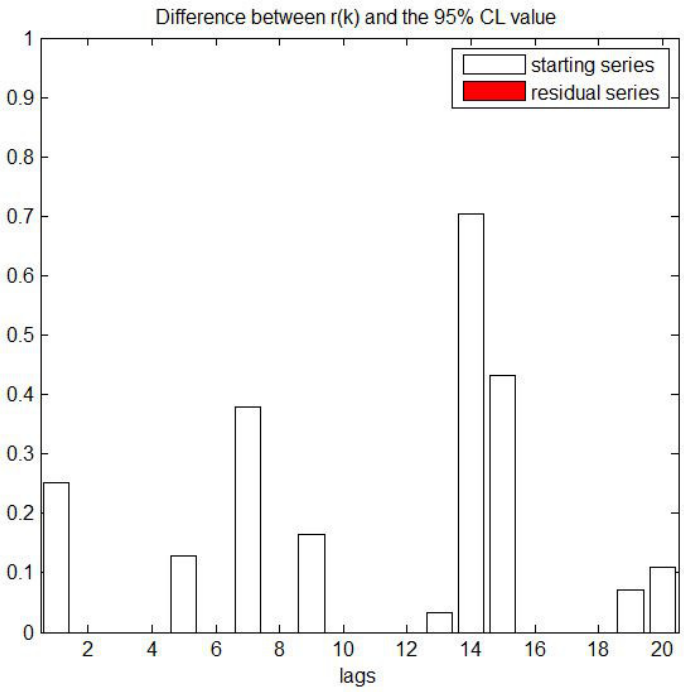

Figure 4.9: The difference between the autocorrelation coefficient and the value of the 95% confidence interval for each lag k for NOS. Considering the residual series, this quantity is null for each lag.

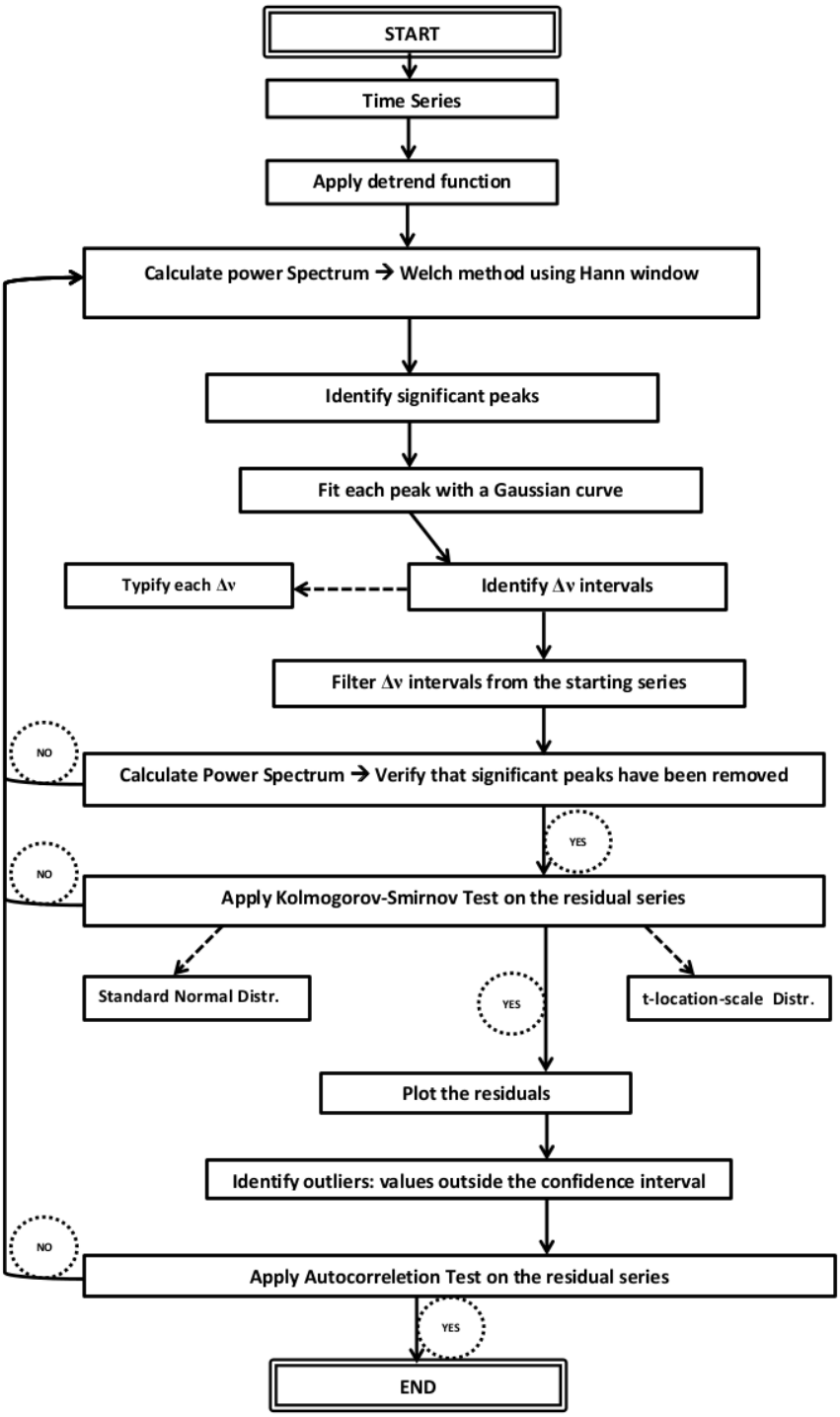

Figure 4.10: Brief block diagram of the performed analysis.

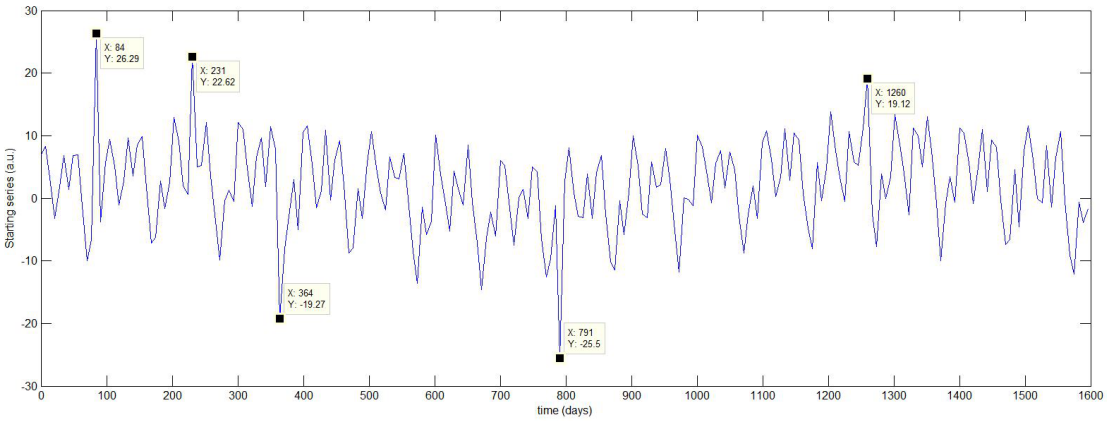

Figure 4.11: Synthetic series (OS), composed by a Deterministic, Stochastic and Linear trend signal. Five outliers have been added to the series at random positions (t=84, 231, 364, 791 and 1260 days).

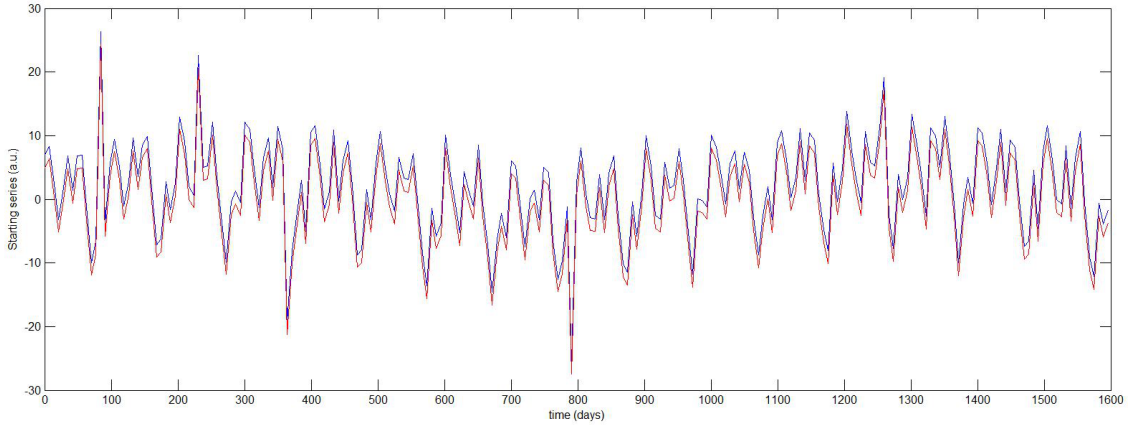

Figure 4.12: *detrend* function applied to the starting series (red) respect to the starting OS (blue).

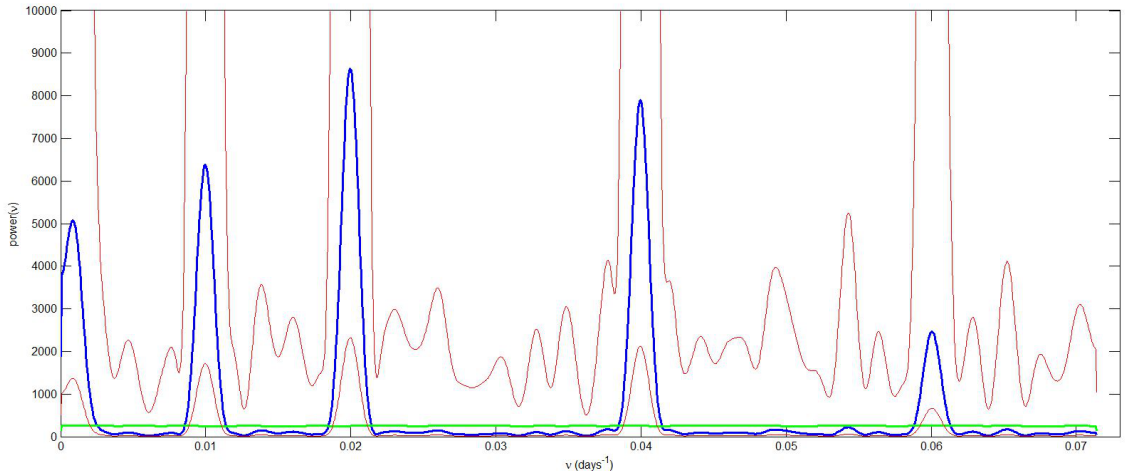

Figure 4.13: Power spectrum of OS, evaluated by Welch method, using Hann window with M=150 and P=90%, together with spectrum upper and lower limits considering confidence intervals at 95% (red) and the null spectrum (green).

The spectrum in Figure 4.13 shows the characteristic peaks of the synthetic series as well as the one of the previous case, even though is now possible to notice that the background is significantly noisier.

After the Gaussian fit of the peaks, we choose the 10% of the parameter a for the frequency intervals and we obtained the corresponding $\Delta\nu$ intervals (Table 4.3).

Table 4.3: $\Delta\nu$ $(days^{-1})$ intervals corresponding to 10% a (OS)

$\nu_{min}(days^{-1})$	$\nu_{max}(days^{-1})$
0	0.0022
0.0088	0.0111
0.0188	0.0212
0.0388	0.0411
0.0589	0.0612

The comparison between Table 4.3 and Table 4.1 shows that the identified frequency intervals are consistent and they correspond exactly to the Deterministic Signal we put inside the two initial synthetic series.

After the removal of the $\Delta\nu$ intervals, the residual series is subjected to the KStest, considering the case that the data in the input vector comes from a normal distribution and, if not, that they belong to a t-location-scale

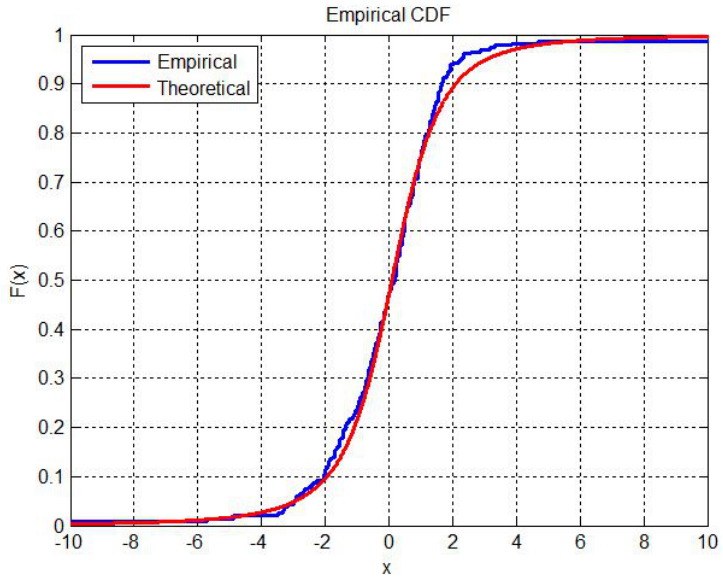

Figure 4.14: Cumulative distribution function of empirical (OS) and theoretical (t-location-scale) distributions.

distribution. The empirical and theoretical CDF and the PDF are shown in Figure 4.14 and 4.15. In this case, the test did not reject the null hypothesis for the t-location-scale distribution.

The residual series is represented by a bar graph, together with the corresponding confidence band. It is shown in Figure 4.16.

The five initial outliers are evidently outside the confidence interval. The filtered $\Delta\nu$ intervals are saved together with the percentage of the removed spectrum respect to the total spectrum (Table 4.4). Autocorrelation function

Table 4.4: $\Delta\nu$ $(days^{-1})$ intervals corresponding to 10% a (OS) and the percentage of the removed spectrum

$\nu_{min}(days^{-1})$	$\nu_{max}(days^{-1})$	%
0	0.0022	16
0.0088	0.0111	18
0.0188	0.0212	25
0.0388	0.0411	23
0.0589	0.0612	7

applied to our starting series with outliers shows a strong autocorrelation

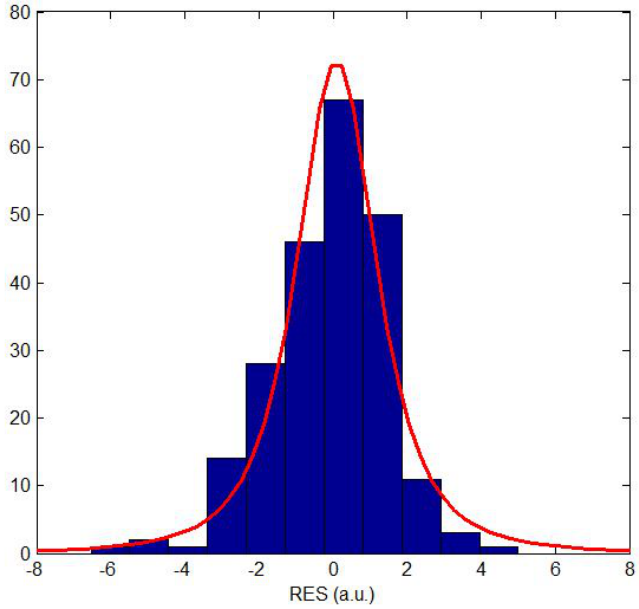

Figure 4.15: Probability density function of empirical (OS) and theoretical (t-location-scale) distributions.

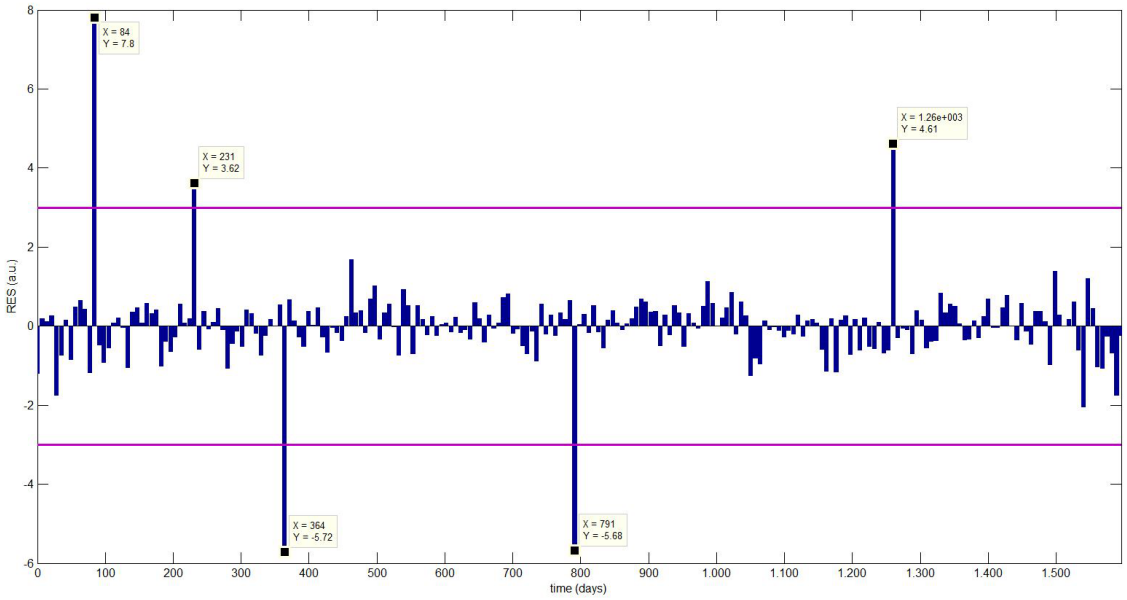

Figure 4.16: Residuals of the synthetic time series (OS).

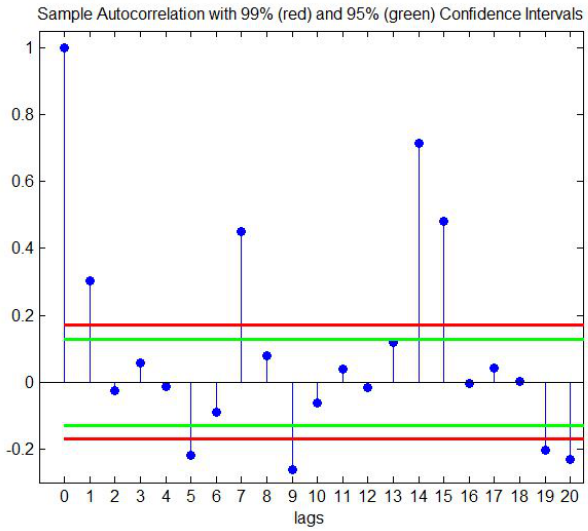

Figure 4.17: Correlogram of the starting series (OS).

(Figure 4.17).

The correlogram of the residual series is shown in Figure 4.18. It is possible to compare the initial and the final correlograms by the plot in Figure 4.19.

We can conclude that the algorithm of the removal of characteristic frequency bands is efficient.

It is important to remember that the aim of this algorithm is to identify anomalies with respect to the basic physical process, not to find the 'exact value' of the distribution. The one and only useful information is to find out if a particular element of the time series falls outside the confidence band.

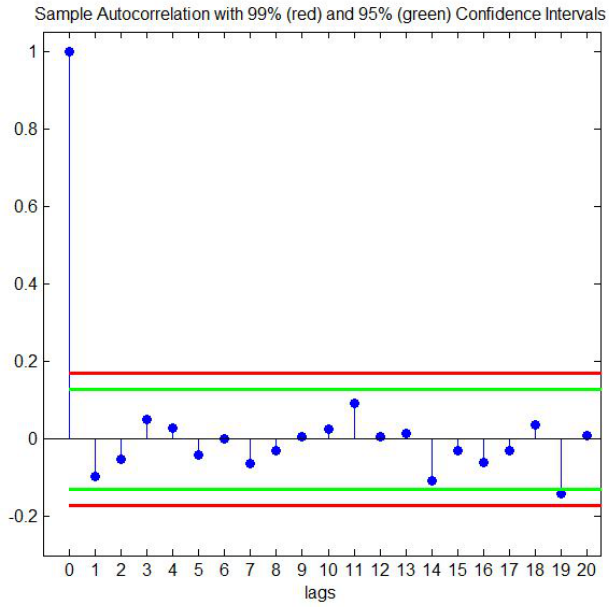

Figure 4.18: Correlogram of the residual series (OS).

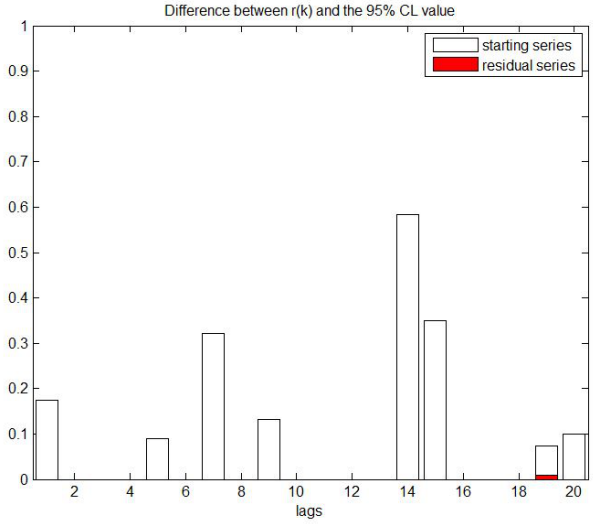

Figure 4.19: The difference between the autocorrelation coefficient and the value of the 95% confidence interval for each lag k for OS.

4.3 Analysis of uranium groundwater content in sampling sites located at LNGS-INFN: E1, E3, E3dx and E4

As previously described in Sections 1.3.1 and 2.3, the content of uranium in groundwater sampled in four sites, located inside the underground facilities at LNGS-INFN, has been weekly monitored since June, 2008, in order to give a contribution to the study of neutron flux inside the Laboratories, as well as for a better definition of radon groundwater transport processes through the cataclastic rocks. After the L'Aquila earthquake, the monitoring of uranium is useful to check if there is a possible correlation with energy release during seismic swarms.

The time series under investigation are composed of about 300 observations (six years of data). The sampling period is one week, so the sampling frequency is once a week, i.e.:

$$F_s = \frac{1}{7}\text{days}^{-1} \simeq 0.1429\text{days}^{-1}$$

For every time series, the same procedure of analysis has been applied. The complete time series of uranium content in site E1, E3, E3dx and E4 are shown in Figure 4.20.

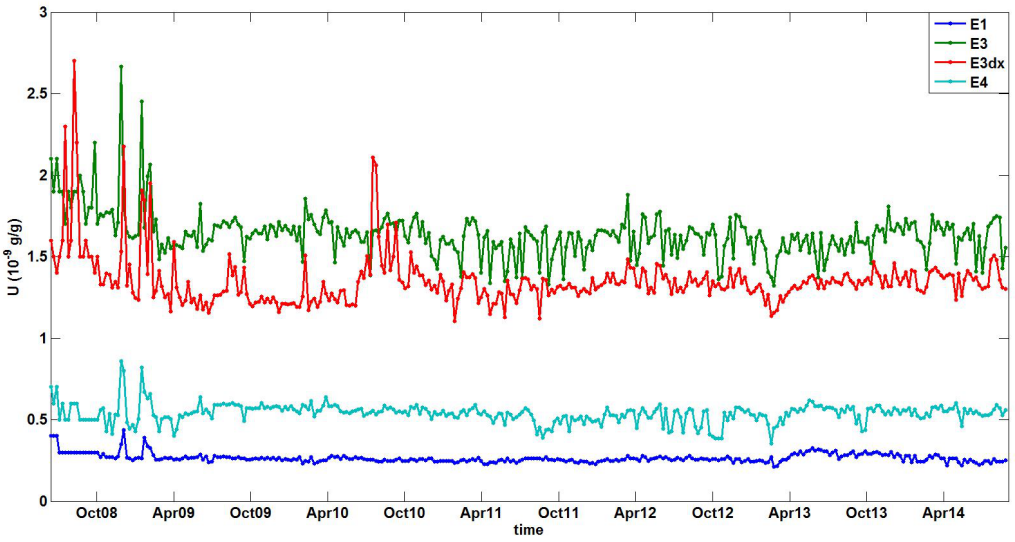

Figure 4.20: Uranium content time series in site E1 (blue), E3 (green), E3dx (red) and E4 (cyan). The accuracy is always less than 5%.

4.3.1 U in E1

U content in site E1 has the average lowest value respect to the other three sampling sites.

Although in Figure 4.20 the content of U in site E1 seems somehow steady, let's say "regular", except the initial (moderate) spike trend, actually the time series is anything but smooth. For the starting time series of U in E1, the same procedure as Sections 4.2.1 and 4.2.2 has been applied. E1 series has been detrended (Figure 4.21) and the algorithm of the time series analysis has been applied. For E1, a window length of M=150 and a percentage of P=25% have been chosen.

The spectrum estimation in Figure 4.22 clearly highlights the most predominant frequencies. In Table 4.5, frequencies relative to the peaks of the spectrum which contribution is more than 5% of the total spectrum are listed. In particular, the first frequency (main peak) corresponds to a time span of about 6 years. The seasonal frequency is evident (six months). The last peak is relative to a time span of about two months.

After the removal of the frequencies, the spectrum has been estimated again, in order to find out any possible residual frequency interval. The test has been rejected, as it's possible to verify in Figure 4.23 . In fact, it is possible to observe some residual frequencies. The first peak has not been

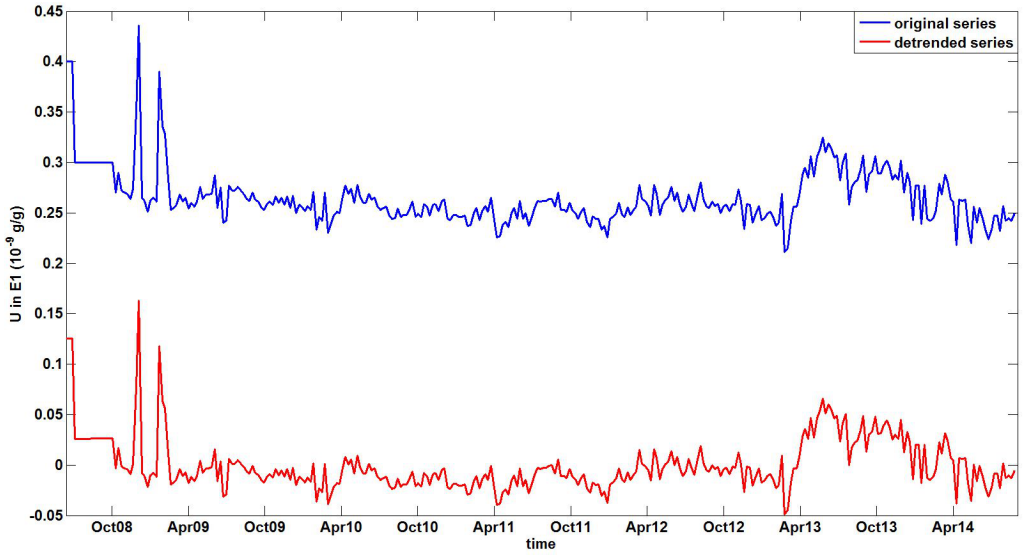

Figure 4.21: Uranium content time series in site E1 (blue). The accuracy is always less than 5%. The detrended time series is also shown (red).

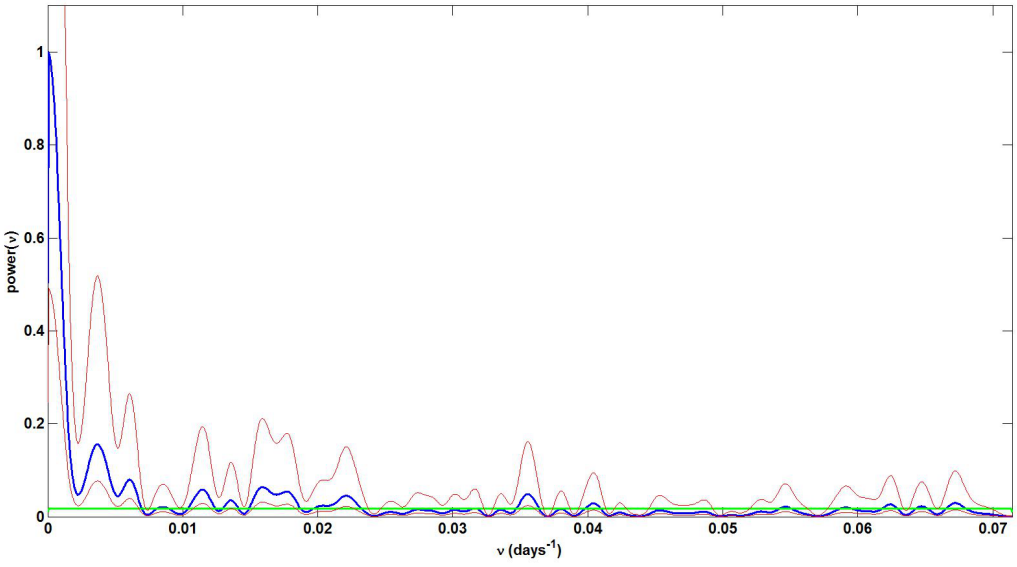

Figure 4.22: Spectrum estimation of the time series of uranium content in site E1, together with spectrum upper and lower limits considering confidence intervals at 95% (red) and the null spectrum (green).

Table 4.5: $\Delta\nu$ ($days^{-1}$) intervals corresponding to 60% a (U in E1) and the percentage of the removed spectrum

$\nu_{min}(days^{-1})$	$\nu_{max}(days^{-1})$	%
0	0.0010	34
0.0029	0.0045	9
0.0155	0.0167	5

correctly filtered, the one year peak has appeared, while the frequency of six months is still in the spectrum. For these reasons, other iterations are required.

After five iterations, the spectrum is completely under the threshold, as it is shown in Figure 4.24.

The distribution of the residual series is then fitted with a normal distribution.

The theoretical curve well describes our residual data (Figure 4.26), as shown in the KStest (see Figure 4.25).

The residual series, together with the 99.7% C.L., is shown in Figure 4.28.

The outliers of the series are shown by means of labels, in order to outline their positions and to compare them with the outliers of the other uranium time series.

We can reveal four outliers. Three of them are prominent and they occupy the time span November, 2008-January, 2009.

The autocorrelation test did not reject the null hypothesis at 99% C.L.; the correlogram of the starting and residual series are shown in Figure 4.29.

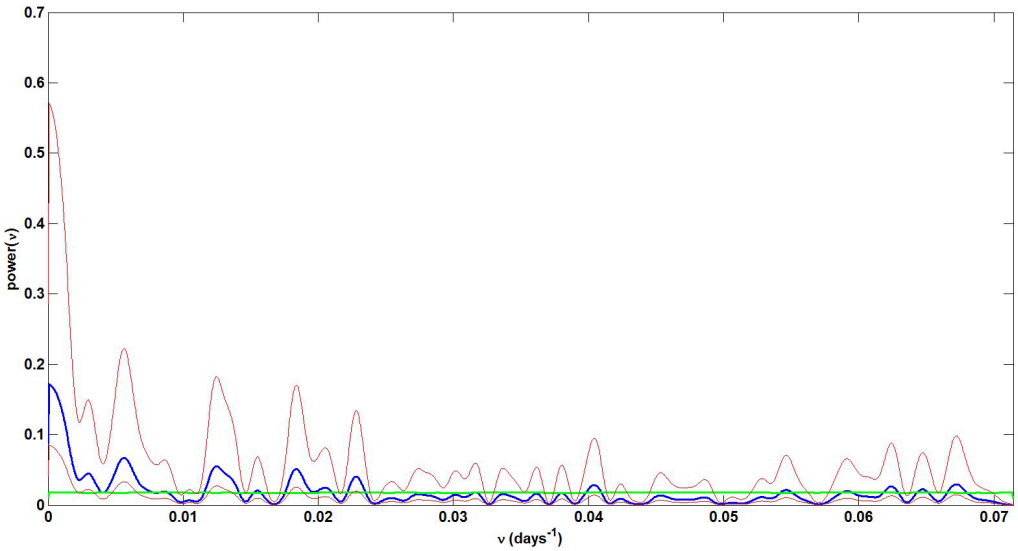

Figure 4.23: Spectrum estimation of the time series of uranium content in site E1, after the frequency removal, together with spectrum upper and lower limits considering confidence intervals at 95% (red) and the null spectrum (green). It is possible to observe some residual frequencies. The first peak has not been correctly filtered. The one year peak has appeared. The frequency of six months is still in the spectrum, so that other iterations are required.

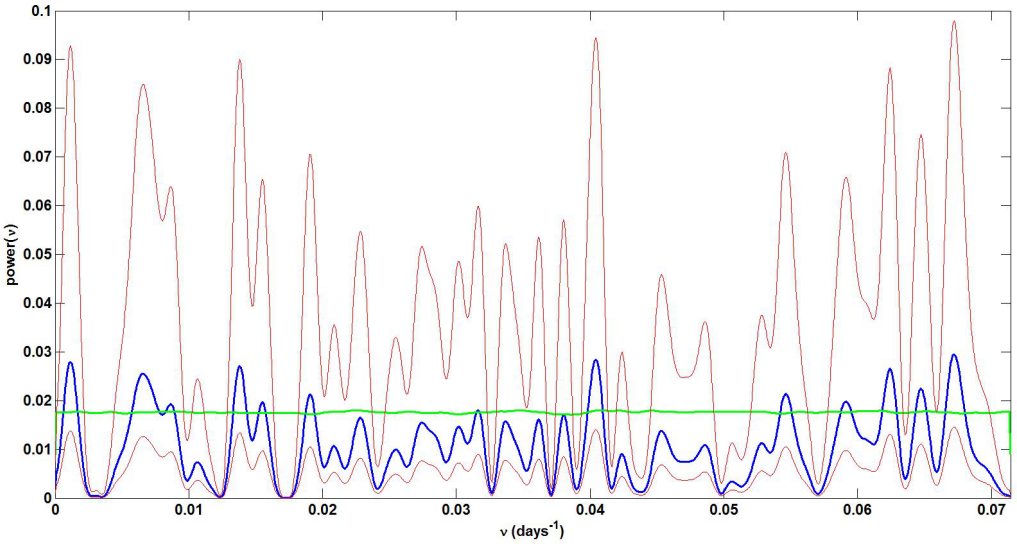

Figure 4.24: Spectrum estimation of the time series of uranium content in site E1, after the frequency removal procedure, together with spectrum upper and lower limits considering confidence intervals at 95% (red) and the null spectrum (green). It is possible to observe no residual frequencies.

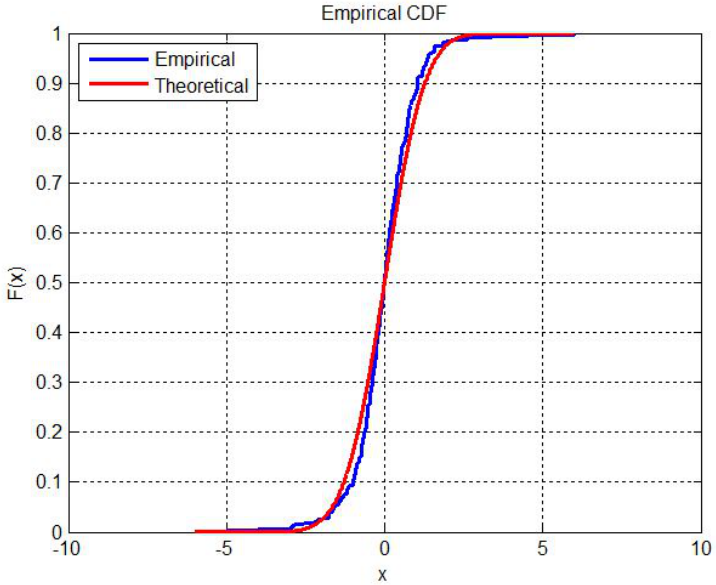

Figure 4.25: Cumulative distribution function of empirical (E1) and theoretical (normal) distributions.

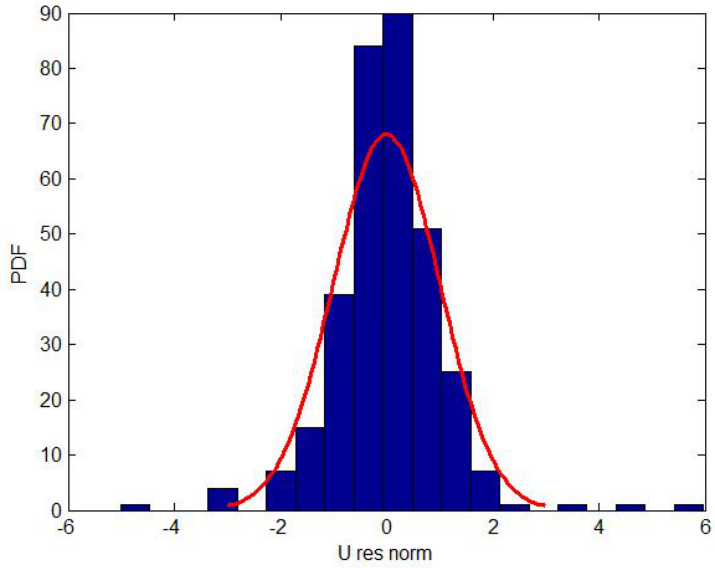

Figure 4.26: Probability density function of empirical (E1) and theoretical (normal) distributions.

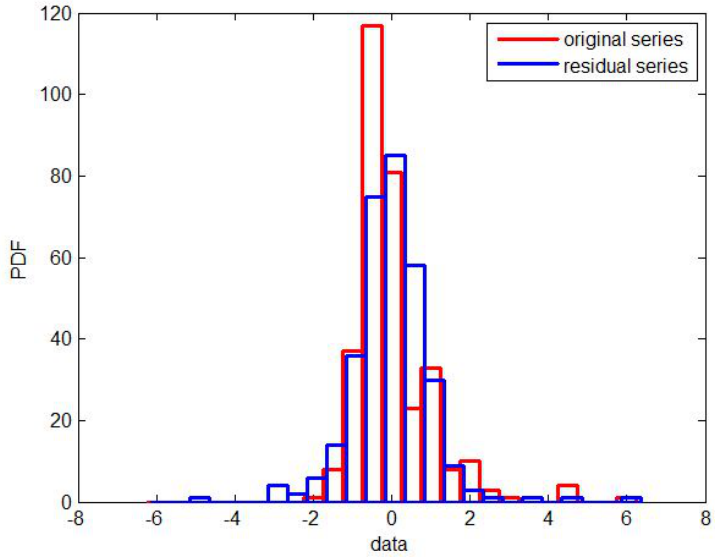

Figure 4.27: Probability density function of E1, before (red) and after (blue) the analysis.

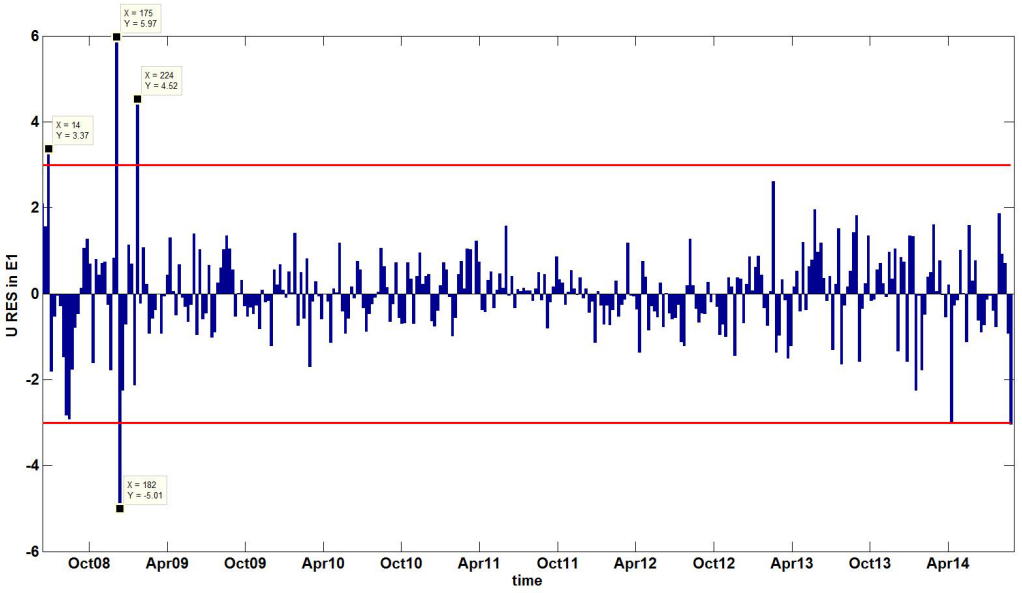

Figure 4.28: Residuals of the U time series in E1. The outliers are identified where the modulus is greater than three times the estimated standard deviation, i.e., C.L. of 99.7% .

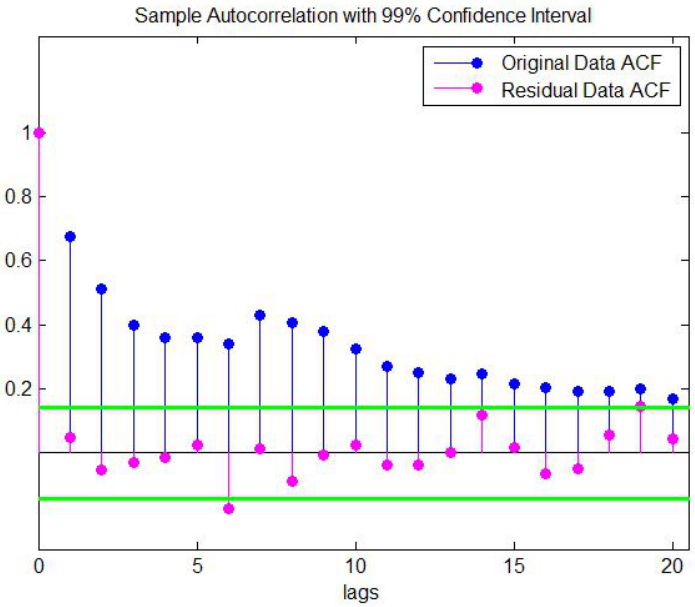

Figure 4.29: Correlogram of the starting and residual series (E1).

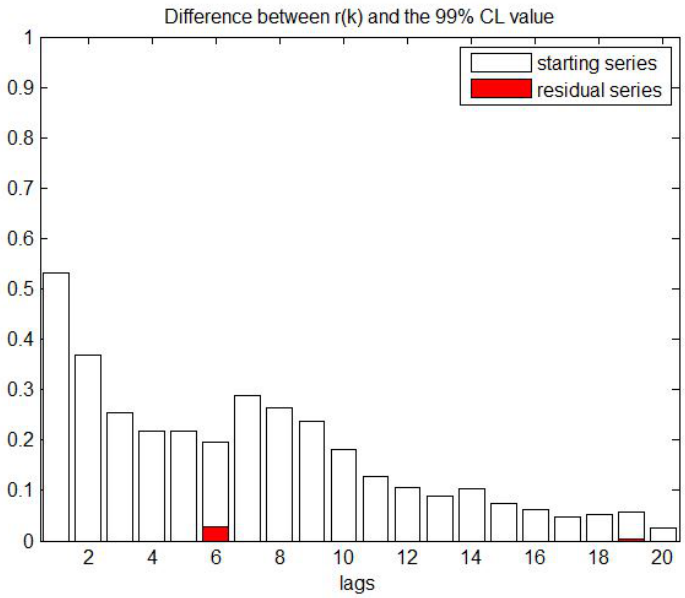

Figure 4.30: The difference between the autocorrelation coefficient and the value of the 99% confidence interval for each lag k for E1.

4.3.2 U in E3

U in site E3 has a different behavior respect to site E1. The mean value of the series is appreciably higher and a more prominent spike trend is evident. The starting time series and the detrended time series are shown in Figure 4.31. The power spectrum has been estimated by the choice of M=150 and P=60.

This spectrum turns out to be more noisy than E1's. This is evident if we look at Figure 4.32 and Table 4.6: for example, the percentage of the removed spectrum is lower for the main frequency intervals.

Figure 4.33 shows that frequencies have not been correctly removed. It is therefore necessary to apply the filter procedure again. In fact, until the lower limit of the spectrum lies under the threshold, this iteration is required. The condition is verified after the second removal procedure: in Figure 4.34 the final spectrum is shown.

It is now possible to characterize the residual distribution and the residual series.

The KStest for a normal distribution did not reject the null hypothesis at the 95% C.L. The CDF and the PDF are shown in Figures 4.35 and 4.36.

The residual series in Figure 4.38 shows the presence of some outliers at

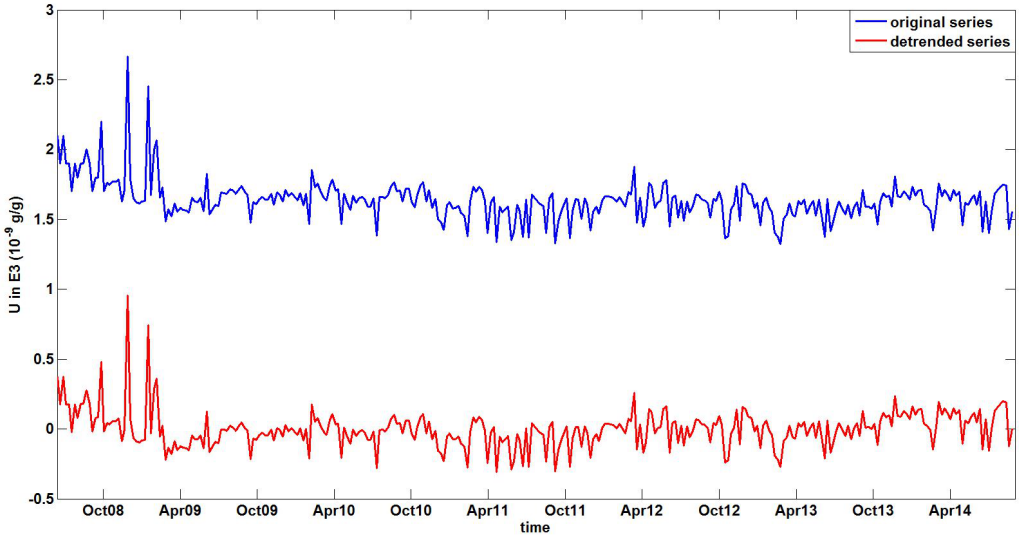

Figure 4.31: Uranium content time series in site E3 (blue). The accuracy is always less than 5%. The detrended time series is also shown (red).

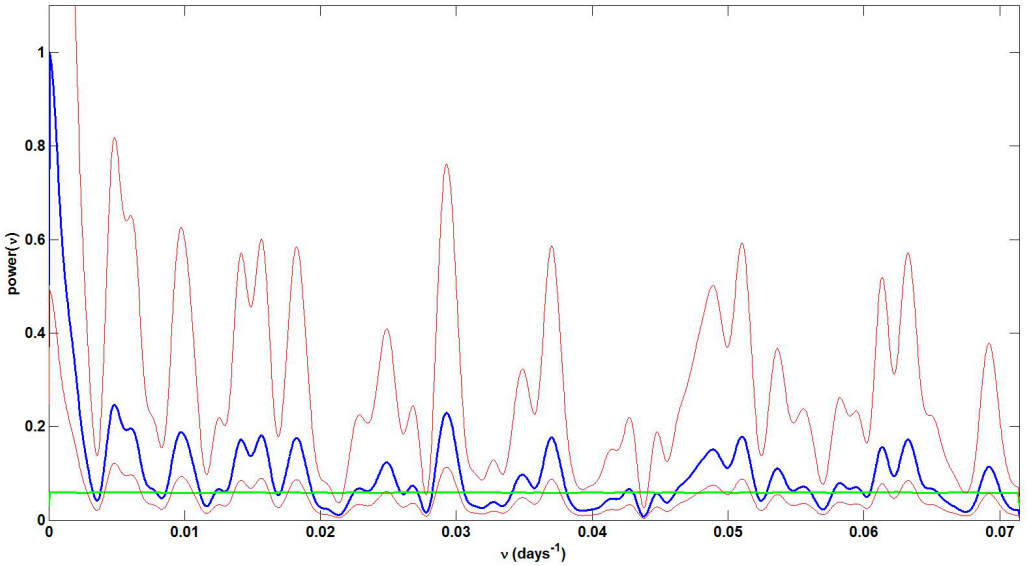

Figure 4.32: Spectrum estimation of the time series of uranium content in site E3, together with spectrum upper and lower limits considering confidence intervals at 95% (red) and the null spectrum (green).

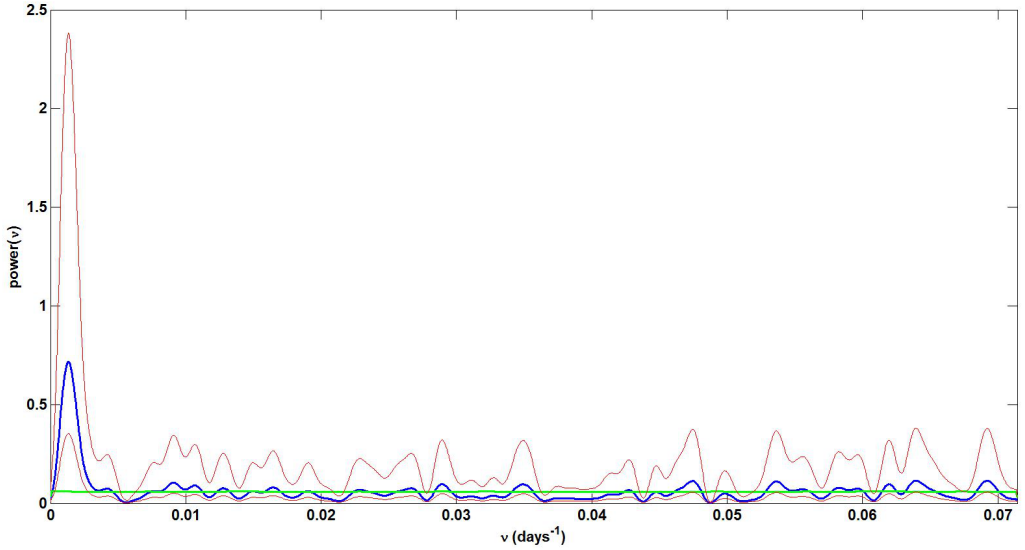

Figure 4.33: Spectrum estimation of the time series of uranium content in site E3, after the frequency removal, together with spectrum upper and lower limits considering confidence intervals at 95% (red) and the null spectrum (green). It is possible to observe one residual frequency .

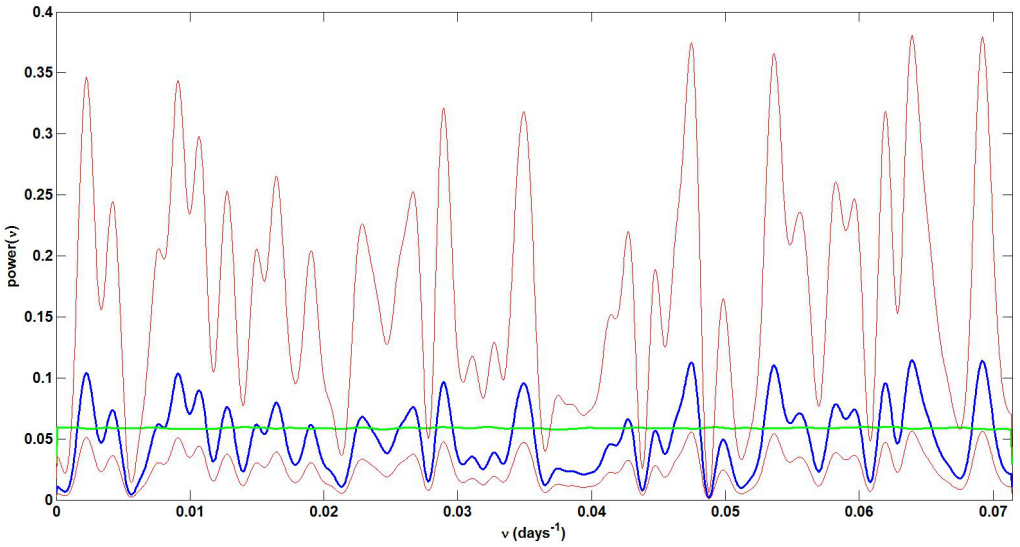

Figure 4.34: Spectrum estimation of the time series of uranium content in site E3, after the frequency removal, together with spectrum upper and lower limits considering confidence intervals at 95% (red) and the null spectrum (green). It is now possible to observe no residual frequencies.

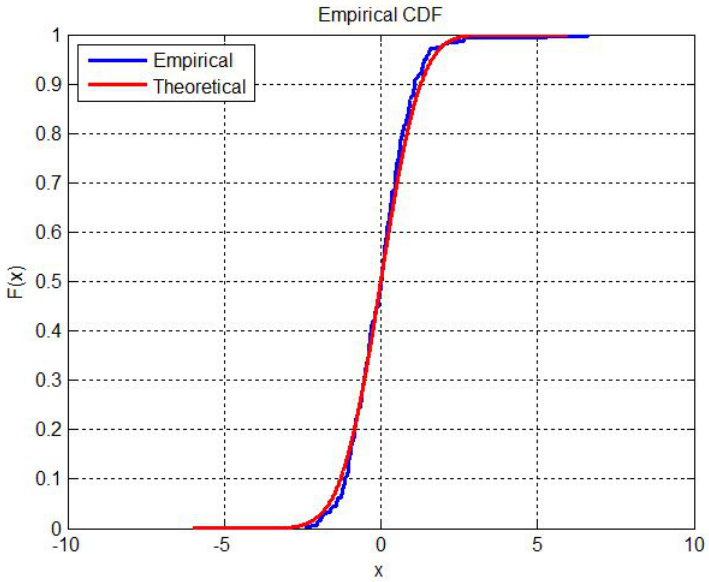

Figure 4.35: Cumulative distribution function of empirical (E3) and theoretical (normal) distributions.

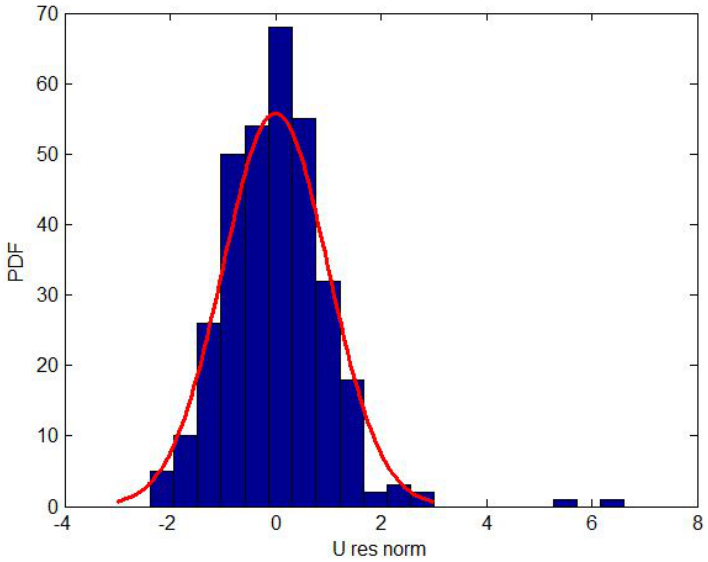

Figure 4.36: Probability density function of empirical (E3) and theoretical (normal) distributions.

Table 4.6: $\Delta\nu$ ($days^{-1}$) intervals corresponding to 70% a (U in E3) and the percentage of the removed spectrum

$\nu_{min}(days^{-1})$	$\nu_{max}(days^{-1})$	%
0	0.0010	21
0.0045	0.0065	8
0.0050	0.0076	5
0.0138	0.0160	7
0.0289	0.0298	6

the beginning of the series, as for the site E1. To be sure of the removal of the characteristic frequencies, the autocorrelation test has been applied: the test did not reject the null hypothesis at 99% C.L. The analysis well explains how the procedure has been efficacious (see Figures 4.39 and 4.40).

In the residual series of U in E3, we can see two outliers around December, 2008-January, 2009.

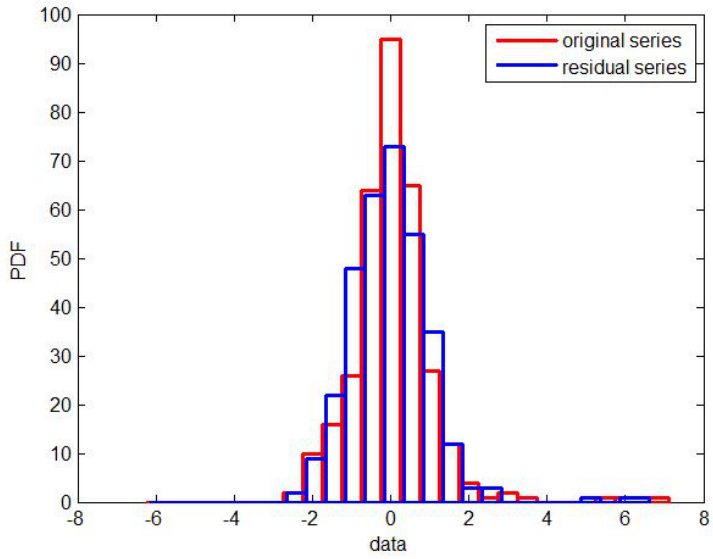

Figure 4.37: Probability density function of E3, before (red) and after (blue) the analysis.

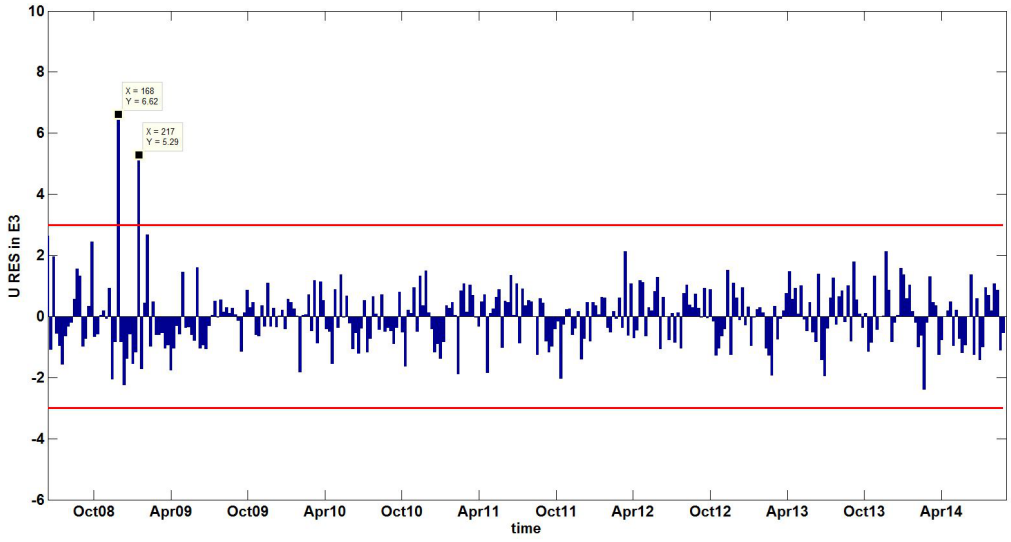

Figure 4.38: Residuals of the U time series in E3. The outliers are identified where the modulus is greater than three times the estimated standard deviation, i.e., C.L. of 99.7%.

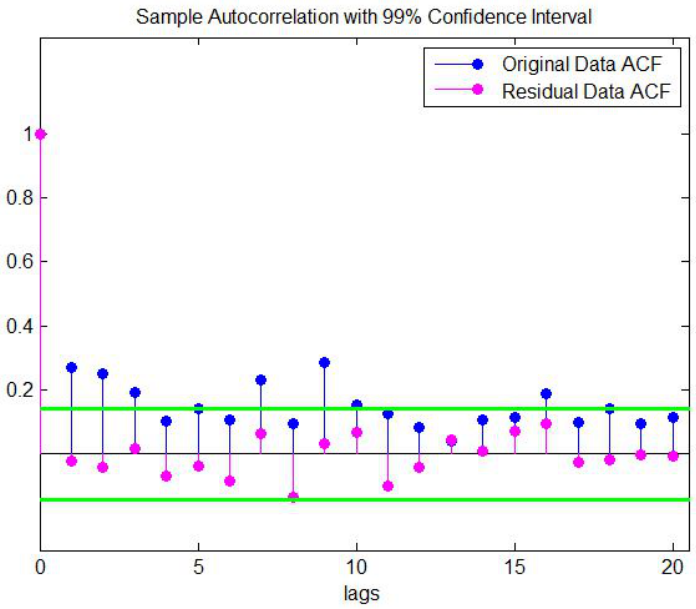

Figure 4.39: Correlogram of the starting and residual series (E3).

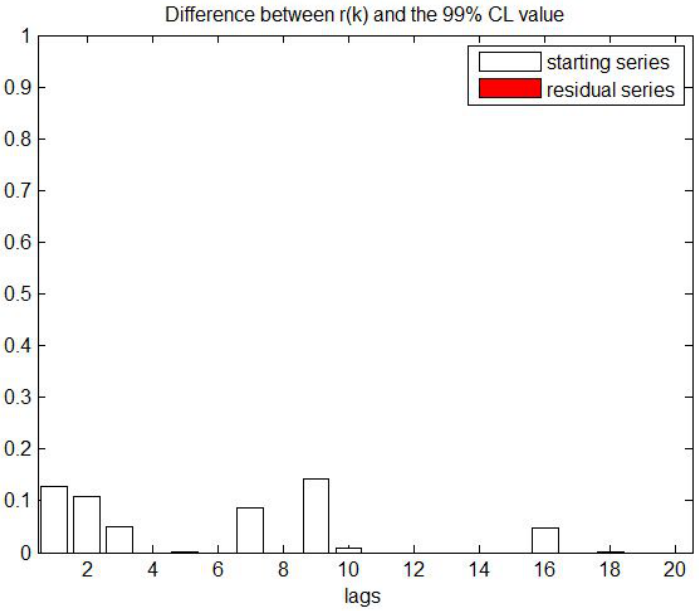

Figure 4.40: The difference between the autocorrelation coefficient and the value of the 99% confidence interval for each lag k for E3. Considering the residual series, this quantity is null for each lag.

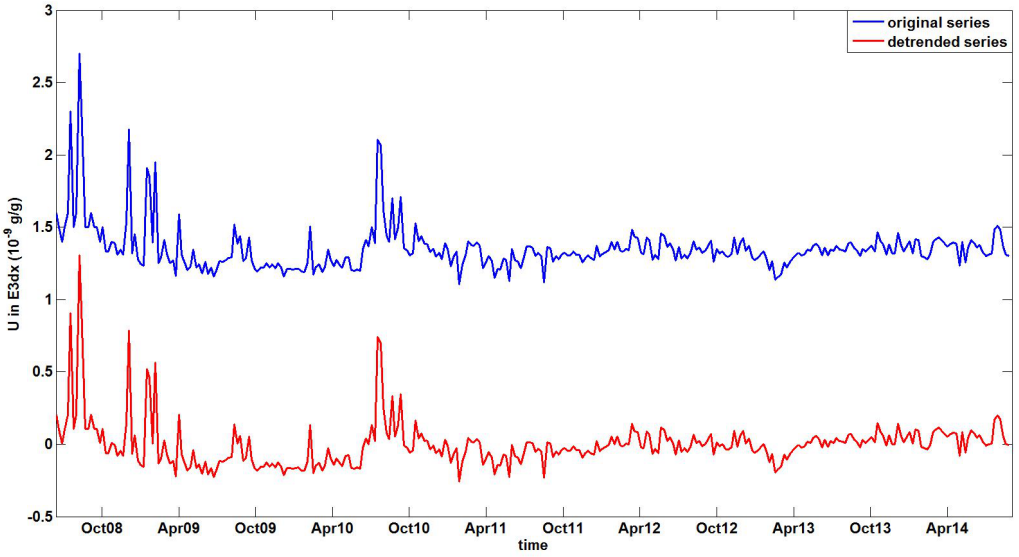

Figure 4.41: Uranium content time series in site E3dx (blue). The accuracy is always less than 5%. The detrended time series is also shown (red).

4.3.3 U in E3dx

As we stated in Section 1.3.1, site E3dx is very significant, due to its position, as it is the nearest site to cataclastic rocks. It is also characteristic for a better description of water-rock interactions through the main overthrust fault.

Since the initial rough series, an intense spike trend both before April, 2009, and before October, 2010 is evident. The detrended series and the original series are shown in Figure 4.41. The power spectrum has been estimated by the choice of M=150 and P=60.

The spectrum of E3dx is very noisy, as only the first three peaks need to be considered (Table 4.7). Looking at the second iteration (spectrum of Figure 4.43), some residual frequencies had still to be removed. After one more iteration, the spectrum in Figure 4.44 is completely under the threshold.

The hypothesis of normality after the last iteration has been rejected by the KStest. Figures 4.45 and 4.47 show the CDF and the PDF of the residual series, respectively. On the contrary, the test with a Student's t distribution has not been rejected at the 95% confidence level. The failure of normality test could indicate the existence of a random component in the residual time series that is different from a white noise. In this case, further investigation is needed.

Differently from sites E1 and E3, in site E3dx we can reveal many outliers

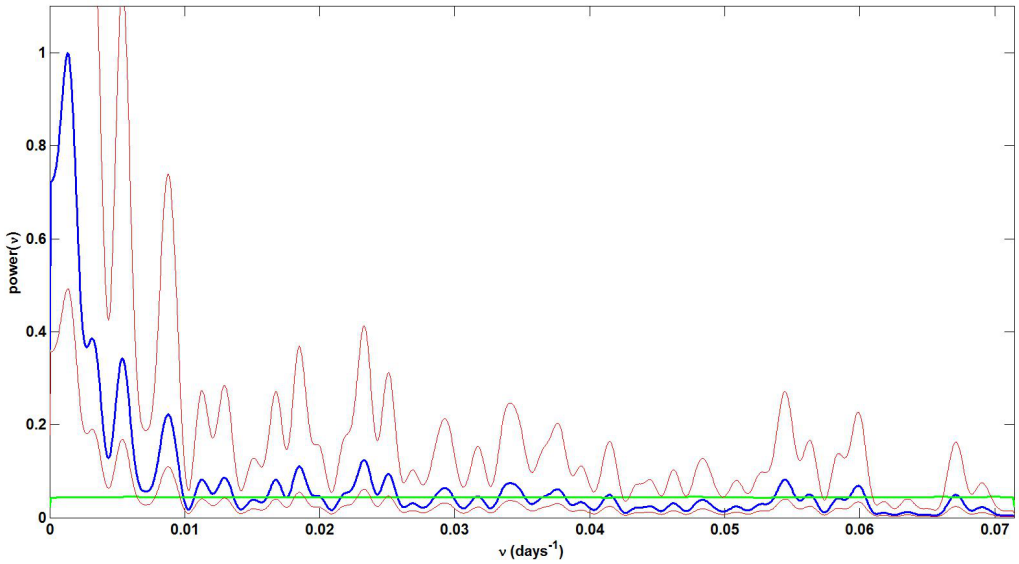

Figure 4.42: Spectrum estimation of the time series of uranium content in site E3dx, together with spectrum upper and lower limits considering confidence intervals at 95% (red) and the null spectrum (green).

before February, 2009, and also one at the end of June, 2010.

Table 4.7: $\Delta\nu$ $(days^{-1})$ intervals corresponding to 80% a (U in E3dx) and the percentage of the removed spectrum

$\nu_{min}(days^{-1})$	$\nu_{max}(days^{-1})$	%
0	0.0018	22
0.0026	0.0035	6
0.0050	0.0058	5

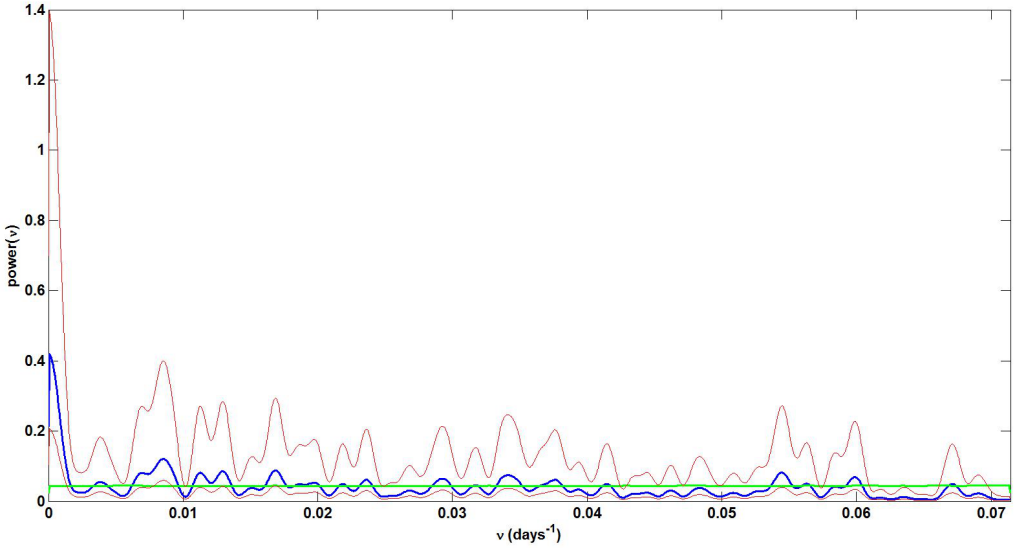

Figure 4.43: Spectrum estimation of the time series of uranium content in site E3dx, after the frequency removal, together with spectrum upper and lower limits considering confidence intervals at 95% (red) and the null spectrum (green). It is possible to observe two residual frequencies.

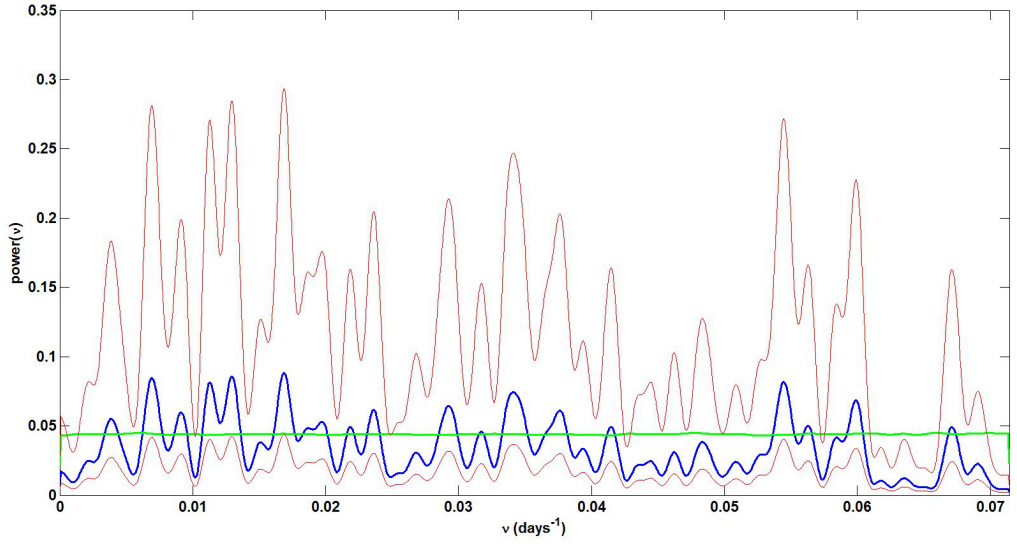

Figure 4.44: Spectrum estimation of the time series of uranium content in site E3dx, after the frequency removal, together with spectrum upper and lower limits considering confidence intervals at 95% (red) and the null spectrum (green). It is now possible to observe no residual frequencies.

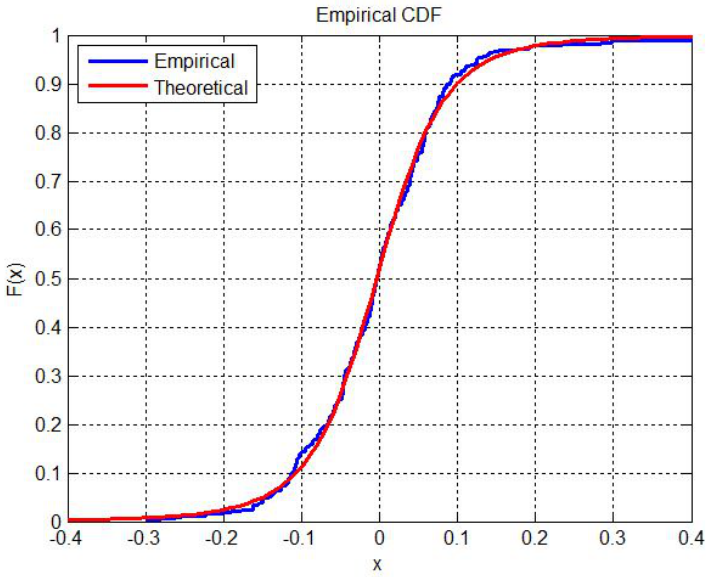

Figure 4.45: Cumulative distribution function of empirical (E3dx) and theoretical (normal) distributions.

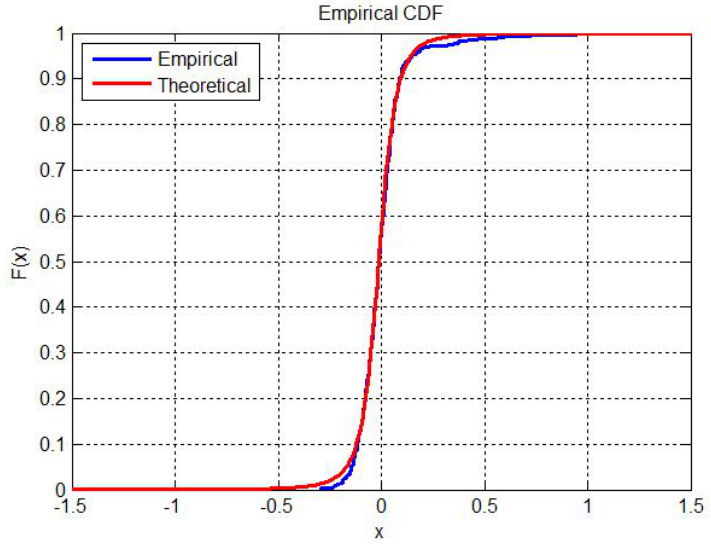

Figure 4.46: Cumulative distribution function of empirical (E3dx) and theoretical (Student's t) distributions.

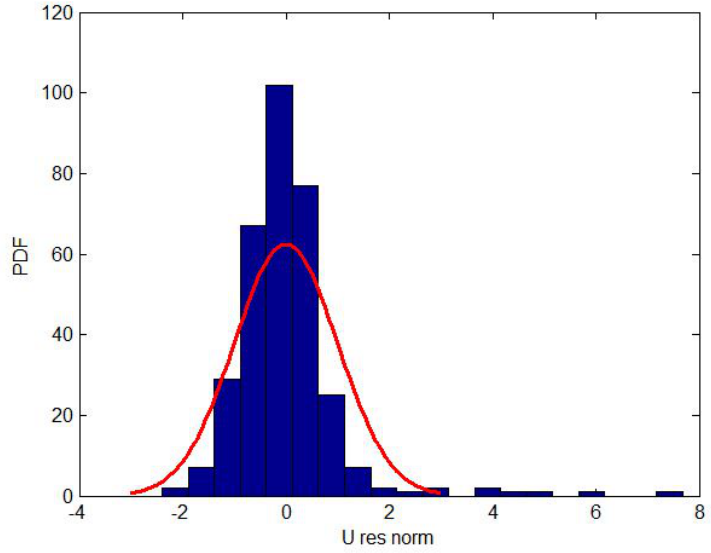

Figure 4.47: Probability density function of empirical (E3dx) and theoretical (normal) distributions.

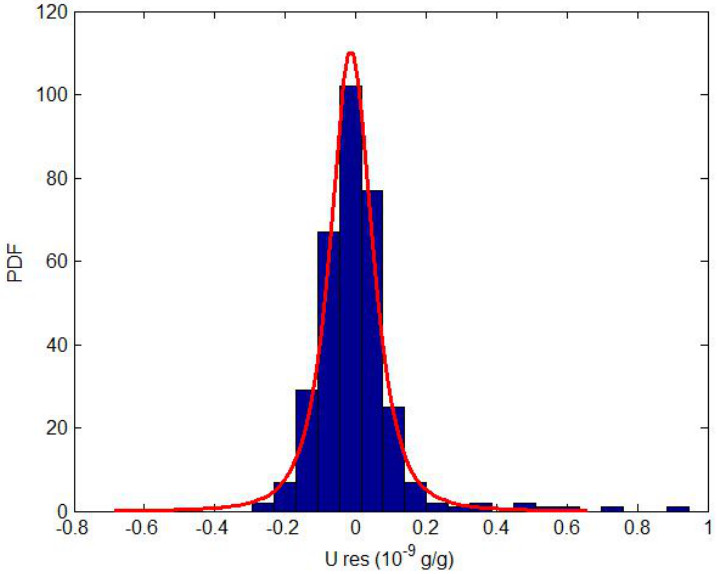

Figure 4.48: Probability density function of empirical (E3dx) and theoretical (Student's t) distributions.

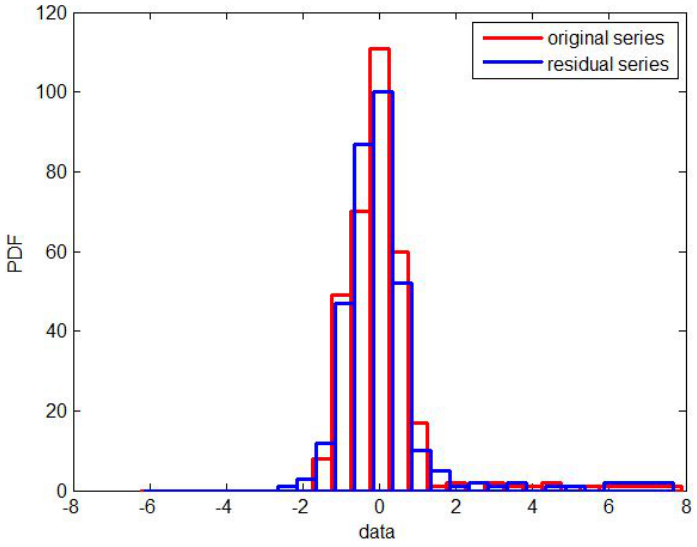

Figure 4.49: Probability density function of E3dx, before (red) and after (blue) the analysis.

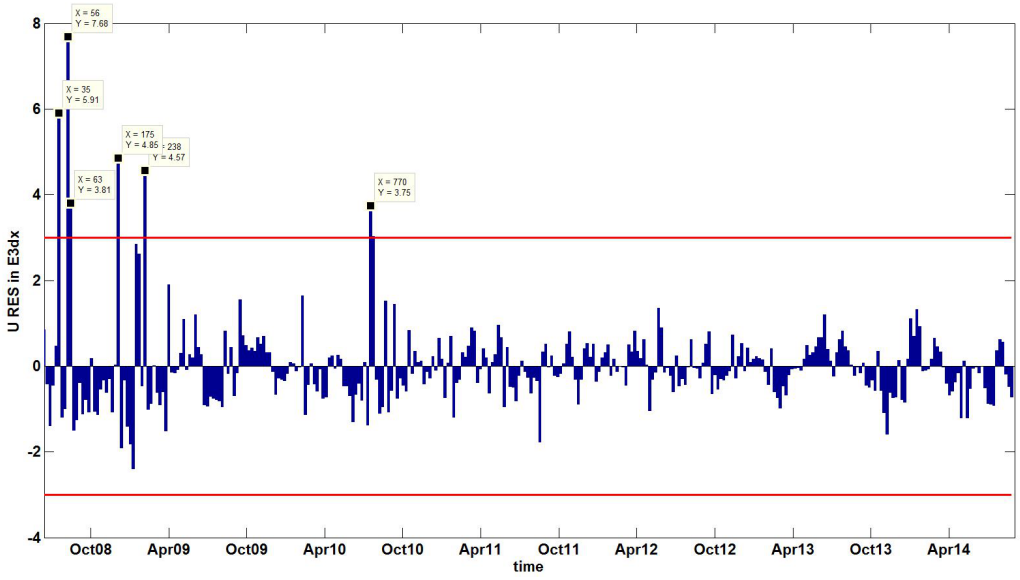

Figure 4.50: Residuals of the U time series in E3dx. The outliers are identified where the modulus is greater than three times the estimated standard deviation.

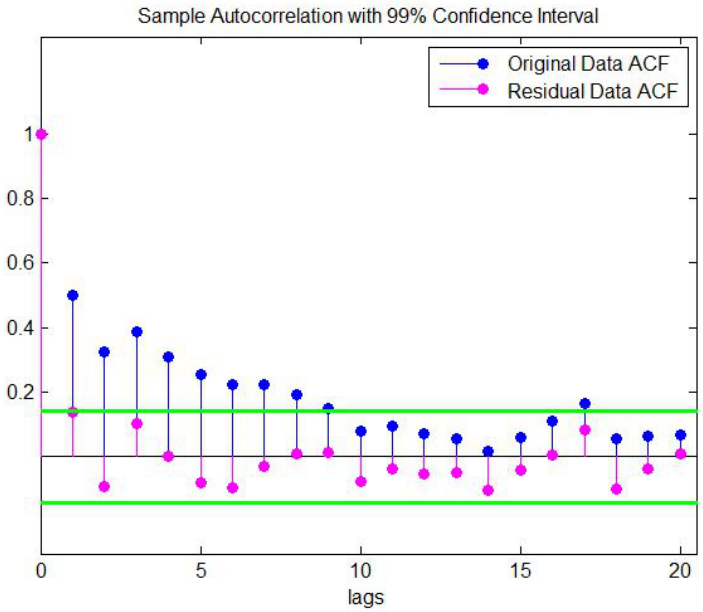

Figure 4.51: Correlogram of the starting and residual series (E3dx).

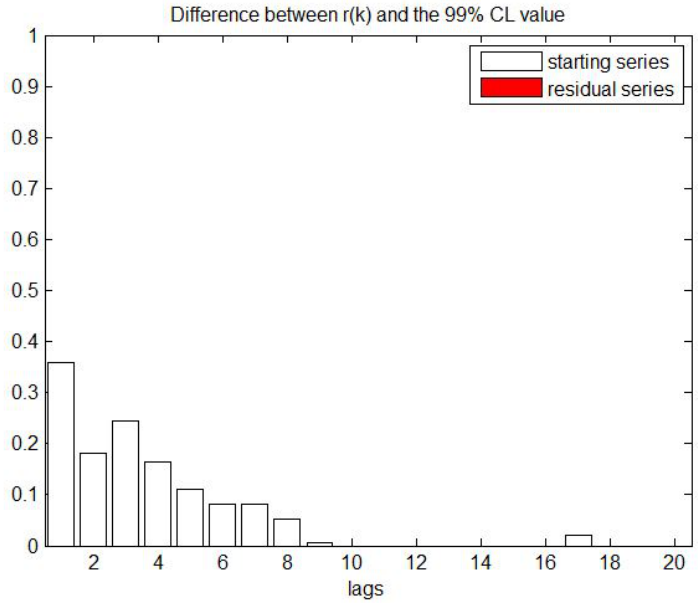

Figure 4.52: The difference between the autocorrelation coefficient and the value of the 99% confidence interval for each lag k for E3dx. Considering the residual series, this quantity is null for each lag.

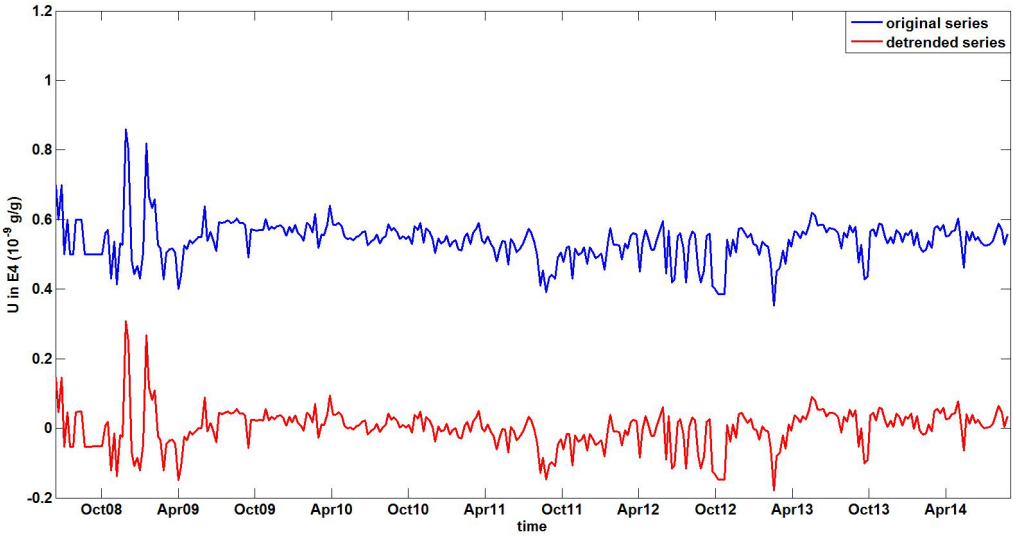

Figure 4.53: Uranium content time series in site E4 (blue). The accuracy is always less than 5%. The detrended time series is also shown (red).

4.3.4 U in E4

Uranium time series in site E4 is anything but regular. In Figure 4.53, a strange behavior from July, 2012 to April, 2013 is observed. This could be possibly due to different problems: environmental and/or experimental conditions, different sensitivity of instruments, etc.

The power spectrum has been estimated by the choice of M=125 and P=15 and the main frequency intervals are shown in Figure 4.54 and Table 4.8.

Table 4.8: $\Delta\nu$ ($days^{-1}$) intervals corresponding to 80% a (U in E4) and the percentage of the removed spectrum

$\nu_{min}(days^{-1})$	$\nu_{max}(days^{-1})$	%
0	0.0013	20
0.0031	0.0047	7
0.0086	0.0105	8
0.0153	0.0162	6

After some attempts, the power spectrum of U in site E4 has been brought under the threshold (Figures 4.54, 4.55 and 4.56). The KStest did not reject

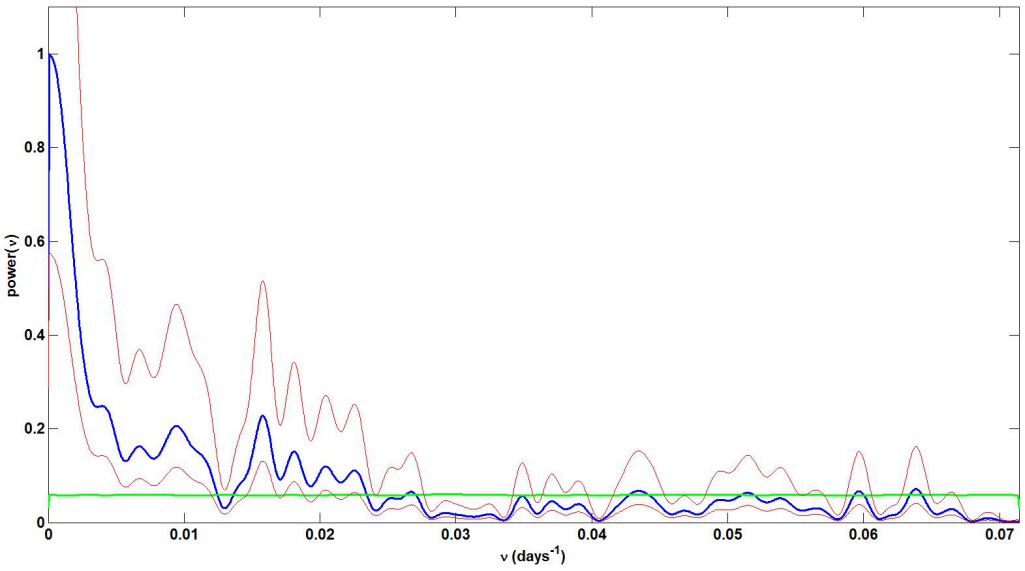

Figure 4.54: Spectrum estimation of the time series of uranium content in site E4, together with spectrum upper and lower limits considering confidence intervals at 95% (red) and the null spectrum (green).

the null hypothesis of normality. The CDF and the PDF are shown in Figures 4.57 and 4.58. Nevertheless, the autocorrelation test rejected the null hypothesis at the considered C.L. (Figures 4.61 and 4.62): the residual series does not present completely randomness features.

As in the case of E1 and E3, we can reveal some outliers in the time span November, 2008-January, 2009, only.

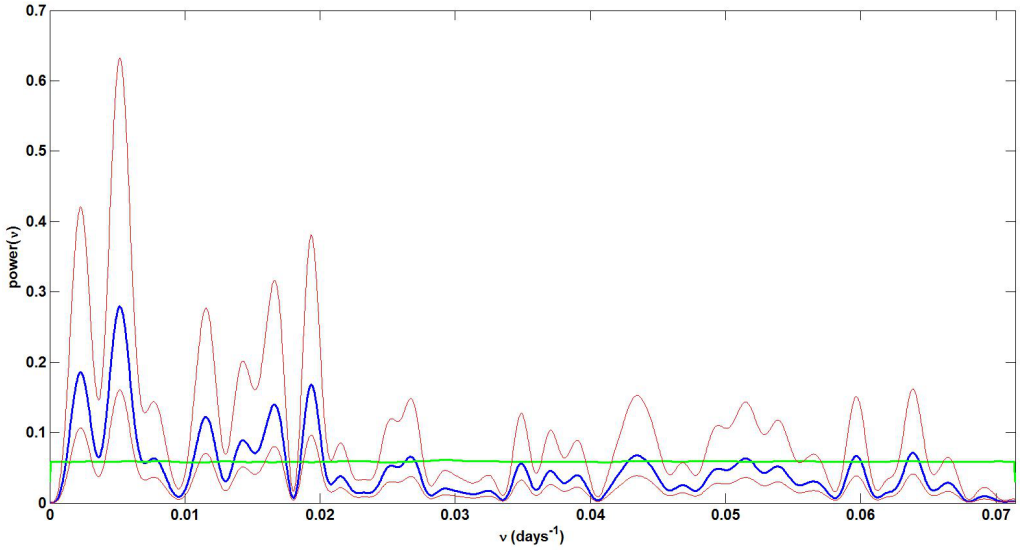

Figure 4.55: Spectrum estimation of the time series of uranium content in site E4, after the frequency removal, together with spectrum upper and lower limits considering confidence intervals at 95% (red) and the null spectrum (green). It is possible to observe some residual frequencies .

4.4 Comparison between uranium groundwater anomalies and seismic activity

In Table 4.9 the values of KStest and LBtest are shown. We can state that, in

Table 4.9: Value of the KStest and LBtest parameters for sites E1, E3, E3dx and E4

	KStest			LBtest		
	h	D	D^*	h	Q	Q^*
E1	0	0.0743	0.0746	0	35.69	37.57
E3	0	0.0486	0.0746	0	24.62	37.57
E3dx	0	0.1519	0.0746	0	33.70	37.57
E4	0	0.0539	0.0746	1	48.29	37.57

the case of every sampling site, the KStest did not reject the null hypothesis, while the LBtest did reject the null hypothesis of no autocorrelation in the residual series of site E4.

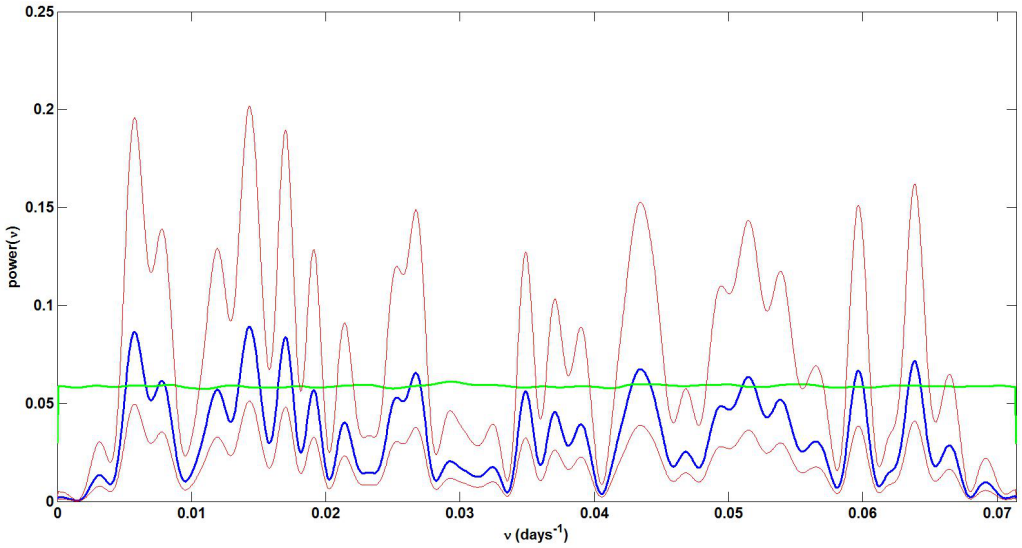

Figure 4.56: Spectrum estimation of the time series of uranium content in site E4, after the frequency removal, together with spectrum upper and lower limits considering confidence intervals at 95% (red) and the null spectrum (green). It is now possible to observe no residual frequencies.

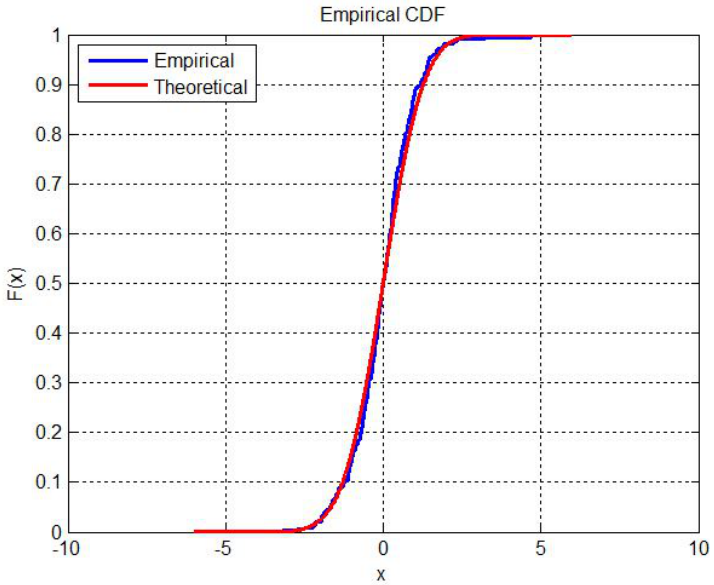

Figure 4.57: Cumulative distribution function of empirical (E4) and theoretical (normal) distributions.

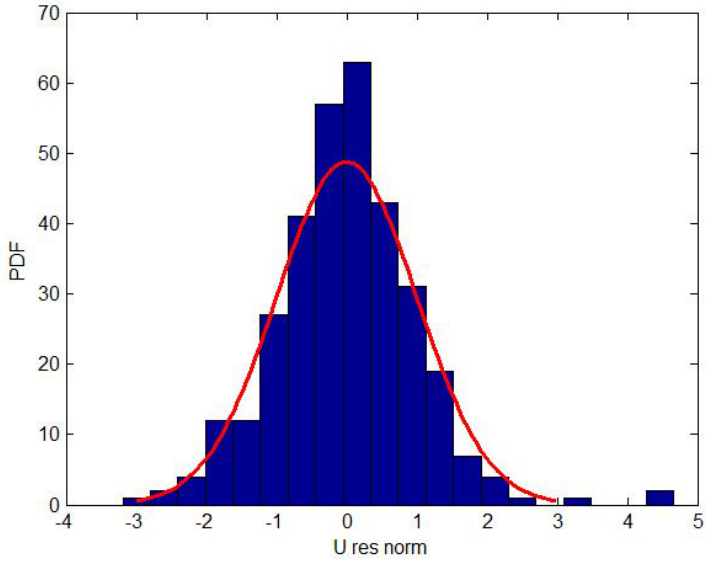

Figure 4.58: Probability density function of empirical (E4) and theoretical (normal) distributions.

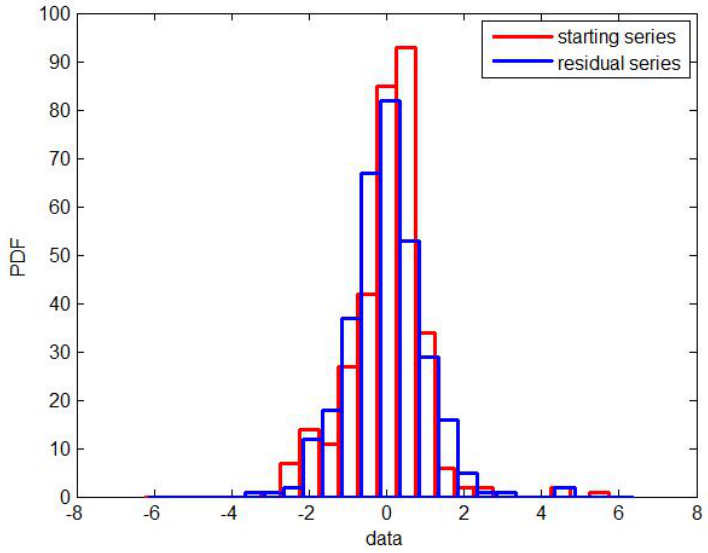

Figure 4.59: Probability density function of E4, before (red) and after (blue) the analysis.

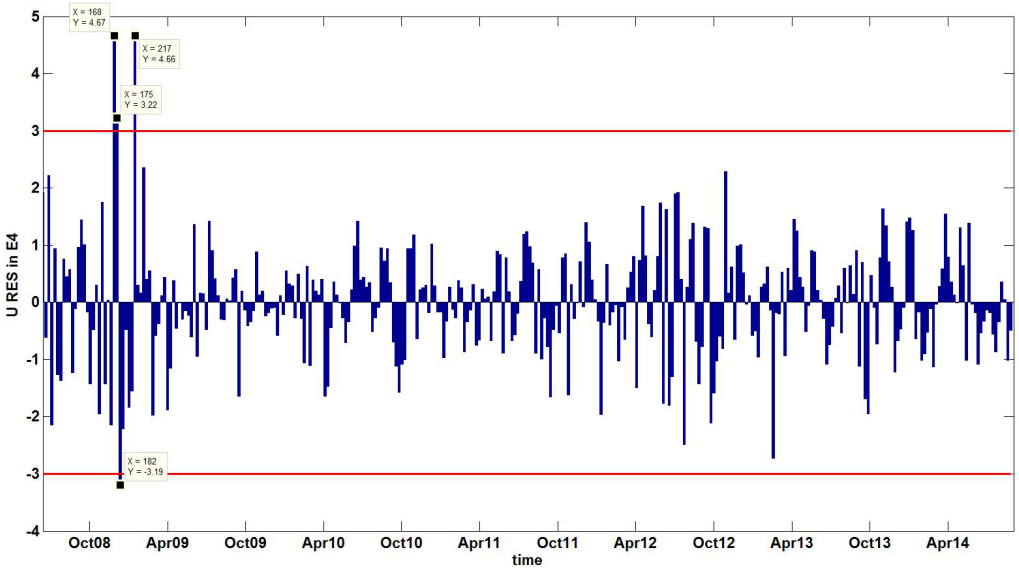

Figure 4.60: Residuals of the U time series in E4. The outliers are identified where the modulus is greater than three times the estimated standard deviation, i.e., C.L. of 99.7%.

We are now able to discuss if uranium in groundwater could be a potential strain indicator of geodynamic processes occurring before an earthquake.

Uranium groundwater residual series of samples E1, E3, E3dx and E4 are shown together with the seismic activity time spans identified in Chapter 3. In Figure 4.63 it is possible to observe that, before the L'Aquila earthquake, uranium in groundwater sampled in all four sites shows some spike-like anomalies. These anomalies are not related to hydrological pattern, because the seasonal contribution has been subtracted during the analysis of time series (Sections 4.3.1-4.3.4). These U anomalies in groundwater are detected until the beginning of February, 2009, i.e. until the beginning of the time span that we identified as Period A (see Table 4.10). However, during the main shock and aftershocks the variations in the U content were small and we did not reveal any anomalous value.

Before the beginning of Period B, one anomaly is observable only in site E3dx (end of June, 2010).

Period C and Period D are not preceded by any anomalous value.

A possible physical explanation of uranium anomalies observed before the L'Aquila earthquake might be the progressive increase of deep CO_2 fluxes at middle-lower crustal levels. Petrological and geophysical modeling explains how carbon is efficiently cycled in the upper mantle beneath Italy and the

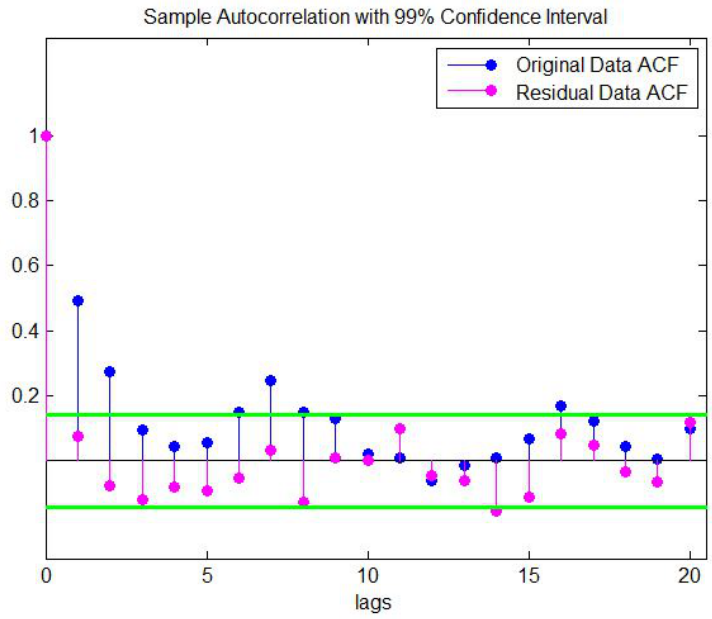

Figure 4.61: Correlogram of the starting and residual series (E4). Although the ACF is under the threshold at many lags, the autocorrelation test rejected the null hypothesis of complete randomness.

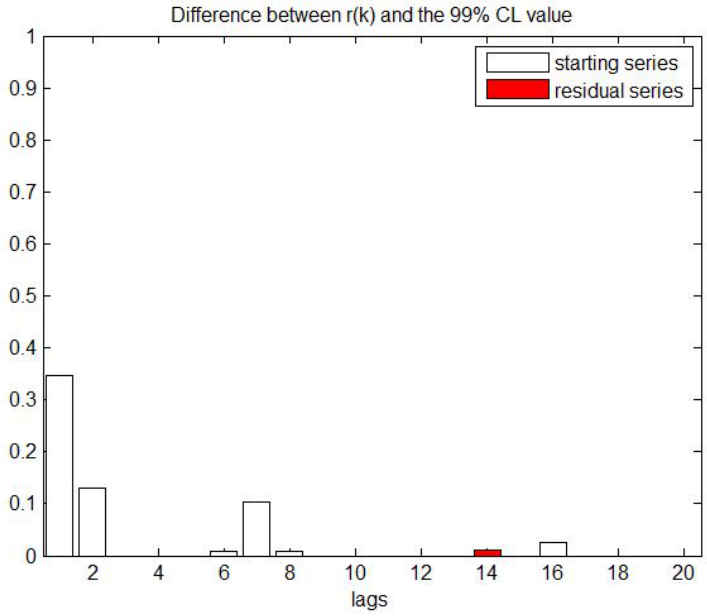

Figure 4.62: The difference between the autocorrelation coefficient and the value of the 99% confidence interval for each lag k for E4.

Western Mediterranean region at the Ma scale, via low-fractions of carbonate melts generated by melting of carbonate-rich lithologies of the subducted Adriatic lithosphere, induced by the progressive rise of mantle temperatures behind the eastward-retreating subducting plate (see Section 1.2 and Figure 4.64).

During the upwelling, part of the CO_2 could not reach the surface and could remain trapped beneath the Moho and the lower crust, especially where continental crust is thick. The entrapment of this CO_2 could origin over-pressurized reservoirs, rich of noble gases, U, Th, K and other incompatible elements. These facilitate seismogenesis, in normal fault areas.

Fault mechanisms are highly influenced by fluids, by their pore pressure, their chemistry and the variation of friction along the fault plane.

Fluids play a major role, triggering the rupture, and they are passively squeezed out during seismic events. Low amounts of CO_2 in zones of active faults are sufficient to give the aquifer efficient on dissolving carbonate wall rock.

The process could be summarized by three steps: the subduction causes the plate melting

$$CaCO_3 + Q \rightarrow CaO + CO_2 \tag{4.20}$$

Table 4.10: Outliers of the residual uranium time series

date	E1	E3	$E3_{dx}$	E4
07/07/08	x			
28/07/08			x	
18/08/08			x	
25/08/08			x	
09/12/08		x		x
16/12/08	x		x	x
22/12/08	x			x
26/01/09		x		x
02/02/09	x			
16/02/09			x	
28/06/10			x	

carbon dioxide in contact with water produces carbonic acid

$$CO_2 + H_2O \rightarrow H_2CO_3 \tag{4.21}$$

furthermore

$$H_2CO_3 \rightarrow H^+ + HCO_3^- \tag{4.22}$$

the result is an acid solution: carbonate acts as base to rise the pH, so that the rock is dissolved. In this case, in chemical analysis of groundwater, it is possible to find excesses of Mg and Ca, in association with excess of uranium content.

Throughout the seismic process, the lower part of the crust is constantly subject to shear, while the upper crust is locked. During this time interval, the volume between the upper crust and the lower crust should suffer dilatancy: fluids are expected to fill in the fractures formed during the interseismic period. The separation produces a weak volume of rocks that sustain the hanging wall until it suddenly falls down to refill the stretched volume. This process is shown by the main shock of an earthquake. The fluids previously introduced are squeezed out. After the collapse, the hanging wall is expected to gradually adjust to its new position, generating a long sequence of aftershocks, as those observed after the main event of April 6^{th}, 2009 of the L'Aquila swarm.

Plastino et al. (2011) proposed the progressive increase of deep CO_2 fluxes at middle-lower crustal levels as a possible physical explanation of U anomalies observed before the L'Aquila earthquake, where the area is cross-cut by several NW-SE trending active normal faults (see Figure 3.1, Section 3.1.1).

We can conclude that, in our analysis, uranium groundwater content shows an unusual behavior during the preparation phase of a seismic event: the available data suggest a possible relationship between the magnitude of the seismic swarm and the size of U anomalies, i.e. the largest the seismic event (in terms of the magnitude of the main earthquake and the number of events of the swarm), the largest the modulus and the number of outliers preceding it. Nevertheless, in order to justify this hypothesis, further observations are required. Moreover, differently from Swarms A and B, we did not observe any anomalous value in U quantities before Swarms C and D. This might be due to the different structures which have been involved in these four periods of increased seismicity: as we stated before, upwelling of CO_2 is favored in normal fault areas (as in the case of the L'Aquila earthquake and Swarm B), while it is inhibited in thrust fault areas (where Swarms C and D occurred, see Figure 3.17, Section 3.2.3).

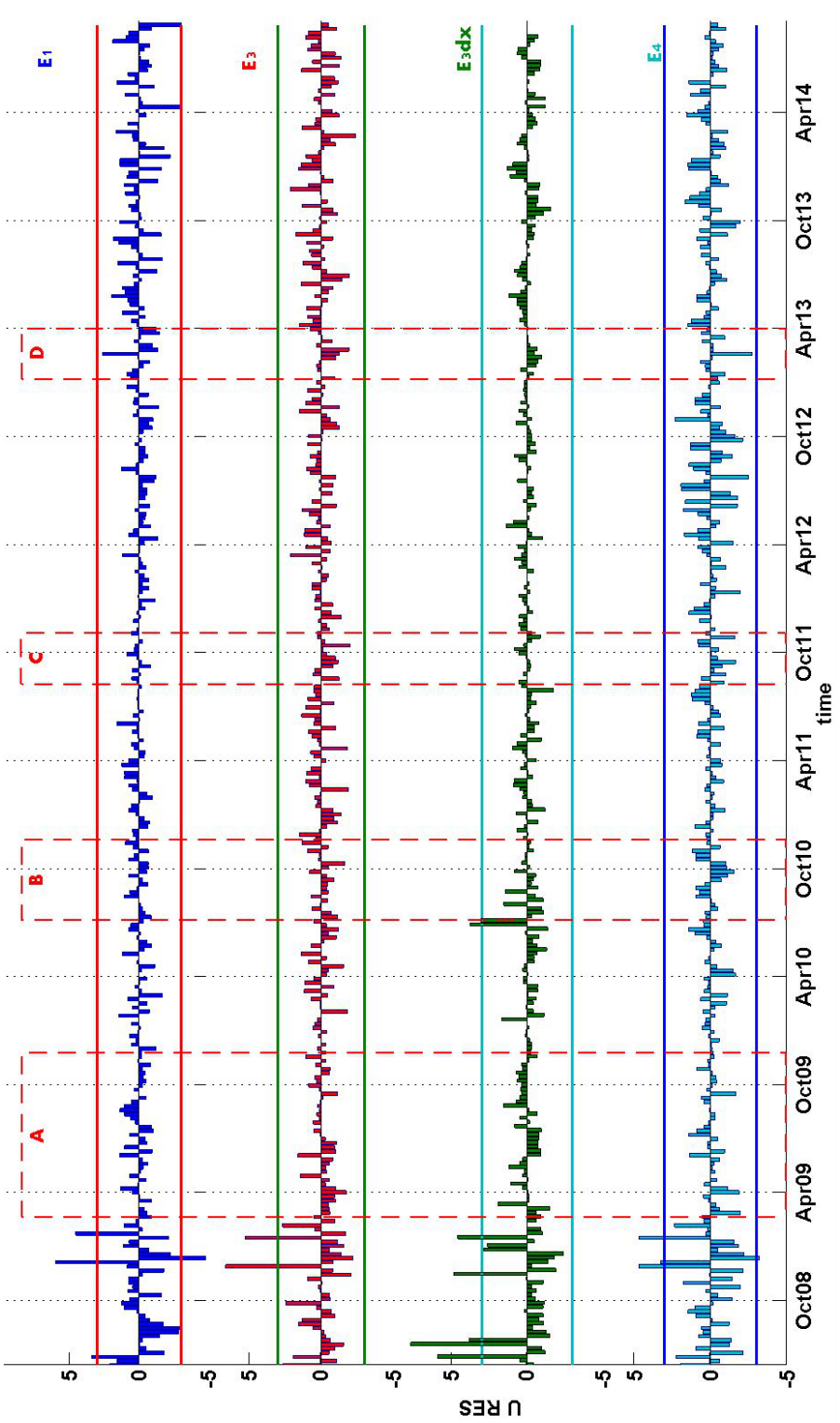

Figure 4.63: Residual U time series for sites E1 (blue bars), E3 (red bars), E3dx (green bars) and E4 (cyan bars), together with A (February-December, 2009), Period B (July-December, 2010), Period C (August-November, 2011) and D (January-April, 2013) (dashed red rectangles). Uranium groundwater anomalies are identified before the L'Aquila earthquake in all four sites, differently from the other three seismic activations.

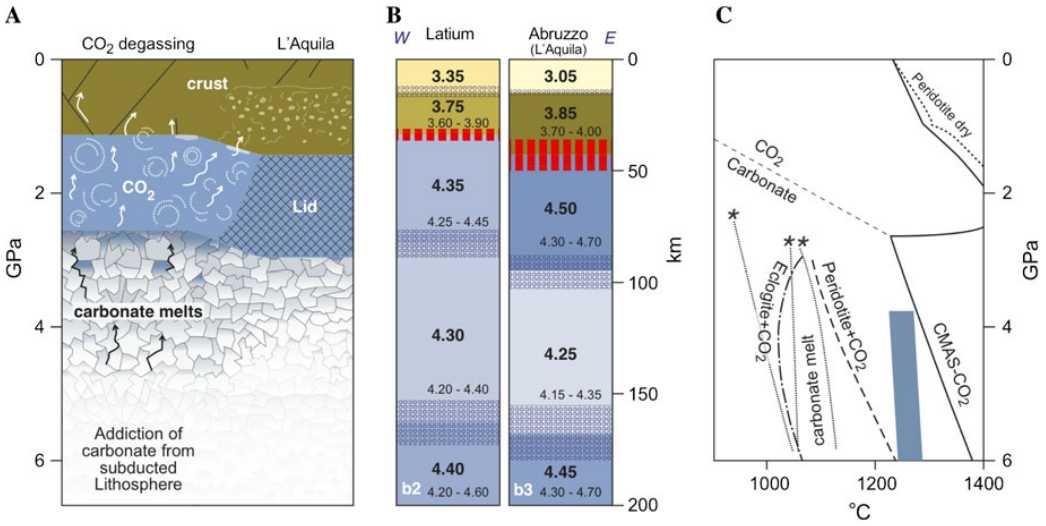

Figure 4.64: The generation and evolution of deep mantle-derived CO2 (A); velocity models of seismic waves (km/s) as function of depth (B), for Lazio (b2) and Abruzzo (b3); p-T graph showing the effects of CO_2 in the upper mantle. In blu, an estimation of temperatures of mantle as function of pressure (C) (Plastino et al., 2011).

Conclusions

Nowadays, the efficacy of many observables proposed as possible precursory signals is, at most, unproven, mainly due to the lack of appropriate, systematic and longterm observations. In fact, strong earthquakes rarely occurs and every presumed precursor can be often affected by its own variability, that it is not linked to seismic features (Buscema and Ruggieri, 2011).

The aim of this thesis was the investigation of the pattern of uranium concentration in groundwater sampled at Gran Sasso National Laboratories (LNGS-INFN) during a time span of about six years: we showed that the anomalies of this observable could be linked to the seismic activity around LNGS-INFN.

The first part of our analysis was focused on the identification of periods of seismic anomalies, to discriminate between seismic activity and moderate seismicity.

We considered the Italian Seismological Instrumental and Parametric Data-Base and we selected events occurred between April 16^{th}, 2005 and September 30^{th}, 2014 with $M_l \geq 1.0$, in the circular region centered at LNGS-INFN with a radius of 100 km. The catalog was tested for being homogeneous and complete.

The leading role in the seismic analysis is played by the energy release E_i, estimated for each i-th seismic event with magnitude M_i and normalized to the minimum energy release E_{min}, relative to the minimum value of magnitude M_{min} considered. The normalized energy release was calculated for monthly sliding time windows, together with the number of events.

For a better characterization of seismicity as a function of the distance from our groundwater sampling site, we chose circular regions centered at LNGS-INFN with a radius ranging from 10 up to 70 km and circular sectors with a radius of 30 km (North-West, North-East, South-West and South-East respect to LNGS-INFN). We realized an *a posteriori* analysis, centered at the epicentral coordinates of the L'Aquila main shock, to highlight the differences between the physical seismic process and the way we observe it from our groundwater sampling site (LNGS-INFN).

We then applied the analysis on the region composed by the intersection between the aquifer and the composite seismogenic sources, to assess a threshold for discriminating between seismic activity and moderate seismicity.

We identified the thresholds L_E and L_N for the monthly energy release and the monthly number of events, respectively, corresponding to the 30% of the considered time interval.

Periods of intense seismic activity are defined as those time intervals when both E and N exceeded the threshold of 30%:

- Period A (L'Aquila earthquake): February-December, 2009;
- Period B: July, 2010-December, 2010;
- Period C: August, 2011-November, 2011;
- Period D: January, 2013-April, 2013.

Aim of this thesis is the study of the link between uranium groundwater anomalies and seismic anomalies around LNGS-INFN.

The second part of our work was therefore based on the characterization of uranium time series. The uranium contents were revealed by ICP-MS technique (using a 7500a from Agilent Technologies). The chemical preparation of the samples consisted in filtering and pouring the water into 10 ml flasks. A quantity of 250 μl of nitric acid was added to each flask. The concentrations of U were evaluated by means of a four levels calibration curves, using standard solutions.

We described the process of optimization of a Fast Fourier Transform (FFT) algorithm. Such a script was developed and enforced to derive information about the main features of the uranium time series. The characteristic frequency intervals were revealed and filtered. As a final step, the outliers of the residual series were identified.

We first tested the algorithm's functionality on synthetic time series, to avoid the identification of spurious outliers or spurious frequency intervals.

The analysis was then applied to the time series of uranium contents of groundwater sampled in sites E1, E3, E3dx and E4, displaced inside the underground facilities.

Our main result is the observation of an anomalous behavior of uranium content just before the L'Aquila earthquake, in every sampling site considered. Some cross-correlations between outliers were found, like the cases of 09/12/08 and 26/01/09 for E3 and E4, 16/12/08 for E1, E3dx and E4, 22/12/08 for E1 and E4. Furthermore, we observed an anomalous value before the seismic swarm that affected the region under consideration between

July and December, 2010, only in the sampling site E3dx. No anomalous value in uranium content was observed during the seismic activity time spans.

We propose that the uranium groundwater anomalies observed before the seismic swarm and the main shock, which occurred on April 6^{th}, 2009 in L'Aquila, provide a key geochemical signal of a progressive increase of deep CO_2 fluxes at middle-lower crustal levels. Repeated sharp U enrichments in groundwater, that can be directly associated with the geodynamics of the earthquake, represent a much more precise strain-meter than radon. Indeed, radon concentration depends on its parent nuclides uranium and radium during the preparation phase of the earthquake (and on their geochemical patterns with reference to environmental redox and pH characteristics) and it is only successively released by microfracturing, during the main shock and aftershocks (see Plastino et al. (2011) and references therein).

The uranium anomalies can therefore be used as a possible strain meter in domains where continental lithosphere is subducted (Plastino et al., 2011).

To be sure of the role of endogenic fluid dynamics for uranium content in groundwater rather than percolation processes, due to meteoric events occurring above the water table of the Gran Sasso aquifer, further radionuclides analysis is required. For instance, the $^{226}Ra/^{238}U$ activity ratio shows whether or not Ra and U radionuclides are in secular equilibrium, possibly opening a new scenario for radon dynamic processes, linked to its parent nuclides content in groundwater. The ^{3}H concentration in groundwater is directly proportional to the meteoric events which replenish the aquifer and it is inversely proportional to the elapsed time since their infiltration in the soil. Continuous analyses of ^{3}H are therefore necessary to support or to deny the hypothesis that the contribution due to percolation processes, linked with meteoric events before the seismic swarm, particularly the snow melting during the spring-summer time, does not affect the groundwater dynamics through possible mixing with younger surface water.

Furthermore, time series analysis of pH, redox potential, electrical conductivity and hardness of the water are necessary for a chemical characterization of groundwater samples, and to verify whether they could support uranium groundwater anomalies.

In conclusion, criteria evaluated in this study for the detection of uranium groundwater anomalies might be applied to data systematically recorded at LNGS-INFN. In this way, real-time uranium anomalies detected within the Gran Sasso aquifer, which might precede future earthquakes, could be identified. This test could represent an interesting development of the performed study.

Acknowledgments

Desidero ringraziare sentitamente tutti coloro che hanno contribuito alla realizzazione della mia Tesi con suggerimenti, critiche ed osservazioni.

Per il prezioso contributo scientifico ringrazio il Prof. Wolfango Plastino, la Dott.ssa Antonella Peresan e il Dott. Ing. Stefano Nisi. Grazie per la loro guida sapiente, attenta e premurosa.

Ringrazio tutti i dipendenti, dottorandi e assegnisti del Servizio di Chimica e dell'Esperimento ERMES dei Laboratori Nazionali del Gran Sasso: Dott. Ing. Marco Balata, Sig. Luca Ioannucci, Dott. Lorenzo Copia, Dott. Maria Laura Di Vacri, Dott. Angela Cardarelli, Sig. Giuseppina Giusti. Grazie per i loro preziosi consigli e per il tempo e le energie che hanno dedicato alla realizzazione del mio lavoro.

Un grazie speciale va a tutti i miei amici. Loro ci sono stati, ci sono e ci saranno sempre.

Infine, questo traguardo è dedicato alla mia famiglia: grazie mamma, papà, Jam, Tel, nonna, Mac e P.

Bibliography

A. Akinci, F. Galadini, D. Pantosti, M. Petersen, L. Malagnini, and D. Perkins. Effect of Time Dependence on Probabilistic Seismic-Hazard Maps and Deaggregation for the Central Apennines, italy. *Bulletin of the Seismological Society of America*, 99(2A):585–610, 2009.

C.J. Allègre and C. Sutcliffe. *Isotope Geology*. Cambridge University Press, 2008.

A. Amoruso, L. Crescentini, M. Petitta, and M. Tallini. Parsimonious recharge/discharge modeling in carbonate fractured aquifers: The groundwater flow in the Gran Sasso aquifer (Central Italy). *Journal of Hydrology*, 476(0):136 – 146, 2013.

A.N.A.S.-CO.GE.FAR. Gran Sasso. Il traforo autostradale, 1980.

D.L. Anderson. *Theory of the Earth*. Blackwell Scientific Publications, 1989.

M. Barbieri, T. Boschetti, M. Petitta, and M. Tallini. Stable isotope (^{2}H, ^{18}O and ^{87}Sr/^{86}Sr) and hydrochemistry monitoring for groundwater hydrodynamics analysis in a karst aquifer (Gran Sasso, Central Italy). *Applied Geochemistry*, 20:2063 – 2081, 2005.

M.S. Bartlett. Smoothing Periodograms from Time-Series with Continuous Spectra. *Nature*, 161:686–687, 1948.

M.S. Bartlett. Periodogram Analysis and Continuous Spectra. *Biometrika*, 37(1/2):1–16, 1950.

R. Basili, G. Valensise, P. Vannoli, P. Burrato, U. Fracassi, S. Mariano, M.M. Tiberti, and E. Boschi. The Database of Individual Seismogenic Sources (DISS), version 3: Summarizing 20 years of research on Italy's earthquake geology. *Tectonophysics*, 453:20 – 43, 2008. Earthquake Geology: Methods and Applications.

J.S. Becker. *Inorganic Mass Spectrometry: Principles and Applications*. Wiley, 2008.

F. Bella, P.F. Biagi, M. Caputo, E. Cozzi, G. Della Monica, A. Ermini, W. Plastino, and V. Sgrigna. Aquifer-induced Seismicity in the Central Apennines (Italy). In Shahriar Talebi, editor, *Seismicity Caused by Mines, Fluid Injections, Reservoirs, and Oil Extraction*, Pageoph Topical Volumes, pages 179–194. Birkäuser Basel, 1999. ISBN 978-3-7643-6048-1.

C. Boni, P. Bono, and G. Capelli. Schema idrogeologico dell'Italia Centrale, 1986.

E. Brigham. *The Fast Fourier Transform*. Prentice Hall, 1974.

M. Buscema and M. Ruggieri. *Advanced Networks, Algorithms and Modeling for Earthquake Prediction*. River Publishers, 2011.

S. Cavalli. *IC: Attualità, Evoluzione e Prospettive*. Tecniche Nuove, 2004. ISBN 9788848169332.

C. Chatfield. *The Analysis of Time Series: An Introduction, Sixth Edition*. Chapman & Hall/CRC Texts in Statistical Science. Taylor & Francis, 2013.

M. Ciarletti. Misura dei rapporti isotopici dell'Uranio in acqua ai LNGS nell'ambito dell'esperimento ERMES. Graduation thesis, Roma Tre University, 2011.

G. De Natale, I. Kuznetzov, T. Kronrod, A. Peresan, A. Saraò, C. Troise, and G. F. Panza. Three decades of seismic activity at mt. vesuvius: 1972-2000. *Pure and Applied Geophysics*, 161(1):123–144, 2004.

M.L. Di Vacri. Radiopurity in nuclear physics research materials: increased sensitivity in mass spectrometric analysis and development of a purification procedure. Graduation thesis, Università degli studi dell'Aquila, 2008/2009.

V.P. Dimri. *Fractal Behaviour of the Earth System*. Springer, 2005.

G. Echevarria, M.I. Sheppard, and J. Morel. Effect of ph on the sorption of uranium in soils. *Journal of Environmental Radioactivity*, 53(2):257 – 264, 2001.

E. Falcucci, S. Gori, M. Moro, A.R. Pisani, D. Melini, F. Galadini, and P. Fredi. The 2009 L'Aquila earthquake (Italy): What's next in the region? Hints from stress diffusion analysis and normal fault activity. *Earth and Planetary Science Letters*, 305(3-4):350 – 358, 2011.

M.L. Frezzotti, A. Peccerillo, and G. Panza. Carbonate metasomatism and CO_2 lithosphere-asthenosphere degassing beneath the western mediterranean: An integrated model arising from petrological and geophysical data. *Chemical Geology*, 262(1-2):108–120, 2009.

H. Fuenzalida and B. Rosenbluth. Prewhitening of climatological time series. *Journal of Climate*, 1989.

M. Gascoyne, J. K. Osmond, and J. B. Cowart. Geochemistry of the actinides and their daughters. In *Uranium-series Disequilibrium: Applications to Earth, Marine, and Environmental Science (ed. M. Ivanovich and R. S. Harmon)*. Clarendon Press, 1992.

Paolo Gasperini, Barbara Lolli, and Gianfranco Vannucci. Empirical calibration of local magnitude data sets versus moment magnitude in italy. *Bulletin of the Seismological Society of America*, 103(4):2227–2246, 2013.

D. Giammar. *Geochemistry of uranium at mineral-water interfaces: rates of sorption-desorption and dissolution-precipitation reactions*. phd thesis, California Institute of Technology, 2001.

B. Gutenberg and C.F. Richter. The energy of earthquakes. *Q. J. Geol. Soc. London*, 1956.

C. R. Hammond. *The Elements, in Handbook of Chemistry and Physics 81st ed.* CRC Press, 2000.

R.S. Harmon. *Uranium-series Disequilibrium: Applications to Earth, Marine, and Environmental Sciences*. Oxford science publications. Clarendon Press, 1992.

I. Jackson. *The Earth's Mantle: Composition, Structure, and Evolution*. Cambridge University Press, 2000.

E. Jenne. *Adsorption of Metals by Geomedia: Variables, Mechanisms, and Model Applications*. Elsevier Science, 1998.

R.G. Kelly, J.R. Scully, D. Shoesmith, and R.G. Buchheit. *Electrochemical Techniques in Corrosion Science and Engineering*. Corrosion Technology. Taylor & Francis, 2002.

K.M. Krupka and R.J. Serne. *Geochemical Factors Affecting the Behavior of Antimony, Cobalt, Europium, Technetium, and Uranium in Vadose Sediments*. Prepared for CH2M HILL Hanford Group, Inc., and the U.S. Department of Energy under Contract DE-AC06-76RL01830, 2002.

D. Langmuir. *Aqueous environmental geochemistry*. Prentice Hall, 1997.

MATLAB. *version 7.9.0 (R2009b)*. The MathWorks Inc., Natick, Massachusetts, 2009.

S. Nidasio. Determinazione di uranio e torio a livelli di ultratracce mediante spettrometria di massa con sorgente al plasma. Graduation thesis, Università degli studi di Pavia, 1994/1995.

T. Ohnuki, H. Isobe, N. Yanase, T. Nagano, Y. Sakamoto, and K. Sekine. Change in Sorption Characteristics of Uranium during Crystallization of Amorphous Iron Minerals. *Journal of Nuclear Science and Technology*, 34 (12):1153–1158, 1997.

W. Plastino. Monitoring of geochemical and geophysical parameters in the Gran Sasso aquifer. In P. Povinec and J.A. Sanchez-Cabeza, editors, *Radionuclides in the Environment Int. Conf. On Isotopes in Env. Studies*, volume 8 of *Radioactivity in the Environment*, pages 335 – 341. Elsevier, 2006.

W. Plastino and F. Bella. Radon groundwater monitoring at underground laboratories of Gran Sasso (Italy). *Geophysical Research Letters*, 28(14): 2675–2677, 2001.

W. Plastino, S. Nisi, G. De Luca, M. Balata, M. Laubenstein, and F. Bella. Environmental radioactivity in the ground water at the Gran Sasso National Laboratory (Italy): a possible contribution to the variation of the neutron flux background. *Journal of Radioanalytical and Nuclear Chemistry*, 282(3):809–813, 2009. ISSN 0236-5731.

W. Plastino, R. Plenteda, G. Azzari, A. Becker, P.R.J. Saey, and G. Wotawa. Radioxenon time series and meteorological pattern analysis for ctbt event categorisation. *Pure and Applied Geophysics*, 167(4-5):559–573, 2010a.

W. Plastino, Povinec P.P., G. De Luca, C. Doglioni, S. Nisi, L. Ioannucci, M. Balata, M: Laubenstein, F. Bella, and E. Coccia. Uranium groundwater anomalies and L'Aquila earthquake, 6th April 2009 (Italy). *Journal of Environmental Radioactivity*, 101(1):45 – 50, 2010b.

W. Plastino, G.F. Panza, C. Doglioni, M.L. Frezzotti, A. Peccerillo, P. De Felice, F. Bella, P.P. Povinec, S. Nisi, L. Ioannucci, P. Aprili, M. Balata, M.L. Cozzella, and M. Laubenstein. Uranium groundwater anomalies and active normal faulting. *Journal of Radioanalytical and Nuclear Chemistry*, 288 (1):101–107, 2011.

W. Plastino, M. Laubenstein, S. Nisi, A. Peresan, P.P. Povinec, M. Balata, F. Bella, A. Cardarelli, M. Ciarletti, L. Copia, M. De Deo, B. Gallese, and L. Ioannucci. Uranium, radium and tritium groundwater monitoring at INFN-Gran Sasso National Laboratory, Italy. *Journal of Radioanalytical and Nuclear Chemistry*, 295(1):585–592, 2013.

D. Porcelli, P.S. Andersson, G.J. Wasserburg, J. Ingri, and M. Baskara. The importance of colloids and mires for the transport of uranium isotopes through the Kalix River watershed and Baltic Sea. *Geochimica et Cosmochimica Acta*, 61(19):4095 – 4113, 1997.

G. Reina. *La materializzazione del sistema di riferimento tramite reti di stazioni permanenti GNSS in ambito globale e locale: metodologie di elaborazione dei dati e aspetti applicativi.* PhD thesis, Università degli Studi di Roma 'La Sapienza', 2006.

L. Romashkova and A. Peresan. Analysis of italian earthquake catalogs in the context of intermediate-term prediction problem. *Acta Geophysica*, 61 (3):583–610, 2013.

G.T. Seaborg. *Uranium.* The Encyclopedia of the Chemical Elements, 1968.

J.C. Sheppard, M.J. Campbell, T. Cheng, and J.A. Kittrick. Retention of radionuclides by mobile humic compounds and soil particles. *Environmental Science & Technology*, 14(11):1349–1353, 1980.

P. Stoica and R.L. Moses. *Spectral analysis of signals.* Pearson Prentice Hall, 2005.

H.E. Taylor. *Inductively Coupled Plasma-mass Spectrometry: Practices and Techniques.* Academic Press, 2001.

J.T. Watson and O.D. Sparkman. *Introduction to Mass Spectrometry: Instrumentation, Applications, and Strategies for Data Interpretation.* Wiley, 2008.

P.D. Welch. The use of fast Fourier transform for the estimation of power spectra: a method based on time averaging over short, modified periodograms. *Audio and Electroacoustics, IEEE Transactions on*, 15(2):70–73, 1967.